EFFECT OF SHEAR LAYER UNSTEADINESS ON THE AERODYNAMICS OF A PITCHING AIRFOIL

By

Alireza Safaripour-Tabalvandani

A DISSERTATION

Submitted to
Michigan State University
in partial fulfillment of the requirements
for the degree of

Mechanical Engineering – Doctor of Philosophy

2020

ABSTRACT

EFFECT OF SHEAR LAYER UNSTEADINESS ON THE AERODYNAMICS OF A PITCHING AIRFOIL

By

Alireza Safaripour-Tabalvandani

It is common practice to utilize a uniform approach flow in most of the problems in aerodynamics. However, in numerous circumstances the complex approach flows found in nature can be significantly non-uniform and even include spatially non-uniform temporal fluctuations. Motivated by these non-uniform unsteady flows, this experimental study investigates the effects of non-uniform approach flow unsteadiness on the aerodynamic performance of an airfoil.

To isolate the effects of unsteadiness from those of the mean non-uniform approach flow, two non-uniform (shear) flows with a matching mean velocity profile are generated in a water tunnel facility. One of these profiles is made through a canonical two-stream shear layer, which is known to contain vortical structures and exhibit non-uniform velocity fluctuations. A matching shear velocity profile with uniform low level fluctuations is generated utilizing a modified shaped honeycomb shear generation method based on the original model proposed by Kotansky (1966). These shear flows demonstrate the same mean behavior and only differ in their fluctuation profiles.

Behavior and development of both shear flows are examined through measurements of their streamwise velocity profile at multiple downstream locations utilizing single component molecular tagging velocimetry. The steady and unsteady shear flows are found to produce the same mean velocity profile with different classes of velocity fluctuations. The steady shear flow demonstrates a uniform low level of fluctuating velocity profile while the unsteady shear layer velocity fluctuations mimic the signature fluctuating velocity profile of plane mixing layers, with a high level of fluctuations in the center and a gradual decrease in fluctuations moving away from the shear layer center line.

A NACA0012 airfoil is positioned at the center of each shear flow and the average aerodynamic forces on the stationary airfoil are directly measured across a wide range of angles of attack. The

resulting lift and drag coefficient curves are compared for each of these shear flows as well as the reference uniform flow. The unsteady shear layer is found to generate a positive lift at zero angle of attack, in contrast to the negative lift observed under the same condition in the steady shear flow. Furthermore, in the presence of the unsteady shear flow, the linear region of the lift curve around zero angle of attack shows a larger slope and extends over a wider range of angles of attack compared to those of the steady shear and uniform flow lift curves. The unsteady shear flow results in a smaller magnitude of drag at small angles of attack compared to the other two flow conditions.

Force measurements are also performed with the airfoil set to sinusoidally pitch around its quarter chord over a range of oscillation frequencies at the center of both shear flows and the reference uniform flow. The mean lift results show that at small oscillation frequencies the steady and unsteady shear flows produce opposite sign lift forces (negative lift in steady shear flow), but both result in positive lift coefficients of similar magnitudes at higher frequencies. The presence of shear and its unsteadiness seems to only weakly affect the mean and fluctuations of the streamwise force, with almost no effect observed on lift fluctuations.

A closer look at the flow around the surface of the stationary airfoil reveals interesting differences between the behavior of the airfoil boundary layer in the presence of steady versus unsteady shear flow. Single component molecular tagging velocimetry is used to measure the streamwise velocity of the flow near the surface of the airfoil at multiple angles of attack in each shear flow. While the steady shear layer results confirm the presence of laminar separation on the suction side of the airfoil at the angles of attack investigated here, no sign of laminar separation or a reverse flow region is found when the airfoil is placed in the unsteady shear layer.

The wake flow behind the pitching airfoil is also visualized through molecular tagging flow visualization to qualitatively examine how these shear flows affect the wake flow behavior. It is observed that both steady and unsteady shear flows result in the wake flow deflecting towards the high speed side of the flow at high oscillation frequencies, with more cycle-to-cycle variation and perturbations observed in the presence of unsteady shear flow.

This thesis is dedicated to my family.

ACKNOWLEDGEMENTS

It is almost impossible to achieve anything meaningful in life just by yourself. During my long journey as a student, I have received support and assistance through many sources. I would like to acknowledge and express my gratitude towards those who helped me get where I am today.

First of all, I would like to thank my wife without whom none of this would have been possible. She has supported me every step of the way, even through many many, very very late nights of experimental work. Even though she is not a mechanical engineer, she seems to always know the solution to even my academic problems. I would also like to thank my family, especially my parents for all their support and sacrifices from near and far. My very special gratitude goes to Dr. David Olson, who has been very patient and helpful despite my endless relevant or irrelevant questions. Our conversations have allowed me to vent, decompress, brainstorm and get through the hard times a little easier. I very much appreciate his invaluable contributions.

I am also thankful to my current and former TMUAL inmates who I have enjoyed working with, including Dr. Patrick Hammer, Mitchell Albrecht, Borhan Hamedani and Kian Kalan with a very special mention to Dr. Shahram Pouya who had been a pillar of TMUAL for so long that it was harder than I thought to get used to working at TMUAL without him.

Most importantly, my very special gratitude goes to my advisor, Prof. Koochesfahani who has been not just a great advisor, but also like a father to me for the past few years, guiding me through my academic journey as well as pointing out ways to improve myself for life beyond academia. It is always a blessing to have a compassionate adviser who thinks of his students as his sons, especially when your parents are far away and you need all the support you can get. I would also like to extend my gratitude to Prof. Naguib for all his help and guidance over the years.

Lastly, this work was sponsored by AFOSR award numbers FA9550-10-1-0342 and FA9550-15-1-0224.

TABLE OF CONTENTS

LIST OF TABLES

LIST OF FIGURES

CHAPTER 1

INTRODUCTION

The focus of this work is to study how the unsteady behavior of a non-uniform approach flow influences the aerodynamic performance of an airfoil in stationary and oscillating circumstances. The majority of aerodynamic problems consider a uniform approach flow, an assumption that is not always representative of the complex flows found in nature. In practice, there are many circumstances where the approach velocity profile is non-uniform, such as when an airplane encounters wind shears or large-scale disturbances due to the topography of the terrain beneath. Furthermore, in many of the practical situations where non-uniform flows are encountered, they could include inherent vortical structures and spatially non-uniform temporal velocity fluctuations. These fluctuations, on top of their mean velocity gradient, may further affect the aerodynamic performance of an airfoil. Although there have been studies focusing on the effect of non-uniform (shear) flows on airfoil aerodynamics, many of them are limited to theoretical inviscid flows and there are very few systematic experimental research on airfoils in real viscous shear flows. There are even less published works on the influence of unsteady shear flows on airfoils.

1.1 Background

It is beneficial to first introduce and define the different approach flows that are referred to in this document. Figure 1.1 presents the three different upstream flow conditions studied in this research. A uniform approach flow refers to the most common upstream boundary condition where both the mean and low-level background fluctuating velocity profiles are spatially uniform (Figure 1.1a). This profile represents the typical approach flow in most experimental flow facilities. A steady non-uniform (shear) flow has a non-uniform mean velocity profile with a spatially uniform (and low magnitude) background velocity fluctuation profile (Figure 1.1b). This indicates that the instantaneous velocity profiles are all very close to the mean velocity profile. The flows in which the mean and fluctuating velocity profiles are both spatially non-uniform, with significant

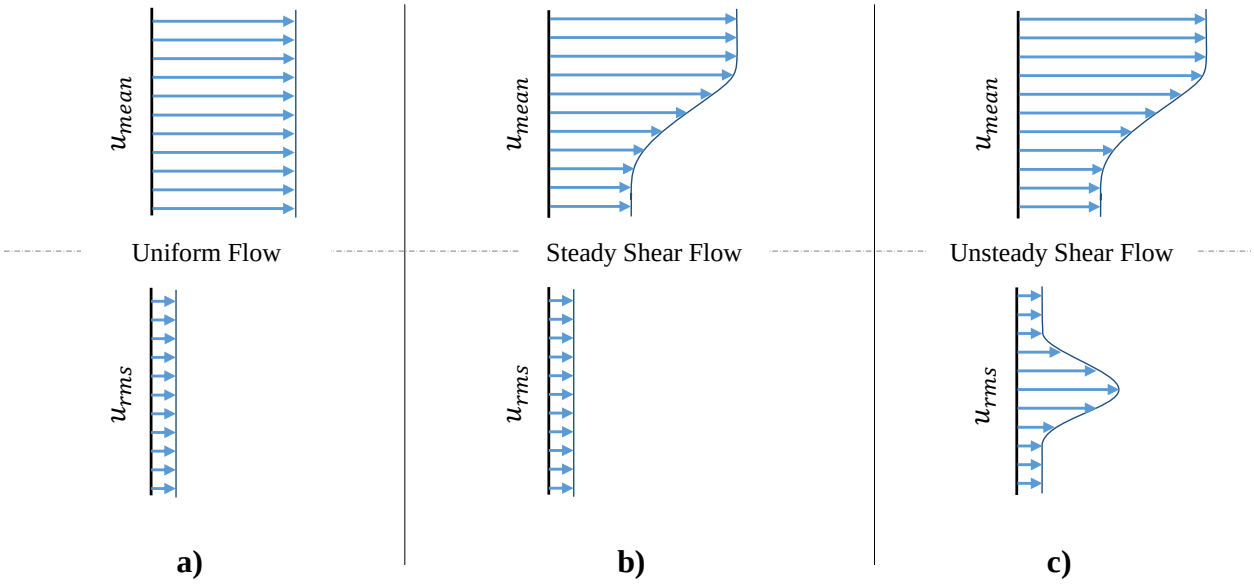

Figure 1.1: Schematic of mean and fluctuating velocity profiles of different approach flow conditions considered in this work: **(a)** Uniform flow, **(b)** Steady non-uniform (shear) flow and **(c)** Unsteady non-uniform (shear) flow.

levels of peak fluctuations, are referred to here as unsteady non-uniform (shear) flows (Figure 1.1c) in this document. In these unsteady shear flows, the instantaneous velocity profiles can be very different from the mean velocity profile, depending on the magnitude and distribution of velocity fluctuations.

As one of the first works on the effect of a steady non-uniform approach velocity on the behavior of an airfoil, Tsien (1943) assumed a 2D steady inviscid flow with a linear velocity profile (uniform shear rate) approaching a symmetric Joukowsky airfoil and showed the presence of the shear flow resulted in a shift in the zero-lift angle of attack for the airfoil. The main conclusion from his work was that a symmetric airfoil at zero angle of attack (AoA) in a positively sheared approach flow generates a positive lift and the magnitude of this generated lift increases with the shear rate of the approach flow. Several studies have expanded the scope of Tsien's work to more general velocity profiles, but all of these studies are limited to inviscid steady flows (see James, 1951; Honda & Lighthill, 1960; Nishiyama & Hirano, 1970)

As mentioned previously, there are very limited systematic studies on the effects of steady shear flows on airfoils in real viscous flows. A rare experimental study by Payne & Nelson (1985)

considered a steady NACA 0018 airfoil in both uniform and steady shear flows in a wind tunnel with chord Reynolds numbers of 75,000 to 200,000. They used a force balance to measure lift and drag forces and found that while the lift and drag curves exhibited an asymmetry due to the shear flow, the aerodynamic characteristics of the airfoil were mainly unaffected by the introduced velocity gradient. They observed a flow induced asymmetry in drag coefficient curves, with a positive shear resulting in a higher drag coefficient at positive angles of attack. They concluded that the effects of shear flow was of the same order of magnitude as of those due to other phenomena such as additional turbulence generated by their shear generation method.

A more recent numerical study by Lee et al. (2014) observed an increase in the lift coefficient of an S809 airfoil (dedicated to horizontal-axis wind turbines, this is an asymmetric airfoil with an expected positive lift at zero AoA) in the presence of a positive steady shear flow, and a reduction in the case of negative shear. They found this increase to be independent of the angle of attack for Reynolds numbers in the order of 10^6.

Ongoing numerical and experimental studies in our own group in the Turbulent Mixing and Unsteady Aerodynamics Laboratory at Michigan State University have shown some interesting effects of viscous shear flows on aerodynamic performance of airfoils. Hammer et al. (2018) investigated the effect of a steady shear flow on a stationary NACA 0012 airfoil with a chord Reynolds number of $Re_c = 1.2 \times 10^4$ through 2D numerical simulations. Their steady shear flow was a three-segmented profile with a linear velocity profile extending over a finite thickness, δ, in between two uniform velocity zones (Figure 1.2a). This velocity profile was characterized by a non-dimensional shear rate $K = \frac{du}{dy} \times \frac{c}{U_\infty}$ and δ was selected large enough ($\delta \approx 1.5c$) so that the finite thickness of the shear zone would not affect the results. They found that a positive linear shear flow results in a ***negative*** lift coefficient at zero AoA (Figure 1.2b), which is contrary to predictions of the inviscid theory by Tsien (1943). Their hypothesis for this observation was that while the airfoil is geometrically symmetric, due to the asymmetric development of viscous boundary layers on the upper and lower surfaces of the airfoil, it behaves like an airfoil with a negative camber. They also observed that the location of the leading edge stagnation point moves further downstream

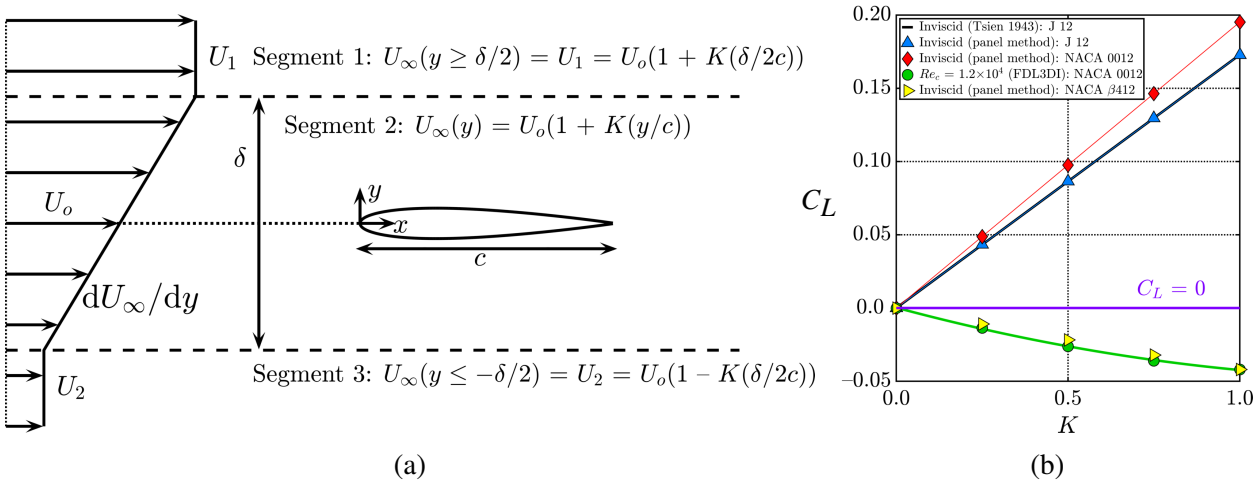

Figure 1.2: **(a)** Schematic of a three-segment linear velocity profile used by Hammer et al. (2018) **(b)** Average lift coefficient, C_L, vs shear rate, K, for inviscid and viscid solution of the airfoils investigated in Hammer et al. (2018). (Figures from Hammer et al., 2018)

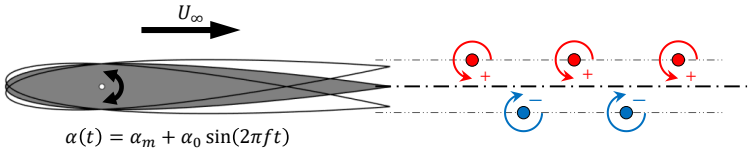

Figure 1.3: Schematic of a reverse von Kármán vortex street behind an airfoil pitching about its quarter chord. The sign of the circulation of the vortex is indicated by the arrow and by the (+) or (-) sign.

with increased shear rate, which is consistent with the behavior of a negatively cambered airfoil. Subsequent experimental force measurements reported in Hammer et al. (2019) also showed a negative lift coefficient at zero AoA for a NACA 0012 airfoil in a similar shear flow, consistent with their previous numerical results and opposite to Tsien's inviscid theory.

In addition to aerodynamic performance of a stationary airfoil, the unsteady aerodynamics of an oscillating airfoil is also of interest. The pure pitching oscillation of an airfoil with chord length c is typically described by its pitch axis location $\left(\frac{o}{c}\right)$, oscillation amplitude (α_0), mean angle of attack (α_m) and reduced frequency $\left(k = \frac{\pi f c}{u_c}\right)$, where f is the oscillations frequency and u_c is the flow speed (See Figure 1.3).

Classical studies (Theodorsen, 1949; von Karman & Burgers, 1935; von Karman & Sears, 1938)

have shown that a simple oscillatory pitching motion of the airfoil can result in the generation of thrust instead of a drag force. Von Karman & Burgers (1935) and Lighthill (1969) associated this thrust generation with an array of alternating-sign vortices shed from the airfoil. Experiments of Koochesfahani (1989) showed the crossover from a von Kármán vortex street to a reverse von Kármán street at high enough oscillation frequencies of a purely pitching airfoil. Bohl & Koochesfahani (2009) found experimentally that for a NACA 0012 airfoil at a chord Reynolds number of $Re_c = 1.25 \times 10^4$, the switch from drag to thrust happened at an oscillation frequency slightly higher than that of the crossover in vortex pattern. Experimental results of Bohl & Koochesfahani (2009) were closely replicated by computations of Hammer (2016) through high fidelity 2D numerical simulations, where he also investigated the effects of Reynolds number and airfoil motion asymmetry on the wake vortex properties. Figure 1.4 shows computational flow visualizations of Hammer (2016) comparing a traditional von Kármán vortex street (result of a low frequency pure pitching oscillation) with a reverse von Kármán vortex street (result of a high frequency pure pitching oscillation) alongside a sketch of the wake velocity profiles.

The effects of a steady shear approach flow on the aerodynamic performance of an unsteady airfoil in pure pitching oscillation is reported by Hammer et al. (2019). In this study, complimentary numerical and experimental investigations were performed on a NACA 0012 airfoil pitching harmonically about its quarter-chord, with an oscillation amplitude of $\alpha_0 = 2°$ and reduced frequencies up to $k = 12$, in a positive steady shear flow. Their approach flow was similar to the profile used in

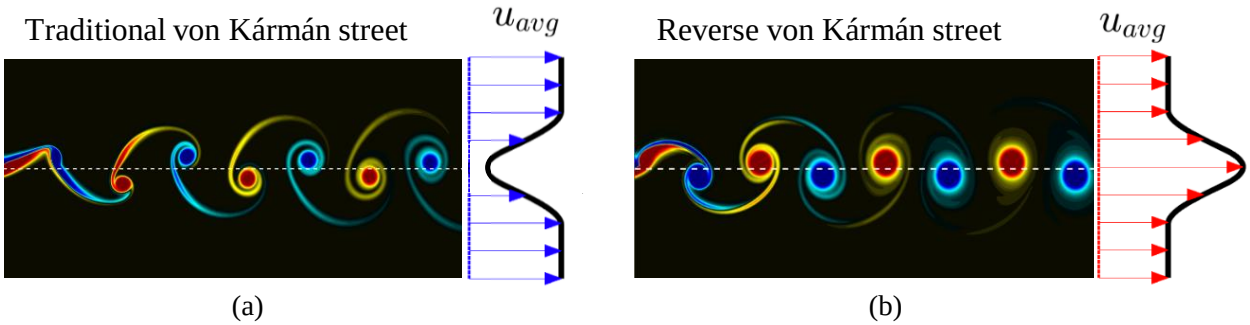

Figure 1.4: Computational flow visualization of traditional von Kármán street **(a)** versus reverse von Kármán street **(b)** with accompanying mean wake velocity profile. (Figures from Hammer, 2016)

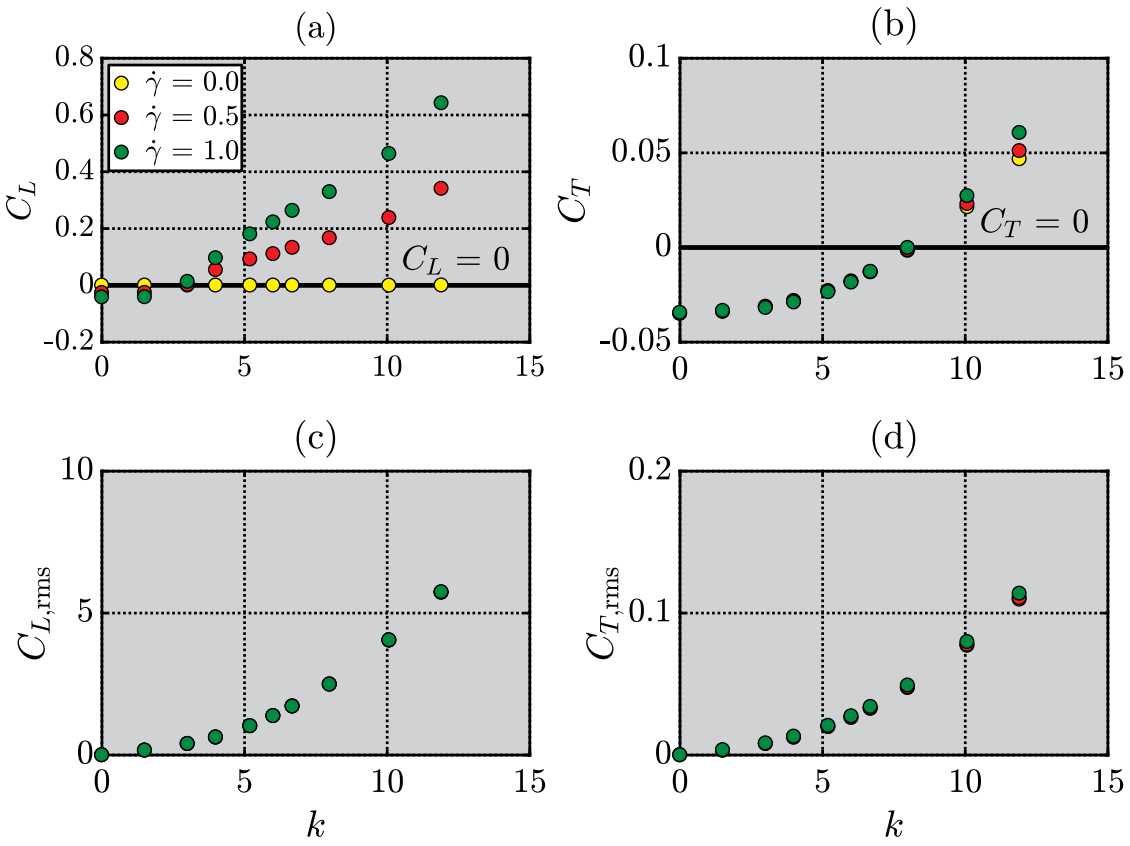

Figure 1.5: Computed mean and fluctuating loads on an oscillating airfoil versus reduced frequency k for different shear rates ($\dot{\gamma}$). (Figures from Hammer et al., 2019)

Hammer et al. (2018) with non-dimensional shear rate values varying between 0 to 1 and a chord Reynolds number of $Re_c = 1.2 \times 10^4$. The numerical part of the study showed a break of the symmetry of the wake structure for all reduced frequencies, with the wake deflecting towards the high speed side at high enough reduced frequencies. Consistent with their previous findings, the presence of shear flow resulted in a negative mean lift coefficient at the limit of stationary airfoil (see Figure 1.5a). They observed that the magnitude of this negative lift decreased with increasing oscillation frequency until it switched sign around a reduced frequency of $k = 3$, and from that point on the magnitude increased going towards higher frequencies. They found that for a constant reduced frequency, the magnitude of the mean lift coefficient increased with non-dimensional shear rate (Figure 1.5a), however, the magnitude of lift coefficient fluctuations did not exhibit any change with shear rate (Figure 1.5c). In addition, Mean and fluctuations of thrust coefficient were weakly affected by the presence of shear in the approach flow (Figures 1.5b & 1.5d). These conclusions

were based on both numerical and experimental results.

All the studies mentioned above pertained to steady shear flows. One of the only experimental measurements available on the effect of an unsteady shear flow on an unsteady airfoil is from Naguib & Koochesfahani (2012). They examined the effect of a canonical plane mixing layer approaching a harmonically pitching NACA 0012 airfoil at a reduced frequency of $k = 10.6$ and oscillation amplitude of $\alpha_0 = 2^\circ$ with a chord Reynolds number of $Re_c = 1.2 \times 10^4$. The phase-resolved spatial map of the streamwise velocity for one oscillation cycle at one chord length downstream of the trailing edge is shown in Figure 1.6 for both the uniform flow and unsteady shear flow. The case of uniform approach flow showed the expected signature from an alternating vortex array in the wake (Figure 1.6a) and the corresponding regions of velocity undershoot/overshoot (evidence of two opposite sign vortices in one oscillation period). However, the results from the unsteady shear flow case exhibited only one region of velocity undershoot/overshoot, without any sign of a similar velocity signature for an opposite sign vortex (Figure 1.6b). This observation seems to imply that in the presence of the unsteady shear flow, the airfoil shed only one vortex structure per oscillation cycle, contrary to the two for the uniform flow. Another interesting observation was the simultaneous presence of both mean momentum excess and deficit in the wake flow.

1.2 Current Study

The main objective of the current Ph.D. thesis is to investigate how the unsteady behavior of a shear flow alters the aerodynamic performance of a low Reynolds number ($Re_c = 1.2 \times 10^4$) airfoil, in both stationary and pitching situations. In order to isolate this issue, it is required to generate two separate matching shear flows with identical mean velocity profiles, where one shows an unsteady nature resulting in spatially non-uniform high-level temporal velocity fluctuations while the other has a steady velocity profile with very low and spatially uniform temporal velocity fluctuations. The goal is to be able to separate the effects that are attributed to the mean shear profile from those caused by unsteadiness of the shear flow.

Regarding the effects of interest, the aerodynamic forces on stationary and pitching airfoils

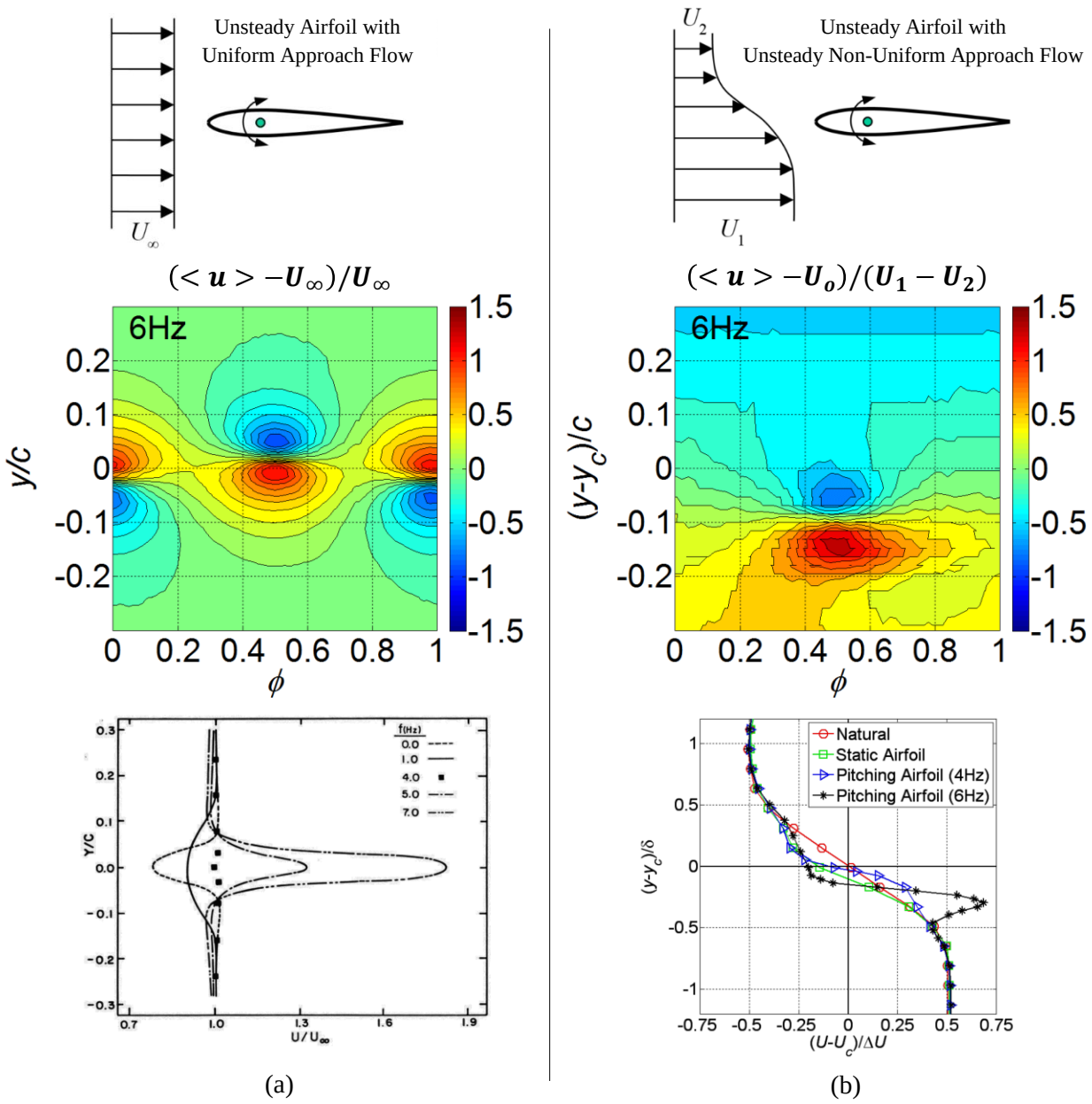

Figure 1.6: Color contour map of phase-averaged streamwise velocity, showing the variation of velocity profiles with phase during one cycle of oscillation in the wake of the pitching airfoil (k = 10.6 Hz, $\alpha_0 = 2°$). **(a)** The baseline case of uniform approach flow shows the expected signature of alternating sign vortex pair. **(b)** In the case of shear layer approach flow, there is evidence for only one vortex core. (Figure courtesy of Koochesfahani & Naguib)

(oscillating over a range of amplitudes and frequencies) are to be compared for these two different shear layers as well as the uniform approach flow. Moreover, boundary layer resolved single component velocimetry on the airfoil surface will be used to investigate the effect of unsteady and steady shear layers on boundary layer behavior of the airfoil. Another point of interest is to qualitatively look at the impact of these two shear layers on the wake characteristics and vortex arrangement behind an oscillating airfoil by means of molecular tagging flow visualization. These measurements will provide the first insight into the role of shear layer unsteadiness on the aerodynamic performance of airfoils in unsteady shear layers as the upstream boundary condition.

1.3 Outline

The remainder of this work is presented in six chapters. Chapter two, briefly introduces the flow facility and experimental techniques used to perform velocimetry and force measurements in the test facility. It also discusses the different methods used to generate the steady and unsteady non-uniform velocity profiles. These experimental techniques are used to generate and characterize the behavior of a pair of matching unsteady and steady shear layers. The results of these shear flow characterizations are presented in Chapter three. Chapter four discusses the stationary and pitching aerodynamic performance of an airfoil positioned in both of these shear layers, through direct measurements of lift and drag coefficients over a range of mean angles of attack, reduced frequencies and oscillation amplitudes. These results are compared with those corresponding to the reference uniform flow as well as previous works in the literature. Effects of shear flow unsteadiness on the behavior of airfoil boundary layer is highlighted in Chapter five, where boundary layer resolved streamwise velocity measurements on a stationary airfoil over a range of angles of attack provide an insight into the underlying mechanisms through which the unsteadiness of the shear flow can affect airfoil's aerodynamic performance. Chapter six qualitatively compares the wake structures of a pitching airfoil in steady versus unsteady shear flows as well as the reference uniform approach flow. Finally, Chapter seven concludes the dissertation with a brief summary of the important results.

CHAPTER 2

EXPERIMENTAL METHODS

2.1 Flow Facility

All the experiments for this project are performed in a 10,000 liter closed-return free surface water tunnel facility (Engineering Laboratory Design Inc., Lake City, MN) located in the Turbulent Mixing and Unsteady Aerodynamics Laboratory (TMUAL) at Michigan State University. The test section of the facility measures 61 cm × 61 cm × 244 cm (shown in Figure 2.1) and has full optical access in the visible spectrum on both sides, bottom and a full height end-view window. As a part of a previous modification, two quartz windows (each 41 cm × 84 cm) were installed to provide optical access for ultraviolet (UV) wavelengths required for Molecular Tagging Velocimetry, as described later on. This flow facility comes with a flow management system consisting of two perforated plates in the entrance diffuser, a ¼" cell diameter honeycomb and fine mesh screen in the settling chamber, a 6:1 contraction channel and finally a ⅛" cell diameter honeycomb and fine mesh screen at the entrance of the test section.

The impeller of the water tunnel is powered by a Toshiba 20 hp motor and controlled with a Toshiba VF-AS1 drive which ensures day-to-day repeatability of the same freestream velocity; this repeatability is a very important requirement since all the velocimetry and force measurements were performed on multiple different occasions spanning over a 2 year time period. While the flow facility can operate up to a maximum freestream velocity (U_∞) of 1 m/s, it was set to a nominal value of $U_\infty = 10$ cm/s for all the measurements performed during this work. The actual magnitude of velocity was slightly fine tuned for each case to maintain the desired Reynolds number amidst year-round temperature changes of laboratory environment and consequently, water. Freestream turbulence intensity ($FSTI = u_{rms}/U_\infty$) of the tunnel was measured to be $\sim 1.9\%$ at this operating conditions. This value includes the known contributions from the very low frequency ($f < 0.2$ Hz) "slushing" of the facility and is consistent with the previous measurements by Katz (2010) and

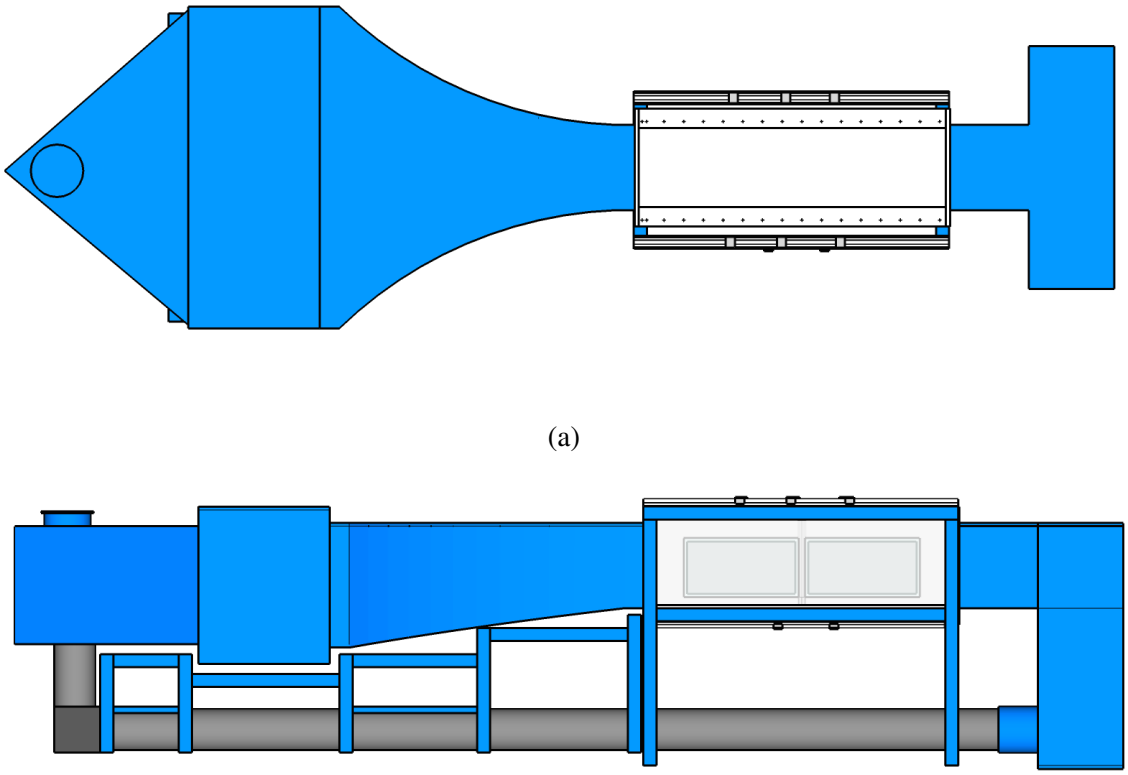

(a)

(b)

Figure 2.1: A scaled drawing of the flow facility. **(a)** Top view, **(b)** Side view. Quartz windows are visible in the side view. (Figures courtesy of Olson, 2017)

Olson (2011) for the same facility. Olson (2011) reported that the effects of this slushing motion can be removed by subtracting the spatial mean velocity at each instance in time to isolate the contributions from broadband turbulence and found the broadband $FSTI$ to be around 0.5% for this facility.

A three-degree-of-freedom (3DOF) servo motion system is mounted on top of the test facility to provide the capability to produce a combination of pitching, plunging and surging motions of the airfoil (Figure 2.2a). This motion system was initially designed and built by Dr. Bruno Monnier and later refined and utilized by Dr. David Olson for experiments reported in Olson (2017) and Hammer et al. (2019). The current study only utilized the pitching capacity of the motion system to oscillate a NACA 0012 airfoil with a chord length of $c = 12$ cm and aspect ratio of $AR = 5.14$ about its quarter chord point. In order to minimize the effects of free surface disturbances during airfoil oscillation, a skimmer plate spanning the width of the tunnel is used. This skimmer plate also

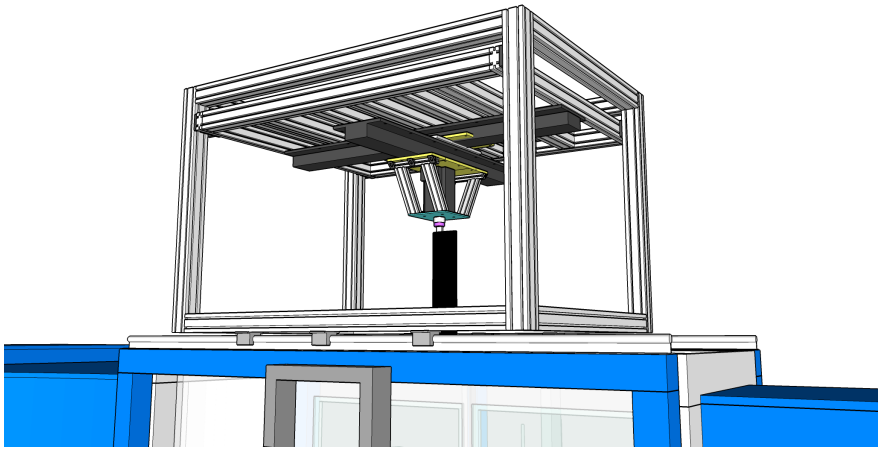

(a)

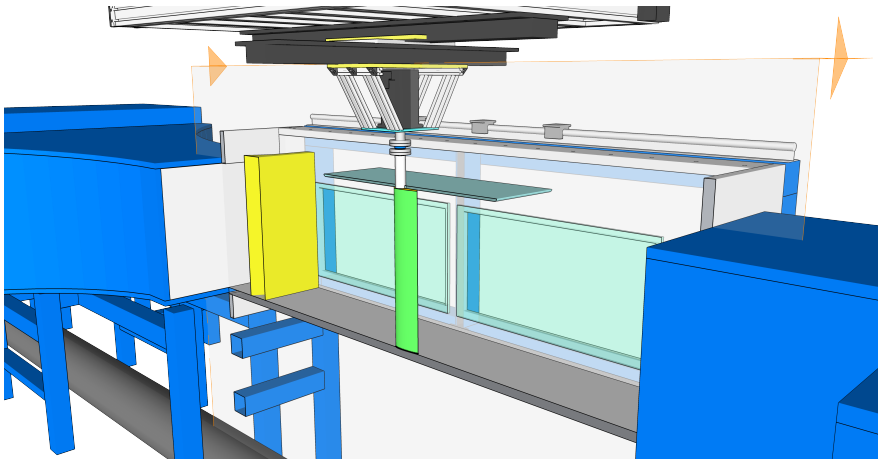

(b)

Figure 2.2: A scaled drawing of the test setup showing **(a)** The three-degree-of-freedom (3DOF) servo motion system, and **(b)** The airfoil and skimmer plate placement in the test section. (Figures courtesy of Olson, 2017)

provides a well-defined boundary condition on the top side of the airfoil. The system is designed so that there is a less than 0.5 mm gap in between the airfoil top surface and the skimmer plate, as well as between airfoil bottom surface and bottom plate of the test section (Figure 2.2b). The actual airfoil pitching motion trajectory is monitored through a high resolution encoder with high resolution of 0.003 degrees.

2.2 Shear Generation Methods

2.2.1 Unsteady Shear Generation

Due to their well-studied behavior, a plane mixing layer is selected as a representative of an unsteady shear layer for this work (Liepmann & Laufer, 1947; Wygnanski & Fiedler, 1970; Brown & Roshko, 1974). Such shear layers are known to produce a high level of spatially non-uniform fluctuations and have been shown to contain vortical structures.

Preliminary experiments in a 6" water tunnel (a ¼ scale of the water tunnel described above) showed that a device with a configuration of two blocks of honeycomb with different tube lengths separated by a splitter plate can be used to generate a two-stream shear layer with a behavior very close to the classical two stream shear layers. Following those results, a similar device was fabricated to be used in the full scale water tunnel facility that would generate a shear layer with a two-to-one velocity ratio. This shear generation device consisted of two uniform honeycomb blocks of lengths 1.5" and 6" with a splitter plate separating them, extending 3" from both ends (see Figure 2.3).

The splitter plate is glued to both honeycomb blocks using urethane adhesive and the honeycomb orientation is aligned so that the straight rows of tubes are parallel to the splitter plate. The honeycomb blocks (PC2 Polycarbonate Honeycomb, Plascore, Zeeland, MI) have circular ⅛" diameter tubes and come in maximum tube length of 12".

In order to make sure the range of airfoil oscillation frequencies will not excite the splitter plate itself, a natural frequency analysis is performed for an assumed cantilever plate length of 3". It is found that using a 0.03" thick (≈0.76 mm) highly corrosion-resistant 316 stainless steel sheet would result in a first natural frequency of 85 Hz which is well beyond the range of airfoil oscillation frequencies ($f < 3$ Hz) and water tunnel's natural frequency (~0.2 Hz). The characteristics of the unsteady shear layer generated by this device is described in section 3.1.

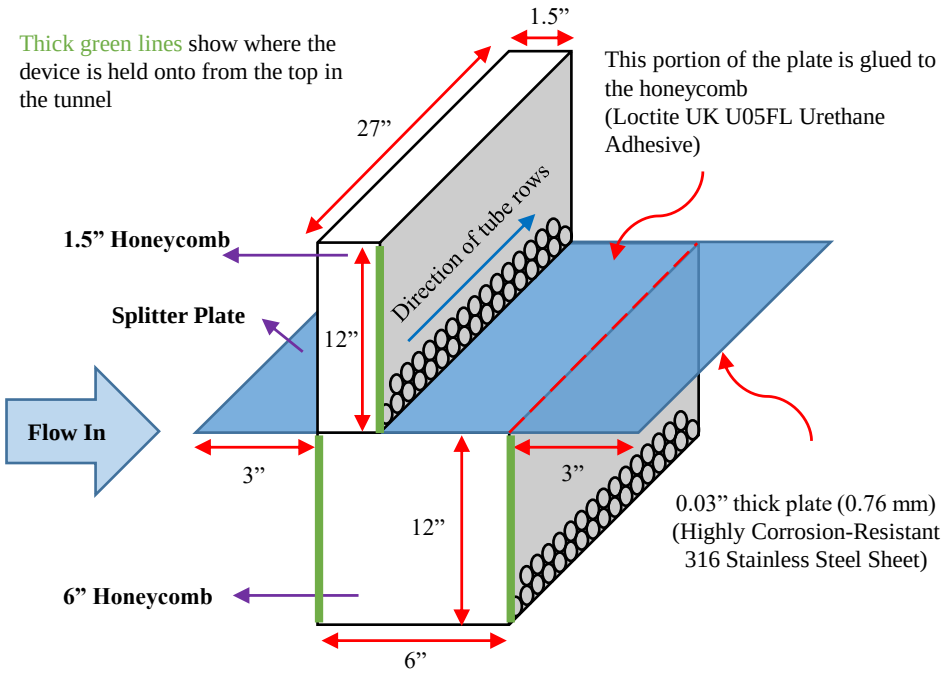

Figure 2.3: A schematic of the two-stream shear generation device

2.2.2 Steady Shear Generation

Various methods have been introduced to alter the uniform flow of facilities by inserting an additional device in the path of the flow, downstream of its original flow management system. Owen & Zienkiewicz (1957) were the first to develop a model to generate a linear velocity profile using a grid of parallel rods with varying cross-stream spacing, which was further modified by Cockrell & Lee (1966) to produce nonlinear velocity profiles. Another model utilizing shaped screens to generate arbitrary velocity profiles was proposed by Elder (1959) and was later refined by Lau & Baines (1968), Turner (1969) and Livesey & Laws (1973). Taking a different approach, Kotansky (1966) developed a simplified model to employ honeycombs with varying tube lengths to create a specified velocity profile. A set of equal-width and equal-length parallel channels with variable internal resistances have also been used by Champagne et al. (1970) to produce a near linear mean velocity profile.

Besides the fact that all of these methods can produce non-uniform velocity profiles, some practical limitations are involved with each method that are worth considering. Maintaining the

designed profile of the shaped screens across the test section is very challenging, especially in larger test facilities. Furthermore, screens can be easily damaged or obstructed which could cause distortions in the resulting velocity profile. The grid of parallel rods are slightly easier to maintain in larger facilities, but this method introduces additional temporal velocity fluctuations into the flow due to the vortex shedding around each individual cylinder. The shaped honeycomb technique is relatively harder to fabricate, but it maintains its structure over time and is less susceptible to minor mishaps. Also, the resulting velocity profiles have a low level of temporal velocity fluctuations (Rose, 1970; Kiya et al., 1980).

Due to the low level of temporal velocity fluctuations required for the current study, and with repeatability of the experiments in mind, the shaped honeycomb technique (Kotansky, 1966) was chosen as the basis for the shear generation method employed in this work. Instead of the original model's assumption of a constant friction factor in all honeycomb tubes, this model is modified to utilize a variable friction factor model to estimate the pressure drop inside honeycomb tubes. This friction factor model (a function of tube length and Reynolds number) is applicable inside the tube entrance length as well as in the fully developed region, in the limit of laminar flow inside the tubes ($Re_d \leq 2300$). Additionally, the model is further refined to eliminate the need to calibrate the pressure drop experimentally for each design.

Figure 2.4 presents a schematic of the shear generation model along with its underlying assumptions. Kotansky (1966) assumed the flow far upstream of the honeycomb has the known uniform inlet velocity, $u_{-\infty}$, with a uniform pressure distribution. Far downstream, the flow has developed into the desired non-uniform velocity profile, $u(y)$, and has recovered a uniform pressure. Based on these assumptions, the overall pressure change (ΔP) between far upstream and far downstream is:

$$\Delta P = P_{-\infty} - P_{+\infty} = \Big[P_{-\infty} - P(0, y)\Big] + \Big[P(0, y) - P(L, y)\Big] + \Big[P(L, y) - P_{+\infty}\Big]. \tag{2.1}$$

The first term on the right hand side of equation 2.1 represents the pressure change upstream of the honeycomb. Kotansky (1966) treats this domain as a potential flow region and hence this pressure change can be found using Bernoulli's equation. The second term is the pressure drop

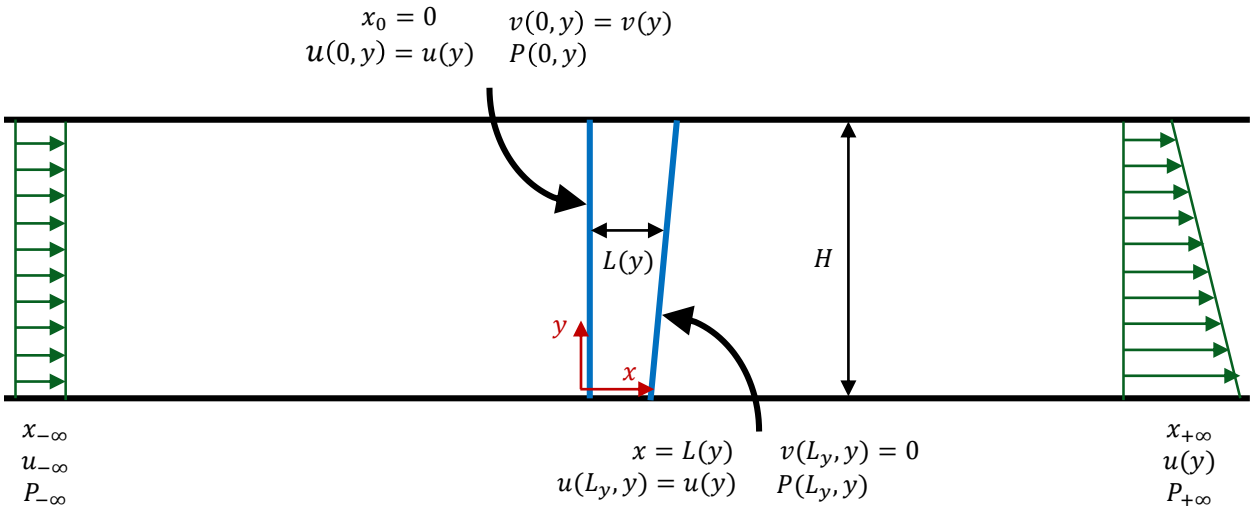

Figure 2.4: A schematic of the shaped honeycomb model along with the main assumptions involved. (after Kotansky, 1966)

inside the honeycomb tubes which can be estimated using a friction factor and Darcy-Weisbach equation. The last term, pressure change downstream of the honeycomb, is presumed to be negligible, based on the assumption of parallel streamlines after the honeycomb. This leads to the following equation for the honeycomb length distribution:

$$L(y) = \frac{d}{4f}\left[\frac{\frac{2}{\rho}\Delta P + {u_{-\infty}}^2 - v(y)^2}{u(y)^2} - 1\right], \tag{2.2}$$

where $L(y)$ is the honeycomb tube length at each y, d the honeycomb tube diameter, f the Fanning friction factor and ρ the fluid density.

Distribution of cross-stream component of velocity profile at the entrance of the honeycomb, $v(y)$, is determined through the solution of potential flow region, while the friction factor, f is estimated based on an asymptotic friction factor model. Finally, a one point boundary condition with a reference honeycomb length is used to find the overall pressure drop value, ΔP. A detailed description of this modified shaped honeycomb model, its performance and the characteristics of the generated profiles is presented in Appendix A.

This shaped honeycomb shear generation method is used to reproduce the mean streamwise velocity profile of the two-stream shear layer with a uniform distribution of fluctuations at the same

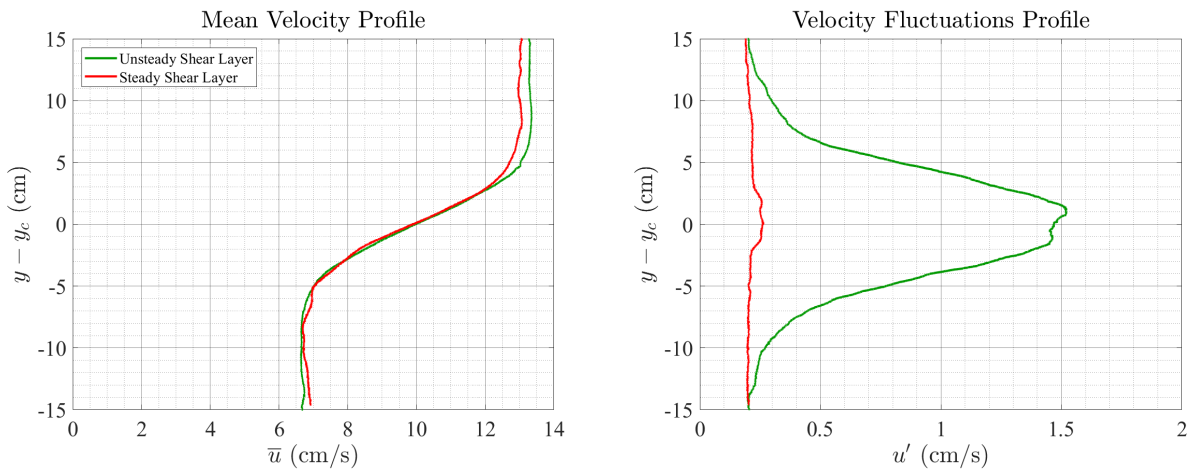

(a) (b)

Figure 2.5: An example comparison of the streamwise **(a)** mean and **(b)** fluctuating velocity profiles in the generated steady shear layer versus the reference unsteady shear layer.

level as the free stream flow. An example of measured mean and fluctuating streamwise velocity profiles for these steady and unsteady shear flows is shown in Figure 2.5.

2.3 Molecular Tagging Velocimetry

2.3.1 Background

Molecular Tagging Velocimetry (MTV) technique is used throughout this work to measure the velocity of the flow. MTV is a whole field non-intrusive optical technique that turns premixed (or naturally present) molecules in the fluid into long lifetime tracers through photon excitation. Typically, a pulsed laser source is used to excite (tag) specific patterns into the area of the flow that is of interest. These tagged regions are interrogated twice with a prescribed time delay to form an image pair (Figures 2.6a & 2.6b). The extracted displacement field from the image pair, along with the known time delay, yields the estimate of the velocity field across the tagged region (Figure 2.6c). For further details about MTV technique, interested readers can refer to Gendrich & Koochesfahani (1996) for MTV image processing procedures and Koochesfahani & Nocera (2007) for a comprehensive review of the development, photochemistry, and several applications of MTV.

In the present work, a water-soluble phosphorescent supramolecule tracer (Gendrich et al., 1997)

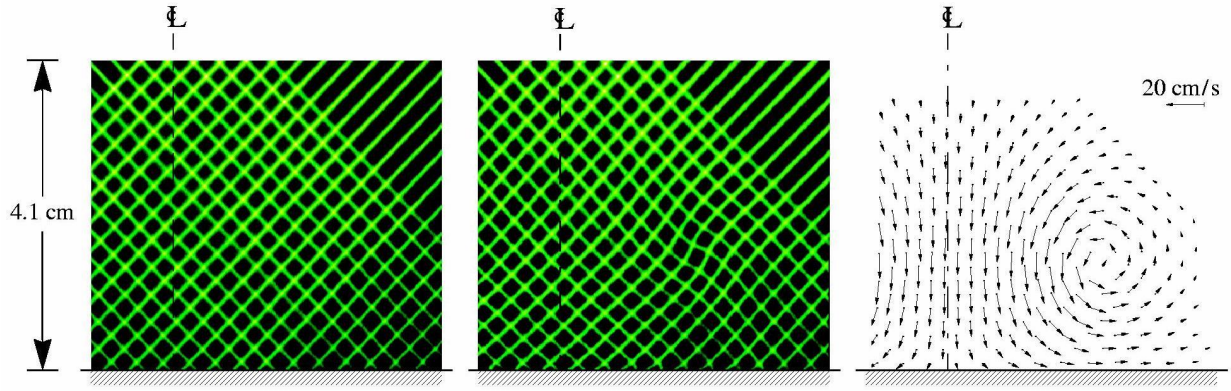

Figure 2.6: Typical MTV image pairs and the resultant velocity field (Gendrich et al., 1997). The flow shown is from a vortex ring impacting on a flat wall at normal incidence. The axis of symmetry is indicated by the dashed lines. **(a)** The grid imaged 1 μs after the laser pulse. **(b)** The same grid imaged 8 ms later. **(c)** The velocity field derived from (a) and (b).

is premixed the water tunnel facility. The chemical composition of this supramolecule consists of the following chemicals: 1×10^4 M of maltosyl-β-cyclodextrin, 0.055 M of cyclohexanol, and a saturated solution of 1-bromonaphthalene ($\sim 1 \times 10^5$ M). The lifetime of this solution was measured to be nominally $\sim\tau$ = 3.5 ms. A Coherent COMPexPro 205 XeCl, an excimer laser with a wavelength of 308 nm and pulse duration of 20 ns, is used to tag this chemical complex.

2.3.2 Single Component MTV for Shear Layer Characterization

Based on the requirements of this study, a single component version of the MTV technique with parallel tagged lines (normal to the freestream flow) is implemented to measure the streamwise velocity of the flow across the width of the test section. Single component MTV (1c-MTV) delivers the capability to measure one component of flow velocity (normal to the tagged lines) at every pixel along the tagged lines to provide a high spatial resolution.

To generate the tagging pattern, the initially rectangular beam of the excimer laser is passed through a cylindrical lens combination to reduce the beam thickness along its shorter axis. This results in a thin and wide laser sheet that can be focused where needed. In this implementation, the optics are fine-tuned to focus the laser sheet (~0.5 mm thick) around the centerline of the test

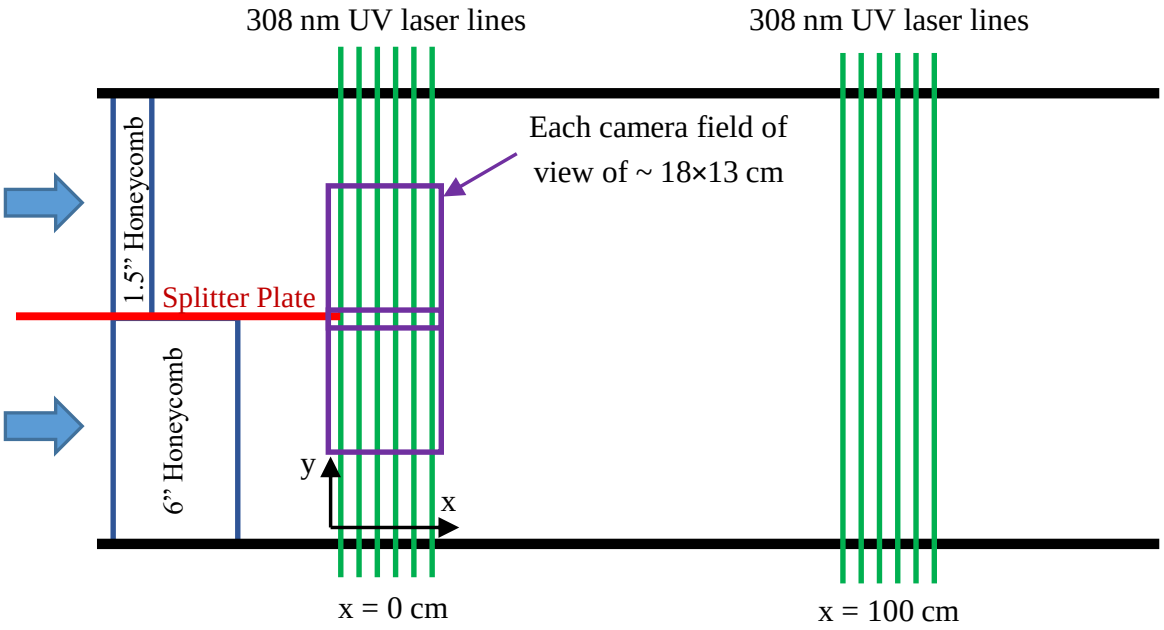

Figure 2.7: A schematic of 1c-MTV streamwise velocity measurement setup utilized in two-stream shear layer generation configuration (top view)

section. The tagging pattern is generated by passing this laser sheet through a brass beam blocker with vertical slots of desired thickness and spacing. The resulting tagging pattern becomes a series of laser lines (typically about 5) each with a full width half maximum (FWHM) width of ~0.7 mm and spaced ~6 mm from each other.

According to the desired domain of measurements required to characterize the shear layer behavior, the imaging system is designed to consist of two CCD cameras (pco.pixelfly) with 35 mm lenses (f/1.2 Nikon Nikkor) mounted side by side underneath the test section. These cameras are positioned so that there is a ~5% overlap between their fields of views. Utilizing this arrangement, each camera images an area about 18 cm × 13 cm (with a resolution of ~114 µm/px), which would cover ~60% of the test section width when combined (shown in Figure 2.7). This region is large enough to include the entire shear layers and extends into their flat velocity regions.

The optical setup is designed in a fashion to allow for both the laser optics and cameras to translate concurrently in the streamwise directions. Additionally the camera setup can move independently in the cross stream direction to be able to cover different regions in the width of the test section, when needed. A smaller traverse system provides the capability to move the laser

optics relative to the camera optics in the streamwise directions, to make it possible to further fine-tune the placement of the tagging lines in the camera fields of view.

For each flow condition, the streamwise component of the flow velocity is measured at multiple downstream locations to characterize the streamwise behavior and downstream development of the shear layers. At each downstream position, undelayed images are taken a short time ($\sim$2 µs) after the laser fires to provide the initial pattern location. Delayed images are taken 8 ms after the first images to produce the displaced patterns. This time delay is selected based on the spatial resolution of the optical setup and the average speed of the flow to result in an average displacement of $\sim$7 pixels in the tagged regions. Based on camera limitations, the image acquisition rate was set at 6.27 Hz during all of velocimetry measurements in this work.

In the current implementation of 1c-MTV, corresponding undelayed and delayed images are not acquired from the exact same laser pulse. Instead, separate sets of undelayed and delayed images are recorded separately and then each of the individual delayed images is correlated to the average of the set of undelayed images. This approach is acceptable based on the assumption that the timing jitter and pulse to pulse pointing instability of the laser are random and their contributions are negligible compared to the displacement between the undelayed and delayed images. Additionally, it is assumed that the exposure time of the undelayed images are short enough that the instantaneous intensity profiles of the tagged lines hardly change duo to flow fluctuations and these profiles are very close to their average representation. Any deviation from these premises will manifest as an increase in the measured velocity fluctuations of the flow. This increase can be approximated by performing a similar correlation between the instantaneous undelayed images and their mean. The fluctuations levels extracted from these undelayed correlations can serve as an estimate of the uncertainties in instantaneous streamwise velocities due to the combined effect of processing noise and using the average undelayed image. A set of 512 undelayed images used in these measurements are found to result in an associated uncertainty of less than 0.057 cm/s for instantaneous streamwise velocity measurements. By acquiring a set of 2048 delayed images, this translates into an uncertainty of 0.0025 cm/s in mean streamwise velocity values.

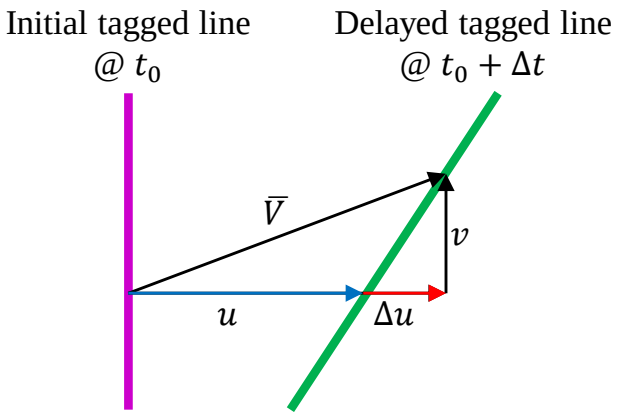

Figure 2.8: A schematic of how a velocity component parallel to a tagged line can generate an error in the velocity normal to the line in 1c-MTV.

The image processing procedure used here is similar to the one used by Katz (2010) and further improved upon by Olson (2011), which performs a line-by-line, row-by-row cross correlation between the intensity fields of undelayed and delayed tagged lines and then utilizes a 7th order polynomial fit to find the peak of the correlation map with sub-pixel accuracy. For more accurate values of velocity fluctuations in flow, The contributions of white noise (from both camera and processing) to the fluctuating velocity measurements are removed by using autocorrelation of the instantaneous velocity time-series, as proposed by Olson (2011).

Due to the inherent assumption of unidirectional flow in 1c-MTV technique, it is prone to errors when there is a component of velocity parallel to the tagged lines, (as illustrated in Figure 2.8). Following the analysis of Hill & Klewicki (1996), this error in measured instantaneous streamwise velocity over time delay Δt can be expressed as:

$$\frac{\Delta u}{u} = \frac{v}{u}\frac{du}{dy}\Delta t, \tag{2.3}$$

where u and v represent the instantaneous streamwise and cross-stream velocity components, and du/dy is the instantaneous streamwise velocity gradient.

2.3.3 Single Component MTV for Airfoil Boundary Layer Characterization

Similar to the works of Katz (2010), Olson (2011) and Olson et al. (2013, 2015) 1c-MTV is utilized to measure the streamwise component of flow velocity at a very high spatial resolution in the

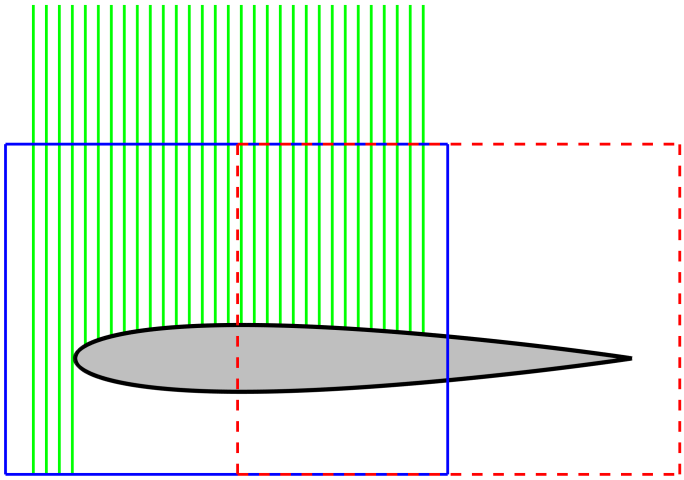

Figure 2.9: A schematic of field of view size and the optical setup for airfoil boundary layer velocimetry. The solid and dashed lines illustrate the two different fields of views used for these measurements.

immediate proximity of airfoil surface. This technique takes advantage of the fact that the MTV images are captured with a short delay after each laser pulse and hence there is no significant wall glare obstructing the view close to the surface.

The laser optics and camera setup are similar to the one described in the previous subsection. The only difference in the laser optics setup is that the laser sheet is passed through another set of cylindrical lenses to expand the width of the sheet before going through a beam blocker. This generates a series of 31 laser lines each 0.7 mm thick (FWHM) and spaced 2.8 mm from each other. For these measurements, only a single camera is utilized which is positioned closer to the plane of interest and uses a 58 mm lens (f/1.2 Nikkor) to produce a more zoomed up field of view approximately 9.5 cm $\times$ 7.1 cm (with a resolution of $\sim$68 µm/px).

These near wall measurements are performed for the airfoil positioned at different angles of attack in each shear flow. Since the size of this setup's field of view (and laser sheet width) is smaller than the chord length of the airfoil, for each case two field of views are required to cover the entire surface of the airfoil. Figure 2.9 shows a sketch of this optical configuration. For each field of view, a set of 512 undelayed and 4096 delayed images are recorded with a 5 ms delay (to generate $\sim$ 7 pixels nominal displacement) between them at a rate of 6.27 Hz.

These images are processed in a similar fashion to the single component measurements for shear layer characterization described in the previous subsection. After processing, the location of the surface of the airfoil at each tagged line is found manually based on the raw images as well as recovered velocity profiles. Furthermore, the measurement points at which the interrogation window is partially blocked by the airfoil surface or affected by the glare from the airfoil surface have been removed.

Since the quartz windows are installed only on one side of the water tunnel facility, UV optical access is only possible from one direction into the test section. This limits the optical access for measurements to only one side of the airfoil. To compensate for this and acquire flow velocities from the opposite side as well, the orientation of the shear flow itself can be adjusted through modifying the placement shear generation devices. This strategy can provide flow information in the proximity of both the suction and pressure sides of the airfoil when it is positioned at either negative of positive angles of attack in a positive shear flow.

2.3.4 Molecular Tagging Flow Visualization for Airfoil Wake Visualization

The same laser optics and camera setup described in the previous subsection is used to visualize the wake flow behind an oscillating airfoil, similar to the work of Koochesfahani & Bohl (2002). The optical setup is moved to tag and record the region just downstream of the the airfoil trailing edge and delayed images are acquired for a range of airfoil oscillation parameters. In order to enhance the flow features through large distortions of the tagged lines, a delay time of 30 ms is used in these measurements.

Since this delay time of 30 ms is well beyond the nominal lifetime of the MTV solution, the camera pixels are binned 2×2 to improve image quality and acquisition rate. This results in a resolution of $\sim$136 µm/px and a sampling rate of 12.27 Hz. For each airfoil motion case in each flow, the airfoil is allowed to oscillate the larger of 10 airfoil convective times or 60 airfoil oscillation periods and then 1024 delayed images are acquired. The instantaneous position of the airfoil at each frame is also recorded, which is later used to phase order the images based on airfoil oscillation

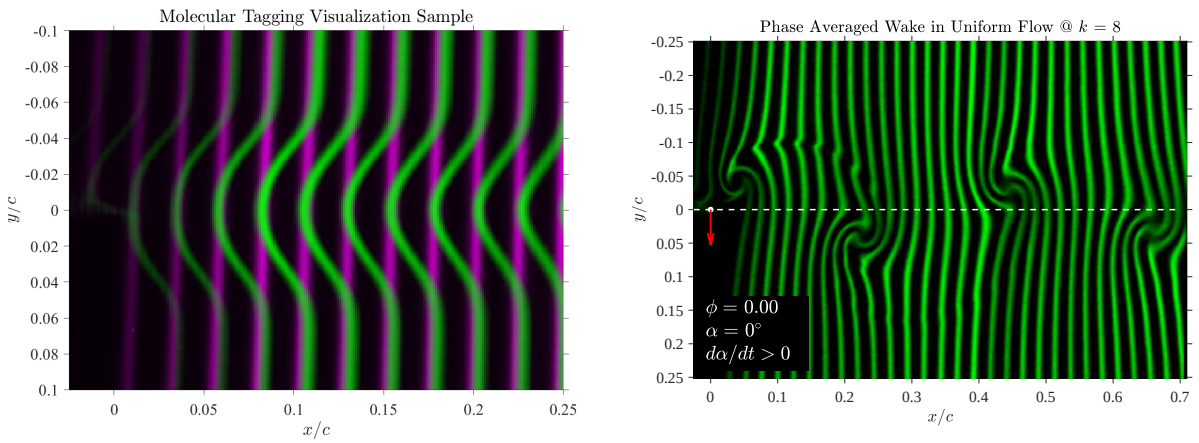

(a) (b)

Figure 2.10: **(a)** A sample pair of molecular tagging flow visualization tagging lines shown at initial (violet) and delayed (green) states in the wake of a stationary airfoil in a uniform flow. The initial image is taken $\sim 2\mu s$ after the laser pulse, while the delayed image is captured 30 ms after the laser pulse. **(b)** Phase averaged molecular tagging visualization of the flow in the wake of an oscillating NACA0012 airfoil with oscillation amplitude of $\alpha_0 = 2$ at a reduced frequency of $k = 8$ in uniform flow at 4 different phases of one airfoil oscillation cycle. The origin prescribes the location of the airfoil trailing edge.

frequency. A 2D median filter with a 3×3 filter size is used to reduce image noise before phase averaging.

Figure 2.10a shows a blown up demonstration of the amount of displacement observed between the undelayed tagged lines and the 30 ms delayed images behind a static airfoil set at zero angle of attack. A sample image of phase averaged wake flow behind an oscillating airfoil is also presented in Figure 2.10b.

2.4 Force Measurement Setup

The force measurement setup consists of an ATI mini 40 six-component force/torque sensor which is assembled so that it connects the NACA 0012 airfoil to the pitching motor. This setup (shown in Figure 2.11) was designed and assembled by Dr. David Olson and was used for force measurements performed in Olson et al. (2016) and Hammer et al. (2019). Present study only utilizes the lift and drag force readings for both the stationary and pitching airfoil measurements.

In the case of force measurements on a stationary airfoil, drag and lift forces are measured over

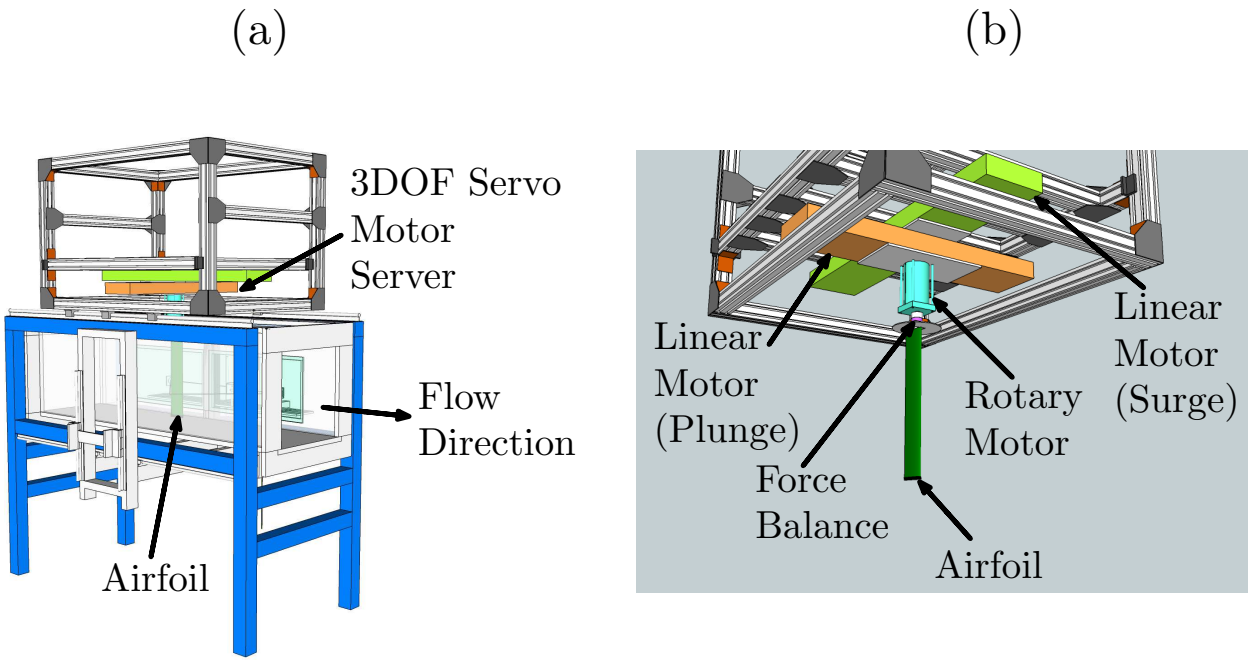

Figure 2.11: **(a)** 3D model of the water tunnel test section, depicting the vertical airfoil mounted to the 3DOF motion system on top of the test section. **(b)** Details of the 3DOF system and airfoil mounting. (Figures courtesy of Hammer et al., 2019)

a range of angles of attack with the following procedure repeated for each angle of attack:

1. With the water tunnel turned off, the airfoil is set to the prescribed angle of attack.
2. 20 seconds wait to make sure any vibrations from the airfoil motion have diminished.
3. With the tunnel still off, forces are measured for 120 s to establish an initial bias measurements.
4. Tunnel is turned on with a 3 minutes wait for everything to reach a steady state.
5. The aerodynamic forces are measured for 180 s
6. Tunnel is turned off again with a 3 minutes wait for everything to settle down.
7. With the tunnel off, forces are measured for 120 s to establish a post-measurement bias.

The initial and final bias measurements are used to remove the bias error and quantify the drift of the sensor during each measurement. Additionally, the measurement duration is designed to be

less than 15 minutes for each case to minimize the impact of sensor drift (to within the measurement resolution). The reported instantaneous resolution according to the sensor specifications is 0.005 N for lift and drag measurements, corresponding to a resolution of 0.014 in lift and drag coefficients (based on the measurement operating parameters). Hammer et al. (2019) have found the uncertainty of the mean force coefficient measurements to be dominated by sensor drift during each measurement with an estimated value of 0.005 in normalized coefficients. During the course of these measurements the original sensor was damaged and replaced. While the replacement sensor was the exact same model, it was observed that the new sensor occasionally experienced slightly larger magnitudes of drift.

A similar procedure is performed for pitching airfoil measurements with the airfoil oscillating over a range of oscillation amplitudes and frequencies:

1. With the water tunnel turned off, the airfoil is set to the prescribed mean angle of attack.
2. 20 seconds wait to make sure any vibrations from the airfoil motion have diminished.
3. With the tunnel still off, forces are measured for 60 s to establish an initial bias measurements.
4. Tunnel is turned on with a 3 minutes wait for everything to reach a steady state.
5. With the tunnel on, aerodynamic forces on the stationary airfoil at mean angle of attack are measured for 120 s.
6. The airfoil starts oscillation with the prescribed motion parameters.
7. After a wait of 10 convective times plus 20 airfoil oscillation periods, the unsteady aerodynamic forces are measured for 180 s
8. Tunnel is turned off again with a 3 minutes wait for everything to settle down.
9. With the tunnel off, forces are measured for 60 s to establish a post-measurement bias.

Force measurement data for the static airfoil in the reference uniform approach flow is used to establish the reference zero angle of attack in the setup. This is the angle at which the net force

(in the plane normal to airfoil span) on the airfoil is at its minimum magnitude. The symmetry of the lift and drag forces of the same data set are utilized to find and correct for any possible small misalignments between the axis of the sensor and flow coordinates. All of the reported force measurement are performed with a sampling rate of 2 kHz.

Hammer et al. (2019) measured the inertia forces due to any slight misalignment between the center of mass of the airfoil (including the support shaft and other components) and the pitching axis by pitching the airfoil in air. They found that the contributions of inertia forces to the *mean* forces were negligible due to harmonic nature of the motion. However, these inertia forces resulted in an increase of ~0.15 in lift coefficient fluctuations and 0.016 for drag/thrust coefficient fluctuations in their measurements.

For oscillating airfoil measurements, frequencies beyond 5 times the oscillation frequency and the setup natural frequency are removed from the raw data before calculating the reported statistical data. These filtered data are also phase ordered and phase averaged based on the recorded motion of the airfoil.

CHAPTER 3

SHEAR GENERATION RESULTS

Figure 3.1 depicts a schematic of the family of plane mixing layers that are studied in this work. In the classical two-stream shear layers, two plane flows (streams) with uniform velocities U_1 and U_2 are initially separated by a splitter plate. These two parallel streams come together as the splitter plate ends at $x = 0$ and the streams begin to mix. The resulting shear layer grows from this velocity difference and widens as it flows downstream. This flow initially entails a wake profile due to the presence of the splitter plate, but as it develops downstream, the wake component dissipates and the flow approaches self-similarity in variable $\eta = cy/x$ far enough downstream.

A typical average streamwise velocity of two-stream shear layers in the self-similar region is presented in Figure 3.2. This mean velocity profile can usually be approximated by a hyperbolic tangent profile, where the centerline of the profile is defined as the y location where the velocity is equal to the centerline (or average) velocity, $U_c = \dfrac{U_1 + U_2}{2}$. There are two widely used parameters to describe the width, or thickness, of the shear layer at each downstream location: momentum

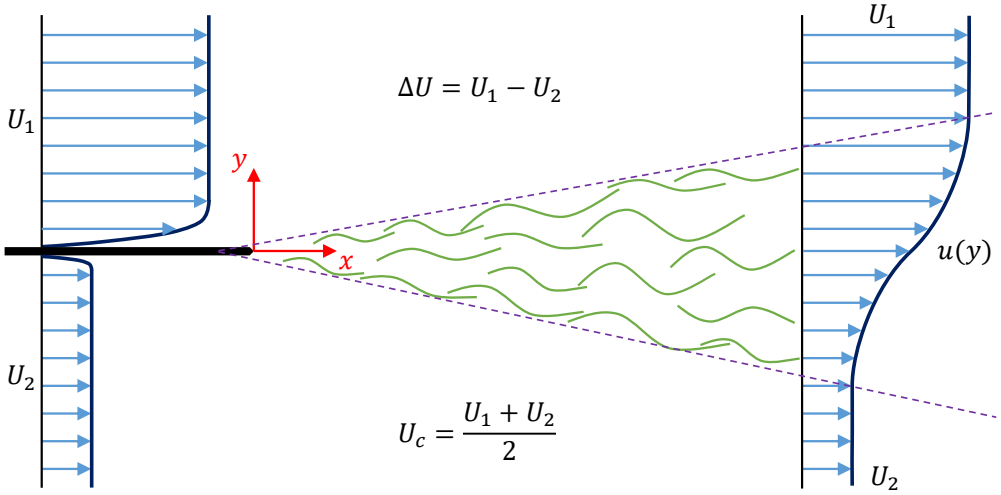

Figure 3.1: A schematic of a plane mixing layer.

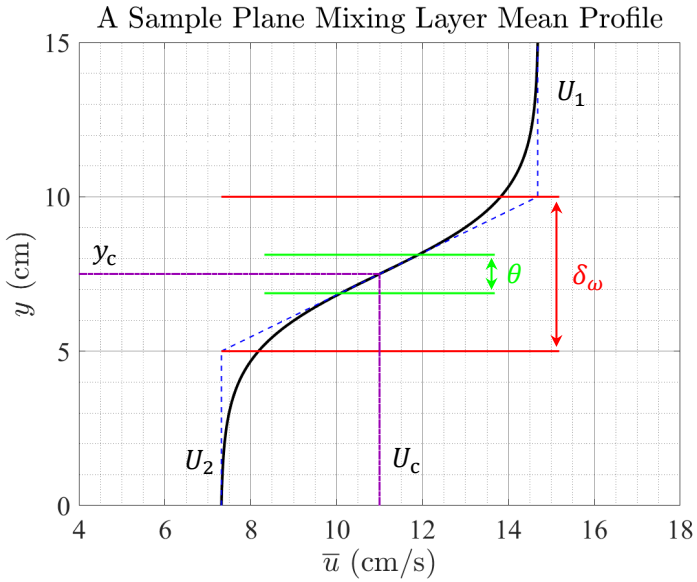

Figure 3.2: A sample plane mixing layer mean velocity profile.

thickness, θ, and vorticity thickness, δ_ω, each defined as follows:

$$\theta = \int_{-\infty}^{+\infty} \left[\frac{U_1 - u(y)}{\Delta U}\right]\left[\frac{u(y) - U_2}{\Delta U}\right] dy\,, \tag{3.1}$$

$$\delta_\omega = \frac{\Delta U}{\left(\frac{\partial u}{\partial y}\right)_{max}}\,. \tag{3.2}$$

Using either of these definitions for shear layer thickness, it has been shown that the shear layer spreads linearly with downstream distance. Here, vorticity thickness will be used as the measure of shear layer thickness, which for a hyperbolic tangent profile is 4 times larger than the momentum thickness. Brown & Roshko (1974) reported that the growth rate of the vorticity thickness can be approximated by:

$$\frac{d\delta_\omega}{dx} = \frac{\delta_\omega}{x - x_0} = 0.181\lambda\,, \tag{3.3}$$

where, x_0 is the apparent origin and λ represents the velocity difference parameter, as proposed by Abramovich (1963) and Sabin (1965):

$$\lambda = \frac{U_1 - U_2}{U_1 + U_2}\,. \tag{3.4}$$

The shift of origin to x_0 is mostly to correct for the effects of finite boundary layer thickness on the splitter plate at $x = 0$. The magnitude and sign of this offset in origin is highly dependent on the initial boundary conditions at the edge of the splitter plate.

3.1 Unsteady Shear Flow Characterization

As the unsteady shear approach flow in this work, behavior and development of the two-stream shear layer is studied by measuring its streamwise velocity profile as a function of distance from splitter plate, utilizing 1c-MTV. Figure 3.3 depicts the development of the mean and fluctuating velocity profiles of the shear layer at select downstream locations. It is observed that right at the edge of the splitter plate (black line in Figure 3.3a), the flow consists of two uniform velocity profiles of different magnitudes, separated by a wake profile resulting from the presence of the splitter plate. The slightly rippled profile at the lower velocity side is due to the fact that this stream has not had enough space to completely recover from the initial jets coming out of the honeycomb and the remnants of these jets are still present in the flow. These non-uniformities are also visible in the fluctuating velocity profile at this location (see Figure 3.3b).

Traveling downstream from the splitter plate, both the wake component and non-uniformities on the low speed side of the mean velocity profile disappear rather quickly, after a distance of ~20 cm (red line in Figure 3.3a). From this point on, the mean velocity profiles in Figure 3.3a exhibit the typical shape of the plane mixing layers, with the shear layer widening as it continues downstream. The fluctuating velocity profiles in Figure 3.3b also show the expected behavior of the temporal

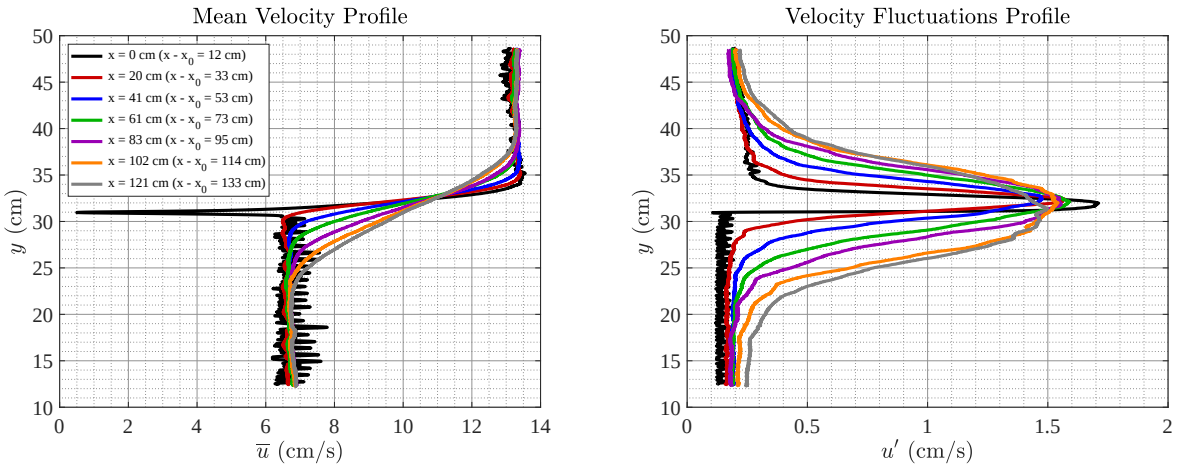

(a) (b)

Figure 3.3: Development of the streamwise **(a)** mean and **(b)** fluctuating velocity profiles in the two-stream shear layer.

fluctuations in two-stream shear layers, with the maximum magnitude of the fluctuation around the center of the shear layer and gradual decrease in fluctuations moving away from the center of the shear layer. Outside the shear layer, the amplitude of fluctuations drops down to the level of background fluctuation present in the test facility. The growth of the shear layer is also noticeable in the velocity fluctuation profiles.

Figure 3.4 illustrates the linear growth of the generated two-stream shear layer through development of vorticity thickness (Figure 3.4a) and shear layer centerline location (Figure 3.4b). A linear fit to the calculated values of vorticity thickness is used to estimate the growth rate, $d\delta_\omega/dx$, and apparent origin, x_0, of the shear layer. The growth rate of this shear layer is found to be $d\delta_\omega/dx = 0.071 = 0.208\lambda$, where $\lambda = 0.34$. This value is consistent with the growth rate reported by Brown & Roshko (1974), $d\delta_\omega/dx = 0.181\lambda$. The slight inclination of the shear layer centerline location towards the low speed side is demonstrated in Figure 3.4b, which is a known behavior of the canonical shear layers.

The normalized behavior of the two-stream shear layer mean and fluctuating velocity profiles are presented in Figure 3.5. The self-similar nature of this shear layer is evident from the fact that the properly normalized curves from different downstream locations fall on top of each other,

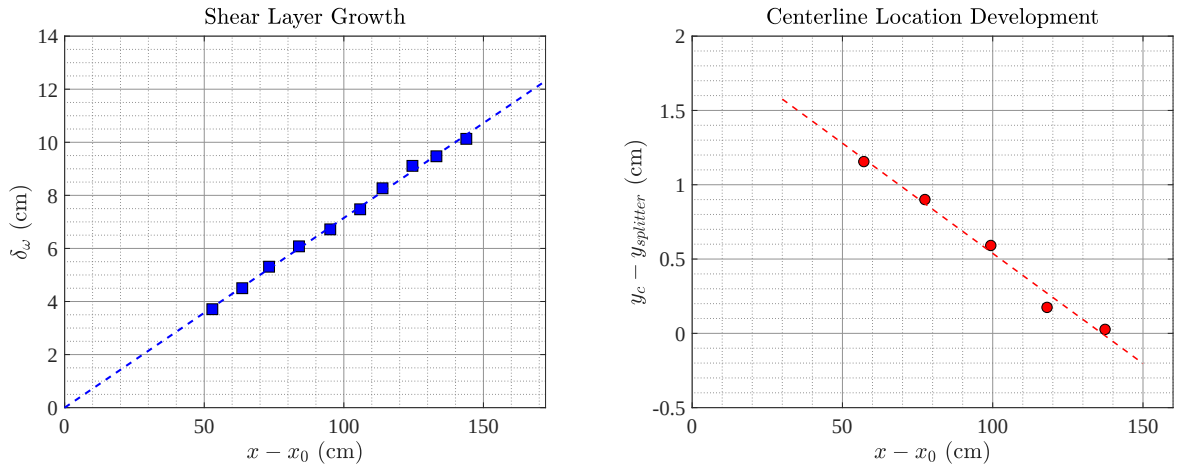

(a) (b)

Figure 3.4: **(a)** Development of the unsteady shear layer vorticity thickness, δ_ω. **(b)** Inclination of unsteady shear layer centerline position towards the low speed side.

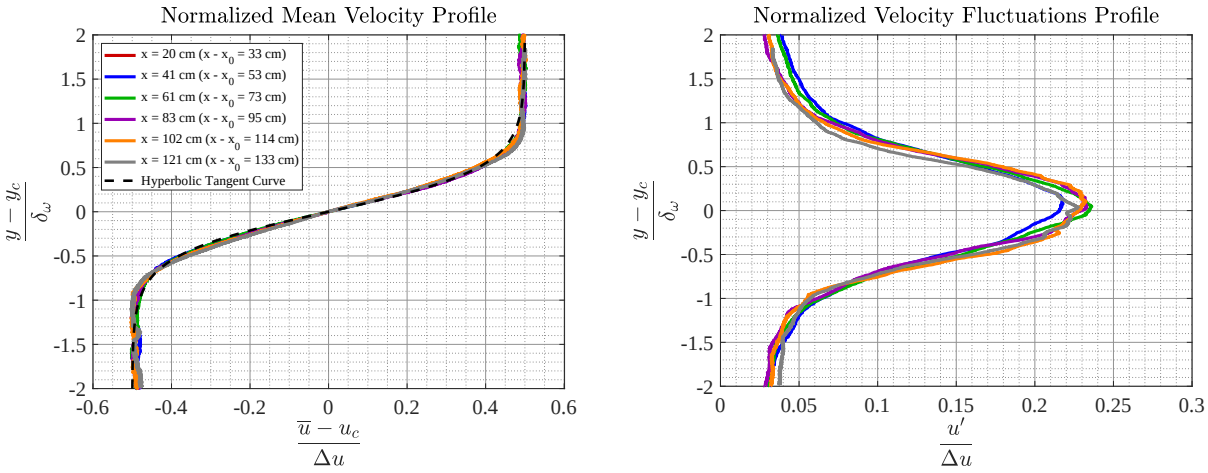

(a) (b)

Figure 3.5: Self-similar behavior of the normalized streamwise **(a)** mean and **(b)** fluctuating velocity profiles in the two-stream shear layer.

for both the mean and fluctuating velocity profiles. For comparison, a hyperbolic tangent profile is superposed on the mean velocity profiles in Figure 3.5a. The shear layer Reynolds number based on vorticity thickness and velocity difference $\left(Re_{\delta_\omega} = \frac{\Delta U \delta_\omega}{\nu}\right)$ values range from 2700 to 6800 for the locations shown in Figure 3.5. It is worth mentioning that the maximum value of measured normalized fluctuating velocity, $(u'/\Delta U)_{\max} = 0.23$, is higher compared to the reported value of 0.17 in the literature typical for these flows. This discrepancy could be due to the errors introduced by the instantaneous values of lateral component of velocity, v, into the instantaneous measurements of the streamwise velocity.

Parameter	Value	Parameter	Value
U_1	13.35 cm/s	$\frac{U_1}{U_2}$	2.01
U_2	6.65 cm/s	$\left(\frac{u'}{\Delta U}\right)_{\max}$	0.23
U_c	10.00 cm/s	λ	0.34
ΔU	6.71 cm/s	$\frac{d\delta_\omega}{dx}$	0.208λ

Table 3.1: Characteristic parameters derived for the two-stream shear layer. Displayed values are average values based on multiple measurements in the self-similar region.

More relevant parameters derived from the generated two-stream shear layer are presented in Table 3.1. It should be noted that the displayed values are average values based on all the self-similar measurements at various downstream locations.

3.2 Steady Shear Flow Characterization

In order to isolate the effects of shear flow unsteadiness from those of the mean shear, a steady shear layer is generated to match the mean streamwise velocity profile of the two-stream shear layer at a specific location. For this purpose, the mean velocity profile of the two-stream shear layer at 94 cm downstream of the splitter plate ($x - x_0 = 107$ cm) is selected as the reference mean velocity profile. The modified shaped honeycomb model (described in Appendix A) is used to design a variable length honeycomb device to produce this desired velocity profile. Figure 3.6 presents the mean and fluctuating velocity profiles of this generated steady shear layer, compared to those of the reference two-stream shear layer. It is observed that while the mean velocity profile of the steady shear layer is very similar to the unsteady shear layer, their fluctuating velocity profiles are distinctively different. The fluctuations of the steady shear layer are spatially uniform and at the level of the background fluctuations in the test facility, in contrast to the bell shaped profile of the fluctuations in the unsteady shear layer which reaches amplitudes as high as 7 times the background

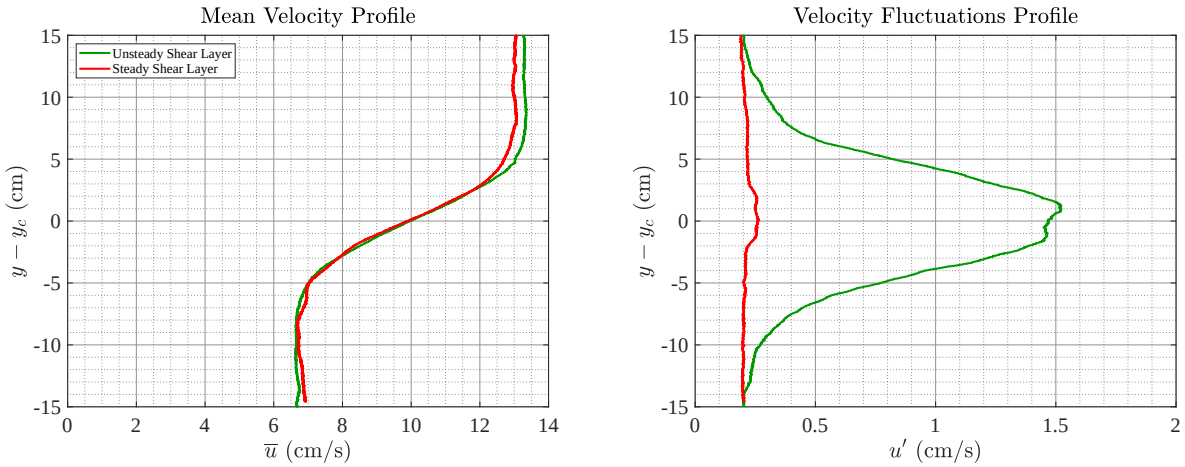

(a) (b)

Figure 3.6: Comparison of the streamwise **(a)** mean and **(b)** fluctuating velocity profiles in the steady shear layer versus the reference unsteady shear layer.

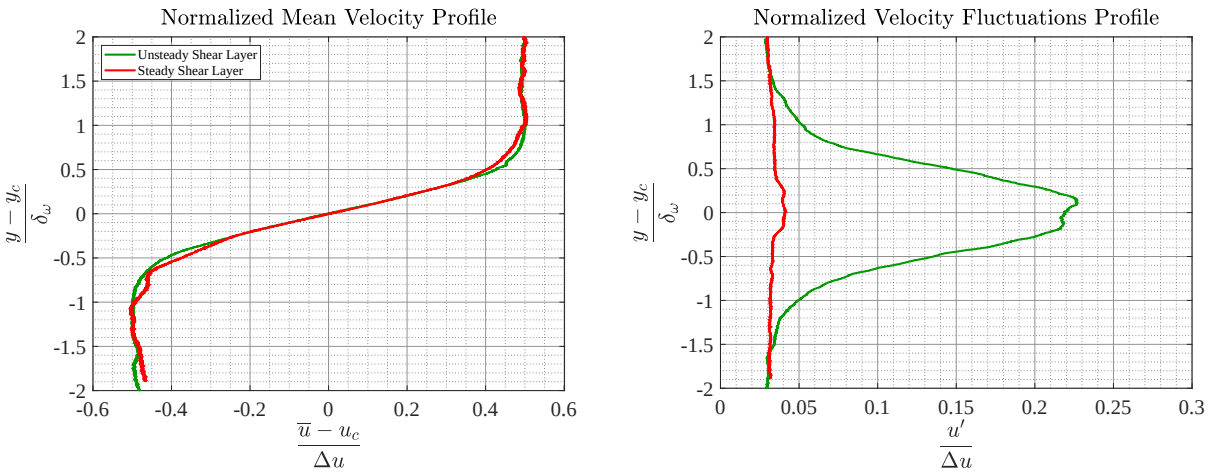

(a) (b)

Figure 3.7: Comparison of the normalized streamwise **(a)** mean and **(b)** fluctuating velocity profiles in the steady shear layer versus the reference unsteady shear layer.

fluctuations level.

Figure 3.7 further highlights the similarity of the mean velocity and the contrast in fluctuations profile through showing the normalized mean and fluctuating velocity profiles for both the steady and unsteady shear layers. A more detailed comparison of these two shear layers in terms of their characteristic parameters is provided in Table 3.2. Based on these observations, the two shear layers discussed here will be used as the pair of matching shear layers for all of the ensuing force measurements and velocimetry experiments carried out in this project. From hereon, the terms ***steady shear layer*** and ***unsteady shear layer*** will simply refer to these shear layers, unless stated otherwise.

Although the steady shear layer generated through the shaped length honeycomb method is not expected to grow as it flows downstream, its development is investigated to better characterize its behavior. Figure 3.8 depicts the mean and fluctuating velocity profiles measured at multiple downstream locations (x values measured from the honeycomb exit plane). Figure 3.8a suggests that the mean velocity profile of the steady shear layer remains almost identical as it progresses downstream. The slight increase in the fluctuations level at the center of the shear layer (~10% as shown in Figure 3.8b) indicates that given enough traveling distance, this steady shear layer could become unstable. To avoid any complications due to flow instability, all the subsequent

Parameter	Unsteady Shear Layer	Steady Shear Layer	Relative Difference
U_1	13.34 cm/s	13.14 cm/s	1.08 %
U_2	6.64 cm/s	6.79 cm/s	2.33 %
U_c	9.99 cm/s	9.96 cm/s	0.26 %
ΔU	6.71 cm/s	6.35 cm/s	5.40 %
δ_ω	8.62 cm	7.82 cm	9.26 %
$\frac{U_1}{U_2}$	2.01	1.94	3.8 %
λ	0.34	0.32	5.15 %
$\left(\frac{u'}{\Delta U}\right)_{\max}$	0.23	0.04	82.61 %

Table 3.2: A comparison between the characteristics of the steady versus unsteady shear layer. The values for unsteady shear layer are extracted from the two-stream shear layer mean velocity profile measured at 94 cm downstream of the splitter plate ($x - x_0 = 107$ cm).

measurements for the steady shear layer are performed within downstream distances shown in Figure 3.8.

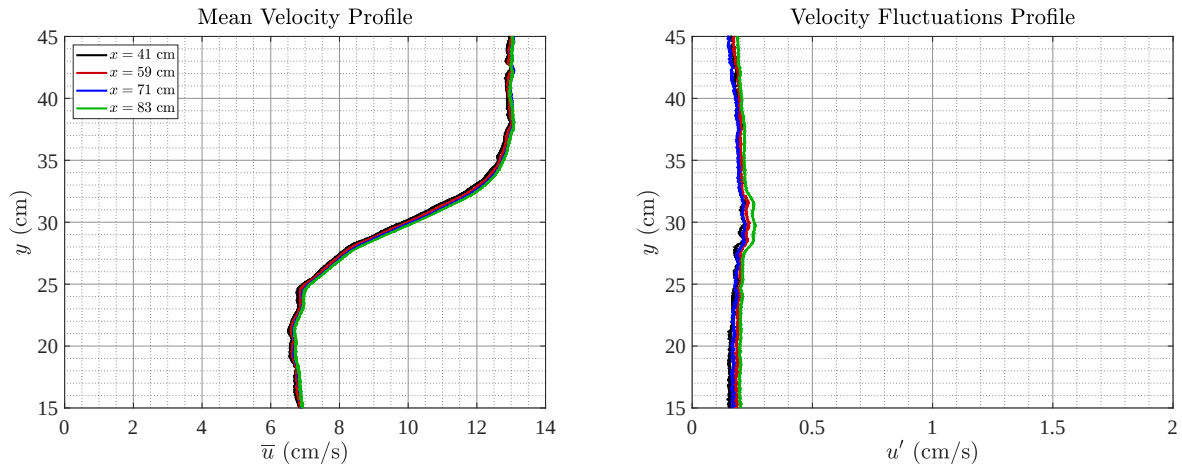

(a) (b)

Figure 3.8: Development of the streamwise **(a)** mean and **(b)** fluctuating velocity profiles in the steady shear layer.

3.3 Sensitivity of Shear Flows to Downstream Perturbations

It is well known that the evolution of two-stream shear layers can be strongly affected by perturbations introduced to the flow, and at high forcing frequencies, downstream disturbances can even influence the behavior of vortical structures of the two-stream shear layer up to the trailing edge of splitter plate (Ho & Huerre, 1984; Koochesfahani & Dimotakis, 1989). Therefor, before looking at the effects of these shear layers on aerodynamic performance of static and oscillating airfoils, it is beneficial to first investigate how the perturbations due to airfoil oscillations might affect the shear layer itself (i.e. does pitching the airfoil change the upstream boundary condition?). This issue is investigated by measuring the streamwise velocity profile of the shear layers upstream of the airfoil (two airfoil chord lengths upstream of the airfoil leading edge), when the NACA 0012 airfoil is placed at the center of the shear layer and oscillates around its quarter chord point with a range of oscillation amplitudes and frequencies. These sensitivity measurements are carried out for both of the shear layers and at multiple airfoil downstream placements for the unsteady shear layer.

Figure 3.9 presents normalized mean and fluctuating velocity profiles measured two chord

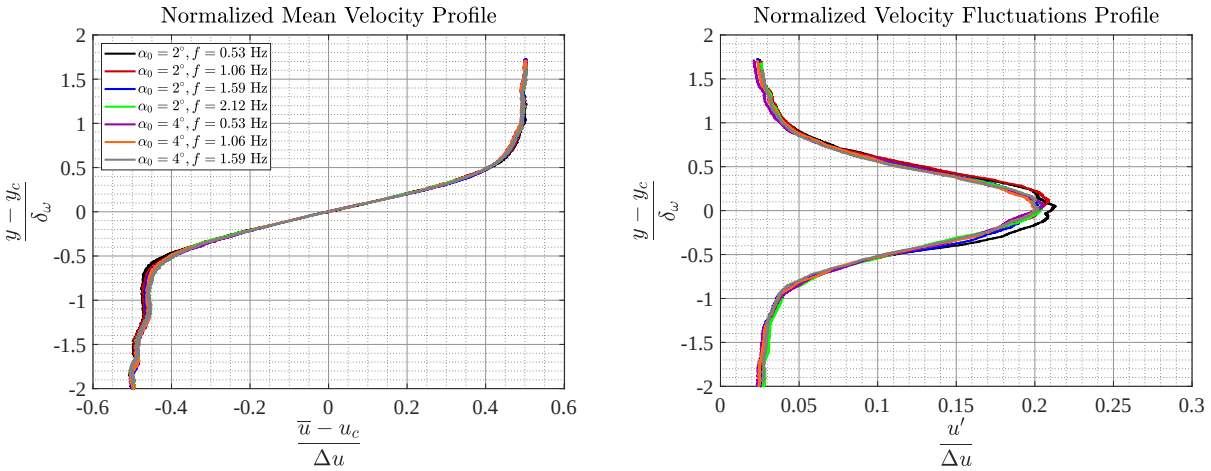

(a) (b)

Figure 3.9: Effect of airfoil oscillation on mean **(a)** and fluctuating **(b)** velocity profiles two chord upstream of the airfoil leading edge when airfoil is located at $x = 94$ cm in the two-stream shear layer.

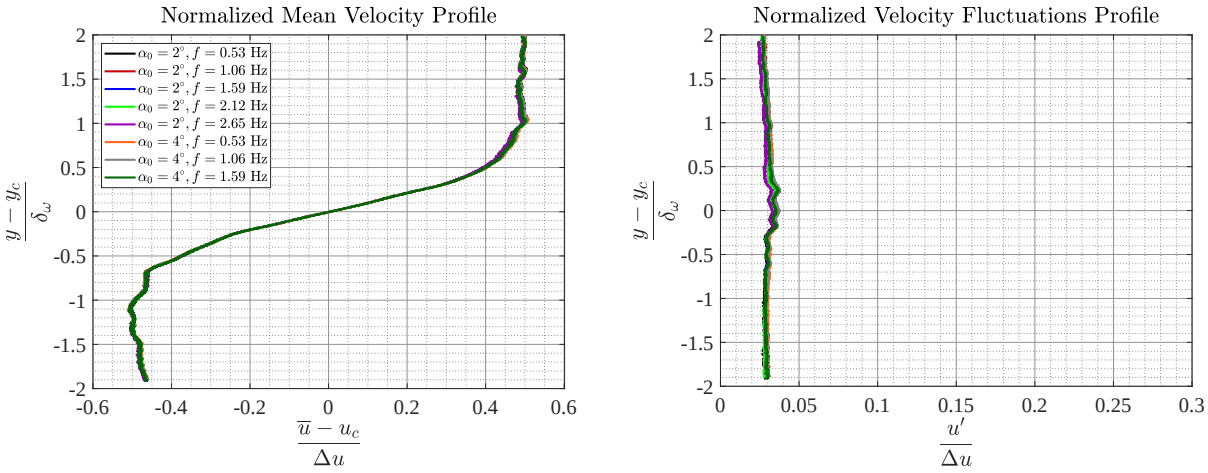

(a) (b)

Figure 3.10: Effect of airfoil oscillation on mean **(a)** and fluctuating **(b)** velocity profiles two chord upstream of the airfoil leading edge when airfoil is located in the steady shear layer.

lengths upstream of the airfoil when airfoil was placed in the center of the unsteady shear layer at downstream location $x = 94$ cm (the designated unsteady shear layer location), for select oscillation amplitude and frequency combinations. It is observed that the perturbations introduced by the pitching airfoil have no noticeable effect on the behavior of both mean and fluctuating velocity profiles of the unsteady shear layer two chord lengths upstream of the airfoil. While these plots only show the results for the airfoil positioned at $x = 94$ cm, similar measurements at locations further downstream with thicker and upstream with thinner unsteady shear layers did not show any effect on the normalized mean and fluctuating velocity behavior upstream of the airfoil either. The results of these measurements along with the effects of stationary airfoil positioned at different angles of attack on the upstream shear flow are provided in Appendix B.

Repeating these measurements with the airfoil placed at the center of the steady shear layer resulted in a similar conclusion (See Figure 3.10 for velocity profiles measured at two chord lengths upstream). Again, airfoil oscillations do not change the normalized mean and fluctuating velocity behavior upstream of the airfoil.

According to these results, placing and pitching the airfoil at the center of these shear layers does not affect the upstream flow boundary condition. This means that since the upstream boundary conditions are independent of airfoil oscillation frequency and amplitude, unsteady force

measurements for pitching airfoils should only reflect the effects of the airfoil oscillation with no ramifications from changes in the approach flow.

CHAPTER 4

AERODYNAMIC FORCE MEASUREMENTS

After establishing the behavior and development of both steady and unsteady shear flows, the load cell setup is used to measure the aerodynamic forces on stationary and oscillating airfoils positioned at the center of each shear layer. Figure 4.1 shows a schematic of the force measurement setup coordinate system used for reporting the aerodynamic forces.

After introduction of the airfoil to the setup, the chord length of the airfoil, c, will be used as the length scale for describing the approach flow and airfoil motion properties. Hence the shear flows are characterized by their non-dimensional maximum (centerline) shear rate of $K = \frac{du}{dy}\frac{c}{U_c} = 1.0$ and normalized thickness of $\frac{\delta_\omega}{c} = 0.7$. The measured lift and drag forces are normalized by the centerline velocity of the shear layer to yield lift and drag coefficients, $C_L = L/(1/2\rho U_c^2 cs)$ and $C_D = D/(1/2\rho U_c^2 cs)$, where s is the airfoil span. The nominal chord Reynolds number of the flow is kept as $Re_c = 12,500$.

In each of the sections on stationary and oscillating airfoils that follows, first the results of the

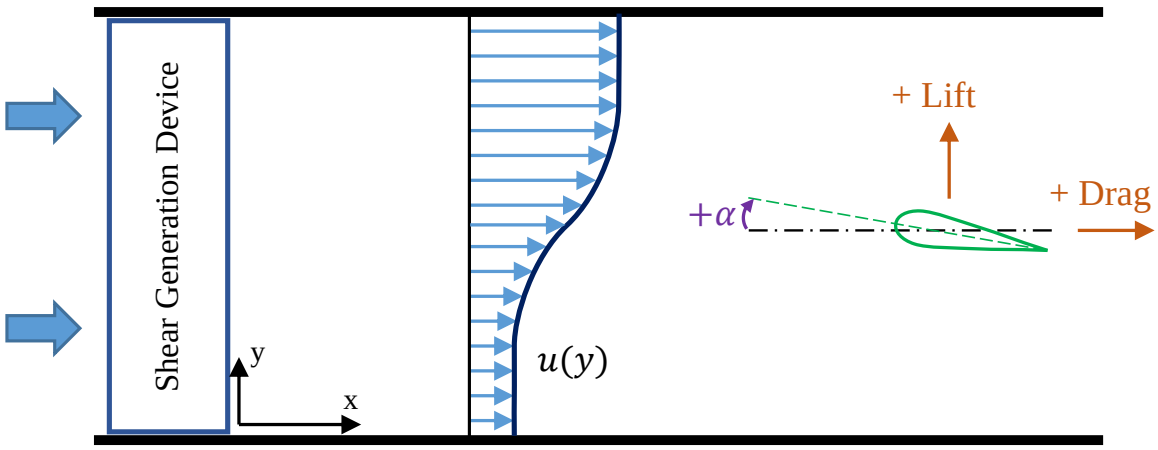

Figure 4.1: Schematic of force measurement coordinate system.

matching steady and unsteady shear layer pair (with $K_{\max} = 1.0$ and $\frac{\delta_\omega}{c} = 0.7$) are compared to each other and the reference uniform flow. Then, the results from only the unsteady shear layer at two more downstream locations (corresponding to $K_{\max} = 1.4$ and $\frac{\delta_\omega}{c} = 0.5$, and $K_{\max} = 0.8$ and $\frac{\delta_\omega}{c} = 0.9$ respectively) are shown to highlight the effects of upstream shear layer width and shear rate.

4.1 Aerodynamic Forces on a Stationary Airfoil

To provide the first insight into the effects of unsteadiness of a shear flow on the aerodynamic performance of a stationary airfoil, the results of force measurements in the steady and unsteady shear flows are compared. Additionally, aerodynamic forces measured for a uniform flow are used as a reference to highlight the main differences duo to the presence of the mean shear itself.

A schematic of the airfoil trailing edge displacement is portrayed in Figure 4.2, where it is overlaid on top of the mean streamwise velocity profile of the shear flows. It is observed that the

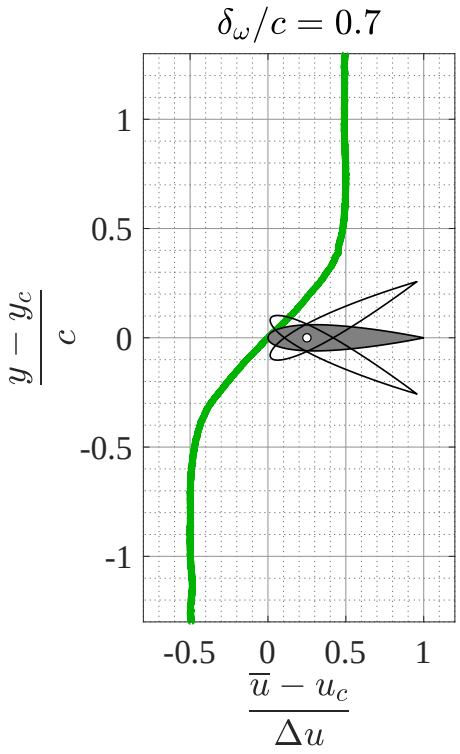

Figure 4.2: Extent of airfoil angular displacement (±20°) compared to the shear layer thickness.

trailing edge of the airfoil spans approximately 65% of the shear layer thickness.

The aerodynamic performance of the stationary airfoil in the shear layers is evaluated through average lift and drag coefficients as well as lift to drag ratio. Here, the symbols show the average values measured over 180s of measurements at each angle of attack, while the error bars indicate the uncertainty of each measurements, which as mentioned in experimental methods chapter, is primarily dominated by drift of the sensor during measurement period. The error bars are mostly within the symbol size, however, there are a few cases that experienced more drift. The effect of these uncertainties is more pronounced in lift to drag ratio plots, according to error propagation.

Figure 4.3a shows that the general trend of the mean lift coefficient curve in steady shear exhibits the typical behavior of the NACA 0012 airfoil in low Reynolds number where the region around zero angle of attack shows a lower slope followed by a region of higher slope at moderate angles, before reaching stall or a plateau at larger angles. This behavior is significantly different in the unsteady shear flow, where it shows a relatively linear behavior across a moderate range of angles of attack and with a larger slope. Both steady and unsteady shear flow curves show an asymmetry in maximum lift coefficient, with a larger amplitude of maximum lift happening at negative angles of attack.

This contrast in behavior of the lift curve in unsteady shear layer can be attributed to the high level of fluctuations present in this flow. The central region of lower slope in the lift curve (as observed in Figure 4.3a for the uniform flow and steady shear layer cases) is usually associated with laminar separation on the surface of the airfoil when it is set at small angles of attack (Cleaver et al., 2010; Wang et al., 2014). This laminar separation is known to be sensitive to flow conditions and Olson (2011) has shown that an increase in free stream turbulence level in a uniform flow can greatly affect the laminar separation bubble by shortening it in both length and height on a SD7003 airfoil. Hence it is possible that the high level of fluctuations in the central region of the unsteady shear layer have affected the development of laminar separation on the airfoil, and consequently, its lift characteristics.

A closer look at the lift coefficient curve around zero angle of attack (Figure 4.3b) shows a

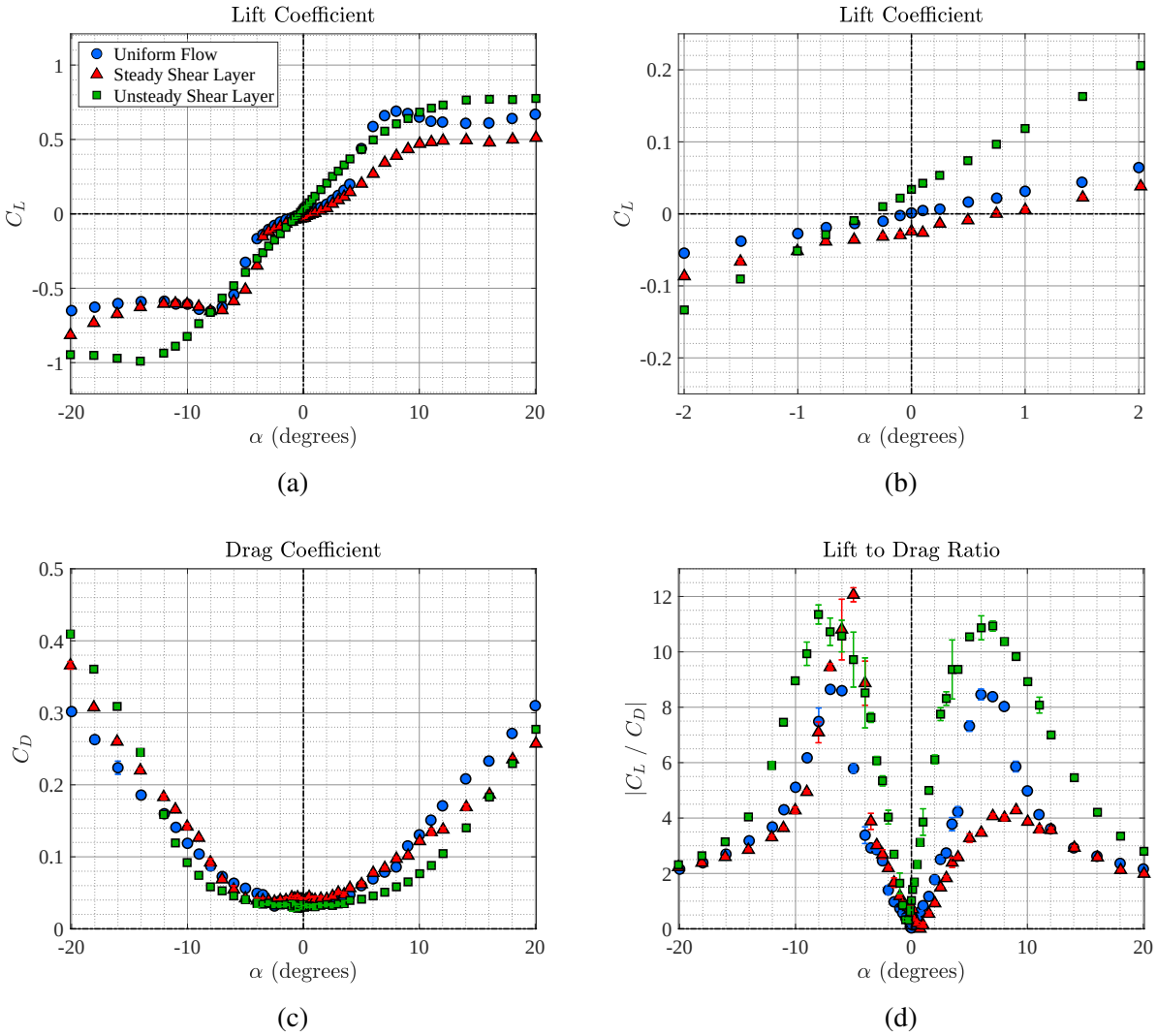

Figure 4.3: Comparison of aerodynamic force coefficients measured on a stationary airfoil placed in uniform, steady shear and unsteady shear flows: **(a)** mean lift coefficient, C_L, **(b)** Zoomed up view of mean lift coefficient, C_L, **(c)** Mean drag coefficient, C_D, **(d)** Ratio of mean lift to mean drag, $\left|\frac{C_L}{C_D}\right|$.

negative lift coefficient at zero angle of attack for steady shear flow, similar to the findings of Hammer et al. (2016, 2018, 2019) and Olson et al. (2016). In contrast, the unsteady shear flow is found to generate a positive lift at zero angle of attack. This change of lift force sign can also be related to the fluctuations of the unsteady shear layer. Hammer et al. (2018, 2019) have hypothesized that in the case of the steady shear layer, the negative lift is a result of asymmetric viscous boundary layer development on the airfoil upper and lower surfaces, which causes a geometrically symmetric

airfoil to effectively behave like one with negative camber. In the case of unsteady shear layer, however, the high level of fluctuations seems to make the flow behave closer to the inviscid theory of Tsien (1943), which predicts a positive lift for a positive shear flow.

The overall behavior of the drag coefficient (Figure 4.3c) for both steady and unsteady shear layers is asymmetric with larger maximum drag coefficients measured at negative angles of attack. The only noticeable difference is that the unsteady shear flow curve exhibits smaller drag coefficients over a larger region of angles of attack, compared to both steady shear layer and uniform flow. This drag reduction is consistent with the hypothesis of the laminar separation being affected by the fluctuations of the unsteady shear layer, since laminar separation is known to increase the drag of the airfoils at low Reynolds number (Lissaman, 1983).

Lift to drag ratio curves are shown in Figure 4.3d, where a large asymmetry in the peak values of lift to drag ratio is noticeable for the case of steady shear layer. Such asymmetry is not perceived in the unsteady shear flow case, which produces an almost symmetrical profile.

Figure 4.4 provides a comparison between the results of the current study in steady shear layer with experimental results of Olson et al. (2016) and numerical results of Hammer et al. (2019). It should be noted that their steady shear flow results are not from a mean velocity profile matching the one in this work, but from a three segmented linear velocity profile (as described in Hammer et al., 2019) with $K = 0.51$, $\delta_\omega/c = 1.7$ and a velocity ratio of $\frac{U_1}{U_2} = 3$ operating at the same centerline velocity, $U_c = 10$ cm/s resulting in a chord Reynolds number of $Re_c = 1.2 \times 10^4$. This velocity profile is shown in Figure 4.5 and compared to shear flows generated in this work. The comparison with these sample steady shear results are only to highlight the similarities in general trends of lift coefficient around zero angle of attack.

The agreement between the force measurements in the steady shear flow with hyperbolic tangent velocity profile generated here and the linear velocity profile of Olson et al. (2016) and Hammer et al. (2019) is very interesting; especially since their shear rate, shear layer thickness and even the shear layer profiles are completely different. From the perspective of shear rate, it is expected that the shear flow with the higher shear rate would produce a larger magnitude of negative lift at

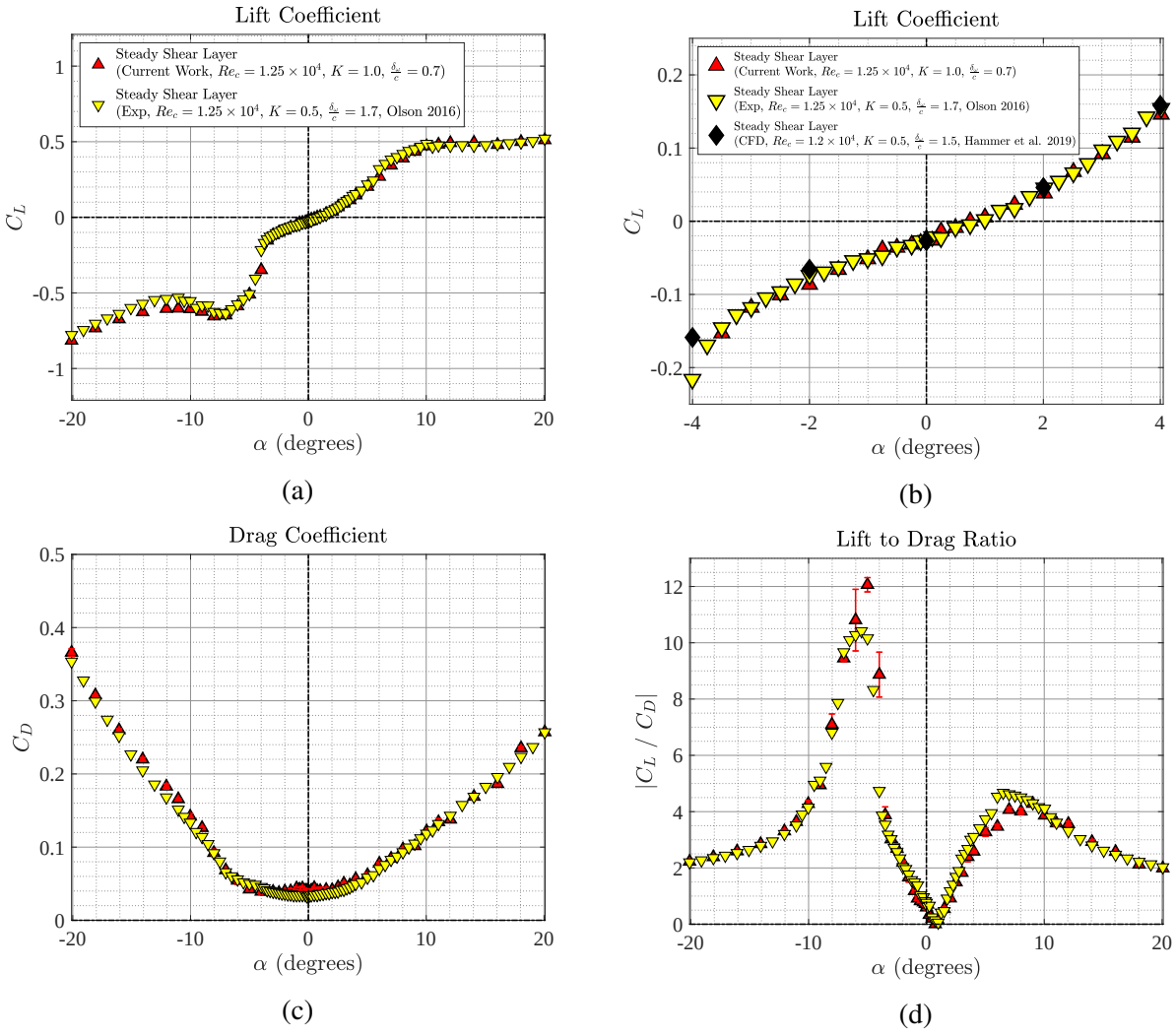

Figure 4.4: Comparison of aerodynamic force coefficients measured on a stationary airfoil placed in the steady shear layer and the results of Olson et al. (2016) and Hammer et al. (2019): **(a)** mean lift coefficient, C_L, **(b)** Zoomed up view of mean lift coefficient, C_L, **(c)** Mean drag coefficient, C_D, **(d)** Ratio of mean lift to mean drag, $\left|\frac{C_L}{C_D}\right|$.

zero angle of attack, due to an increased flow induced asymmetry in the boundary layer thicknesses on the two sides of the airfoil (See Hammer et al., 2018). However, unpublished simulations of Hammer have shown that for a linear velocity profile (similar to the ones used in Olson et al. 2016 and Hammer et al. 2016, 2018, 2019) the magnitude of generated negative lift at zero angle of attack is also dependent on shear layer thickness and increases with $\frac{\delta_\omega}{c}$ until this ratio is large enough that the finite size of the shear zone does not influence the outcome anymore. He found

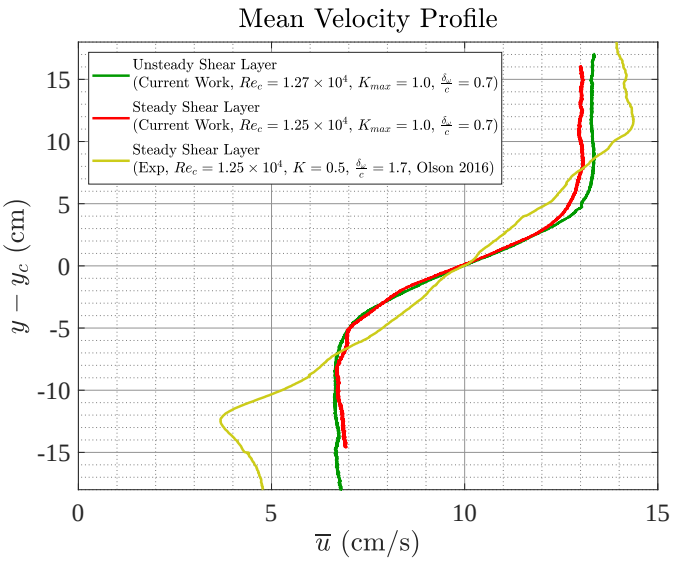

Figure 4.5: Comparison of the shear flow velocity profiles studied in the current study with the linear steady shear used in Olson et al. (2016).

that this happens when $\frac{\delta_\omega}{c} > 2$, which means that the finite thickness of the relatively thin shear layer used here $\left(\frac{\delta_\omega}{c} = 0.7\right)$ would generate a smaller magnitude of negative lift at zero angle of attack. Furthermore, his comparisons of a hyperbolic tangent velocity profile versus a linear velocity profile of the same thickness $\left(\text{both with } \frac{\delta_\omega}{c} = 1.5\right)$ and equal centerline shear rates ($K_{\max}$) showed a slightly smaller magnitude of lift generated by hyperbolic tangent profile at zero angle of attack. This is consistent with the fact that in a hyperbolic tangent velocity profile, the average shear rate over the thickness of airfoil is always smaller than its center line (maximum) shear rate. Consequently, the combination of these opposing effects may have contributed to the similarity of the observed lift force behavior despite the obvious differences between these two shear layers.

4.1.1 Effect of Upstream Unsteady Shear Flow Profile on Aerodynamic Forces on a Stationary Airfoil

This subsection focuses only on the force measurement results in the unsteady shear flow to look at the effect of the downstream positioning of the airfoil in the growing unsteady shear layer. For this purpose, the airfoil is positioned at the center of the two-stream shear layer at three different downstream locations, where both the shear rate and thickness of the shear layer change with this

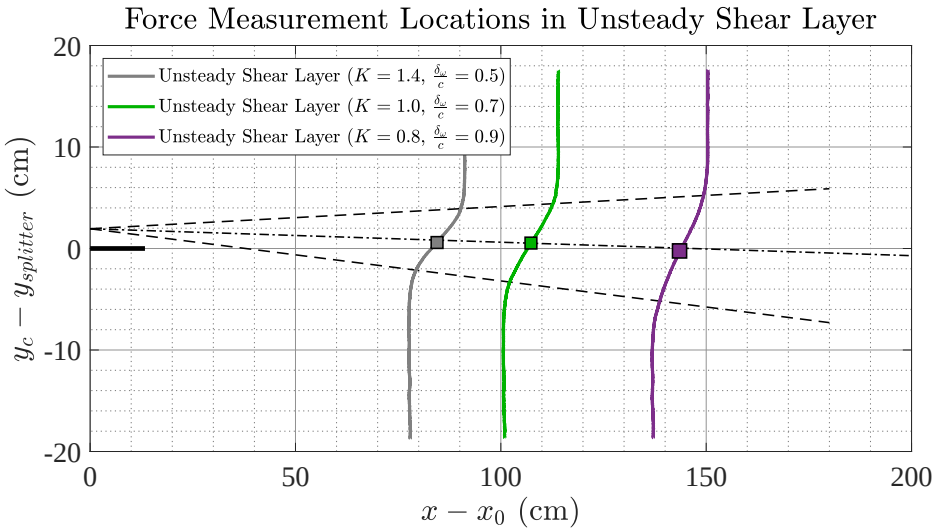

Figure 4.6: Measurement locations for force measurements on stationary airfoil in two-stream shear layer. The symbols show the x locations where force measurements have been performed, with the profiles indicating the measured mean velocity profile at that location.

streamwise position. Figure 4.6 shows the three downstream locations at which force measurements have been performed on the stationary airfoil. Figure 4.7 compares the extent of airfoil displacement to shear layer thickness at each of these locations for the maximum angle of attack of 20°. It can

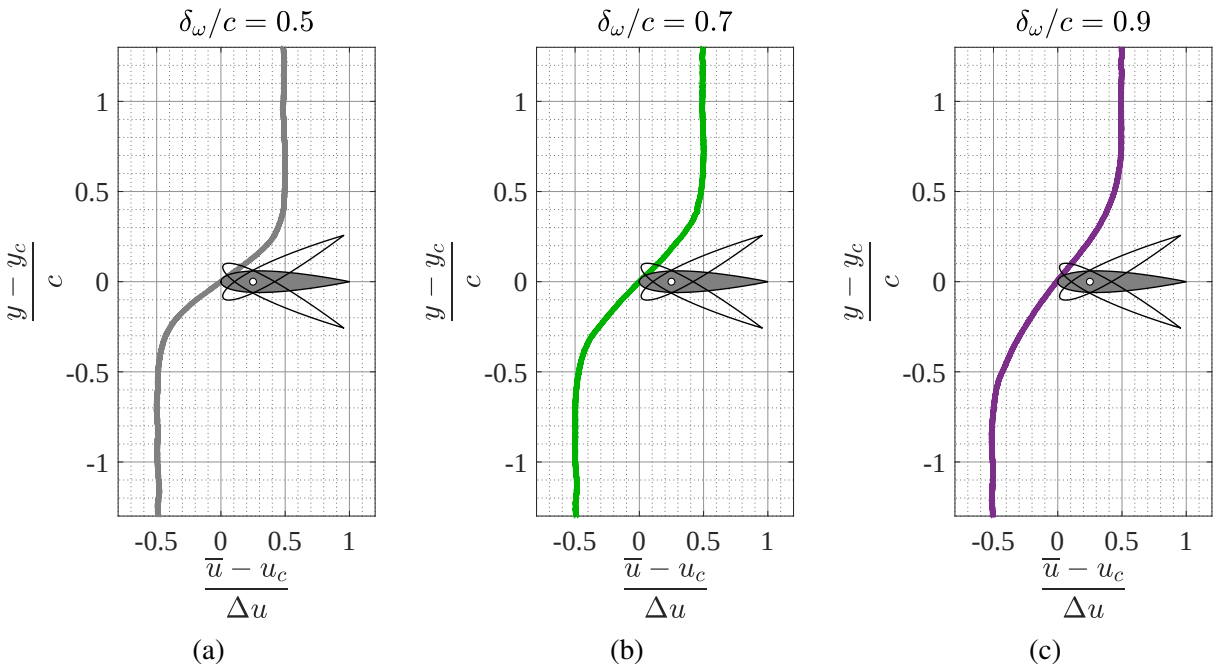

Figure 4.7: Extent of airfoil angular displacement (±20°) compared to the two-stream shear layer thickness at each measurement location.

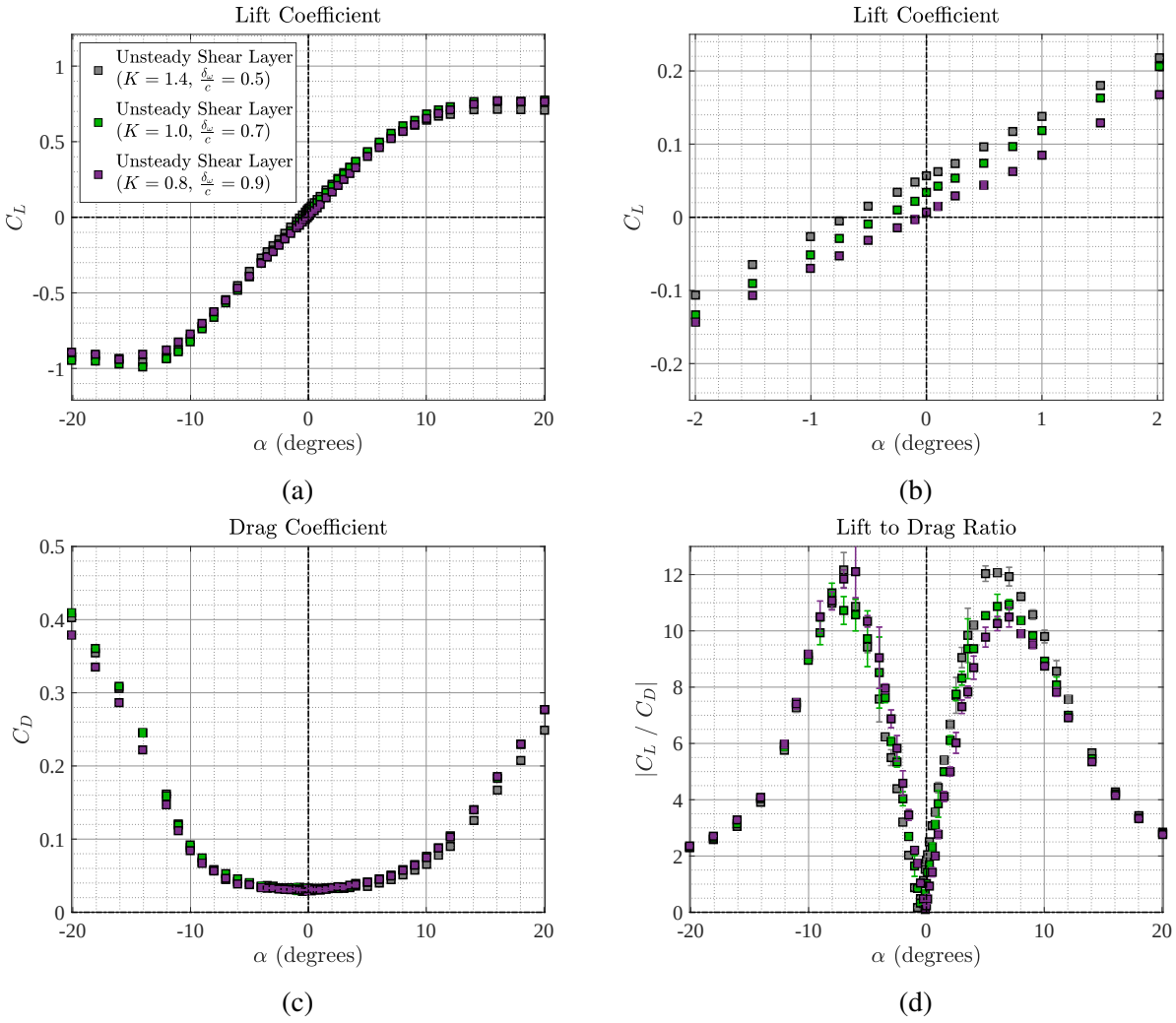

Figure 4.8: Comparison of aerodynamic force coefficients measured on a stationary airfoil placed in unsteady shear layer at different downstream locations: **(a)** mean lift coefficient, C_L, **(b)** zoomed up view of mean lift coefficient, C_L, **(c)** mean drag coefficient, C_D, **(d)** ratio of mean lift to mean drag, $\left|\frac{C_L}{C_D}\right|$.

be seen that the displacement of the airfoil trailing edge becomes comparable to the shear layer thickness at the largest angle of attack, especially for the thinnest shear layer with $\frac{\delta_\omega}{c} = 0.5$.

The aerodynamic force measurement results for different downstream locations in unsteady shear layer are presented in Figure 4.8. The main observation form the lift coefficient curves is that the overall behavior of the lift coefficient is very similar for all the downstream locations (Figure 4.8a). The only difference is that the magnitude of the positive lift at zero angle of attack decreases with distance downstream (Figure 4.8b). According to Figure 4.8c, the changes in shear rate (and

shear layer thickness) do not seem to noticeably affect the behavior of the drag coefficient. Figure 4.8d indicates that while all the unsteady shear layers display a mostly symmetric pattern in lift to drag ratio (especially compared to that of the steady shear layer), going further downstream slightly increases the weak asymmetry of the curve.

4.2 Aerodynamic Forces on an Oscillating Airfoil

Corresponding to the measurements described earlier, aerodynamic forces are measured on a purely pitching NACA0012 airfoil placed at the center of both steady and unsteady shear layers. Similarly, the measurements are carried out on the airfoil pitching in a uniform approach flow as well to provide a reference for comparison with steady and unsteady shear layer results. In each flow the airfoil is set to be purely pitching around its quarter chord point with oscillation amplitudes of 2° and 4° and reduced frequencies, k, ranging from 1 to 6. Table 4.1 lists the oscillation frequency details for all of the pitching airfoil force measurements performed in this work. For brevity, only the results from $\alpha_0 = 2^\circ$ oscillations are shown here and the results for $\alpha_0 = 4^\circ$ are provided in Appendix C.

The extent of the trailing edge displacement during pitching of the airfoil is compared to the thickness of the shear layer in Figure 4.9, where it is evident that the displacement of the airfoil is well within the central region of the shear layer.

Since in most studies on oscillating airfoils the interest is in the possible thrust force generated by the airfoil motion and to be consistent with previous works, the streamwise component of oscillating aerodynamic forces measured in this work is presented in the form of thrust coefficient, $C_T = -C_D$.

$k = \frac{\pi f c}{u_c}$	$k = 1$	$k = 2$	$k = 3$	$k = 4$	$k = 5$	$k = 6$
$\alpha_0 = 2^\circ$	$f = 0.26$ Hz	$f = 0.53$ Hz	$f = 0.79$ Hz	$f = 1.06$ Hz	$f = 1.32$ Hz	$f = 1.59$ Hz
$\alpha_0 = 4^\circ$	$f = 0.26$ Hz	$f = 0.53$ Hz	$f = 0.79$ Hz			

Table 4.1: List of unsteady force measurement cases.

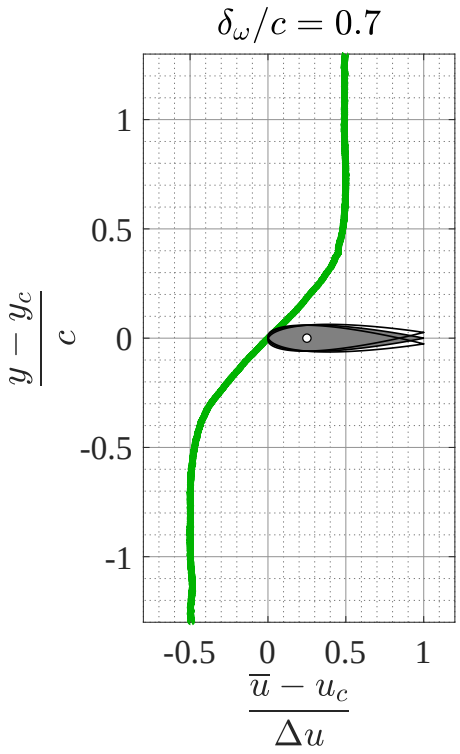

Figure 4.9: Extent of pitching airfoil angular displacement (±2°) compared to the shear layer thickness.

Aerodynamic force measurement results for the pitching airfoils are explored through the behavior of mean lift and thrust coefficients as well as their fluctuations as a function of reduced frequency for a single oscillation amplitude. Such results are depicted in Figure 4.10 for the cases with oscillation amplitude of 2°, where symbols depict the average value of 4 independent measurement repetitions for each combination of flow and oscillation frequency. The error bars for mean values are based on the propagation of sensor drift during each measurement, while the uncertainty in fluctuations is shown as the standard deviation of the fluctuation magnitudes between the 4 repetitions.

The first noticeable observation from the plot of mean lift coefficient versus airfoil oscillation reduced frequency (Figure 4.10a) is that for the uniform flow cases, the mean lift stays very close to zero (within experimental errors) for all reduced frequencies. This is the expected result for a symmetric airfoil oscillating symmetrically around zero angle of attack in a uniform flow, and reaffirms the accuracy of mean lift measurements. In the case of steady shear layer, the mean

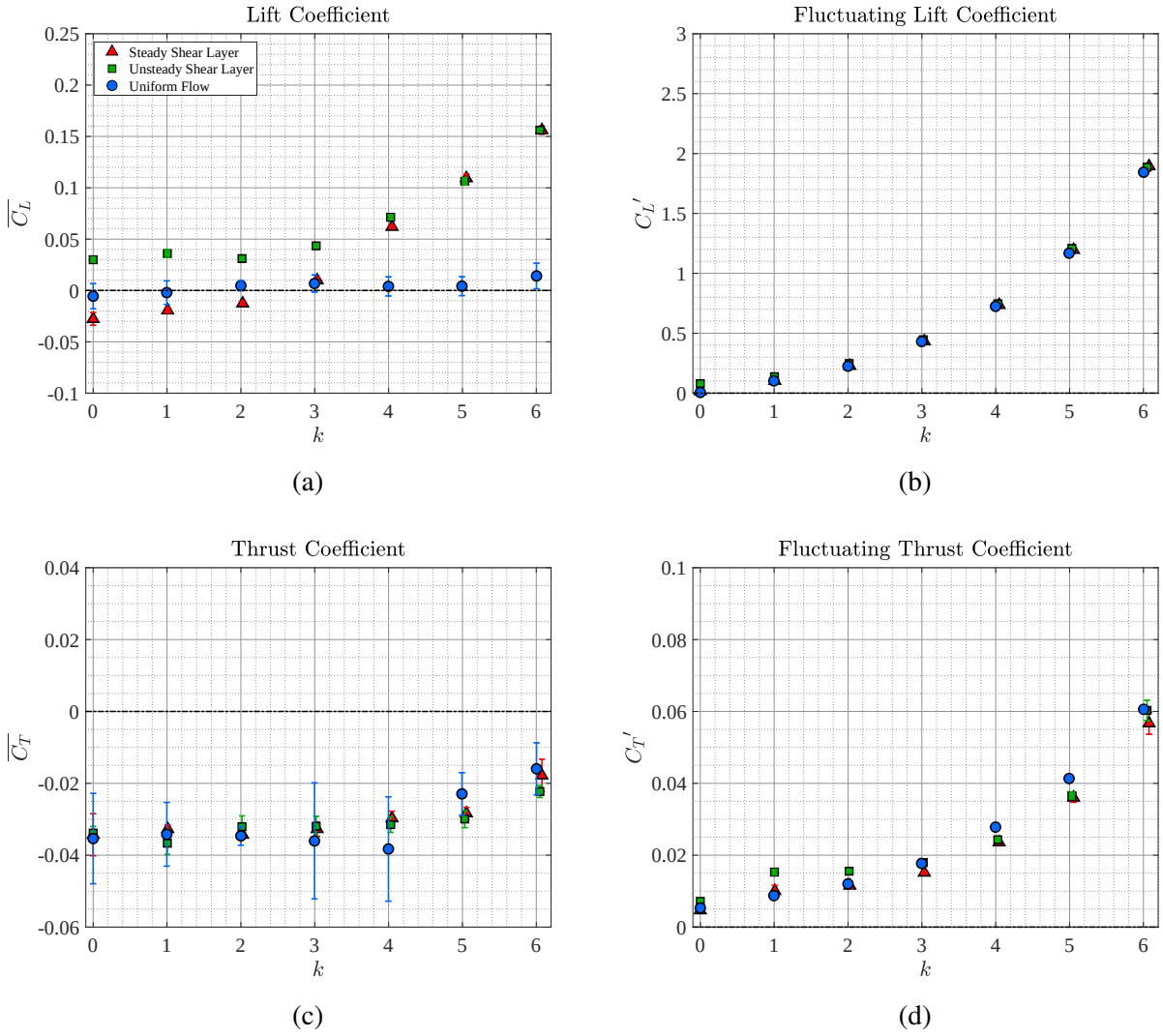

Figure 4.10: Comparison of aerodynamic force coefficients measured on a pitching airfoil placed in uniform, steady shear and unsteady shear flows: **(a)** mean lift coefficient, $\overline{C_L}$, **(b)** lift coefficient fluctuations, $C_L{}'$, **(c)** mean thrust coefficient, $\overline{C_T}$, **(d)** thrust coefficient fluctuations, $C_T{}'$. The airfoil is pitching with zero mean angle of attack and an oscillation amplitude of 2° around its quarter chord point.

lift gradually decreases in magnitude from its initial state of negative lift until it transitions to positive lift around $k = 2.5$. After this point the magnitude of now positive mean lift increases with frequency. This pattern is consistent with the numerical and experimental observations of Hammer et al. (2019). For unsteady shear case, the mean lift remains relatively constant (around the value of static lift at zero angle of attack) for small reduced frequencies ($k \leq 2$) and gradually increases afterwards. The behavior of mean lift in unsteady shear layer becomes similar to that of steady

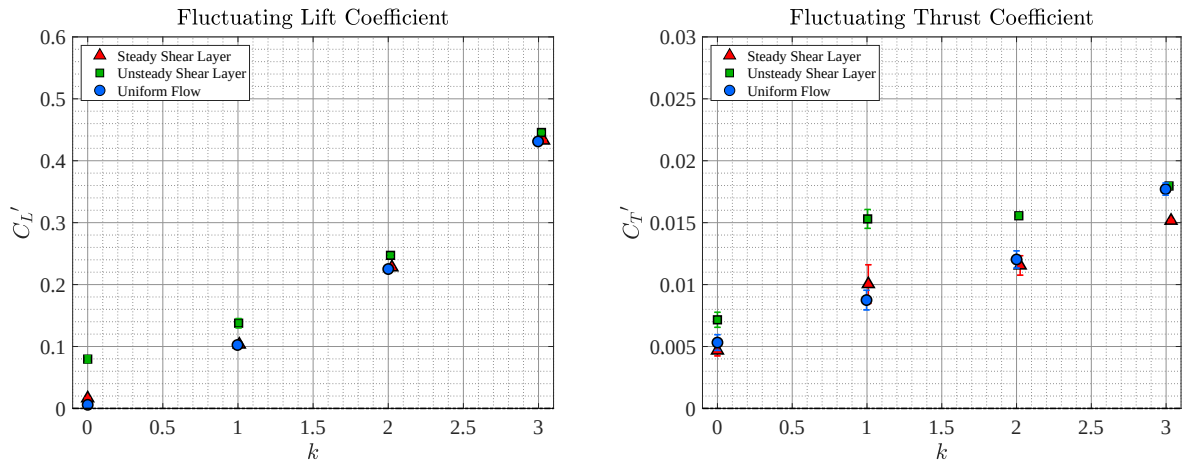

(a) (b)

Figure 4.11: Comparison of aerodynamic force fluctuations measured on a low frequency pitching airfoil placed in uniform, steady shear and unsteady shear flows: **(a)** lift coefficient fluctuations, $C_L{}'$, **(b)** thrust coefficient fluctuations, $C_T{}'$. The airfoil is pitching with zero mean angle of attack and an oscillation amplitude of 2° around its quarter chord point.

shear layer beyond ($k \geq 4$).

The comparison of lift coefficient fluctuations in different flows (Figure 4.10b) suggests that neither the presence of shear nor its unsteadiness seem to affect the fluctuations in the lift coefficient, similar to findings of Hammer et al. (2019). Mean and fluctuating thrust coefficients are found to be weakly affected by the change in shear flow parameters (Figures 4.10c and 4.10d), which is again in agreement with the conclusions of Hammer et al. (2019).

A closer look at both lift and thrust fluctuations at low oscillation frequencies emphasizes the slightly higher magnitude of fluctuations in unsteady shear layer compared to steady shear layer and uniform flow (Figure 4.11). This is consistent with the higher level of inherent fluctuations in the unsteady shear flow. As the oscillation frequency of the pitching airfoil increases, these flow induced fluctuations become negligible compared to the fluctuations generated by airfoil oscillation in measured forces.

These observations suggest that at low frequencies, the mean lift generated by unsteady shear layer is mostly governed by the unsteadiness of the flow, but as the frequency of oscillation increases the impact of airfoil oscillations becomes more dominant and at high enough frequencies,

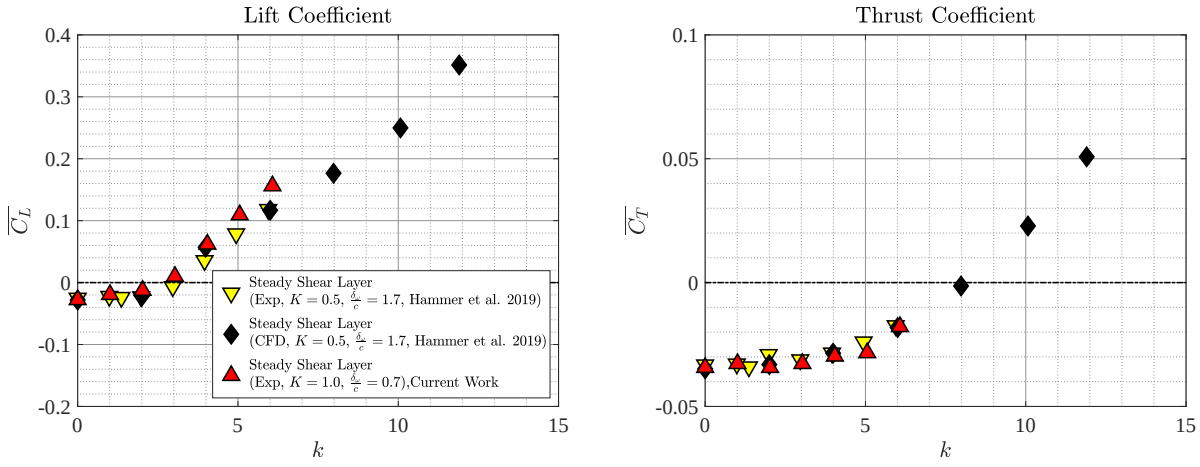

(a) (b)

Figure 4.12: Comparison of aerodynamic force coefficients measured on a pitching airfoil placed in steady shear with experimental and numerical results of Hammer et al. (2019): **(a)** mean lift coefficient, $\overline{C_L}$, **(b)** mean thrust coefficient, $\overline{C_T}$. The airfoil is pitching with zero mean angle of attack ($\alpha_m = 0^\circ$) and an oscillation amplitude of $\alpha_0 = 2^\circ$ around its quarter chord point.

the airfoil oscillation alone will dictate the aerodynamic performance. This hypothesis will be further investigated later through phase ordering the force measurement results.

Figure 4.12 compares the mean aerodynamic force coefficients measured in the steady shear layer of the current work with numerical simulations and experimental results of Hammer et al. (2019) for a similar NACA0012 airfoil pitching with the same parameters. As mentioned previously, their steady shear flow results are not from a mean velocity profile matching the one in this work, but from a three segmented linear velocity profile. With this in mind, both the mean lift and thrust coefficients show a qualitative agreement with their results.

The results from force measurements on an airfoil pitching with an oscillation amplitude of $\alpha_0 = 4^\circ$ (presented in Appendix C) show a similar trend. While the mean lift of the steady and unsteady shear layers initially have opposite signs, they seem to produce similar values of lift at reduced frequencies of $k > 2.5$.

4.2.1 Effect of Upstream Unsteady Shear Flow Profile on Aerodynamic Forces on an Oscillating Airfoil

The unsteady aerodynamic forces are also measured with the pitching airfoil positioned at the two other downstream locations in the two-stream shear layer (shown in Figure 4.6) mentioned in the stationary airfoil section. Figure 4.13 illustrates the sweep of the airfoil trailing edge during the oscillating motion in comparison with the width of the shear layer at each of these locations. A maximum of ~20% of the shear layer thickness is covered for the worst case of 4° oscillations in the most upstream location with $\frac{\delta_\omega}{c} = 0.5$ (see Appendix C).

The mean lift results of these measurements for the oscillation amplitude of $\alpha_0 = 2°$ are compared with the reference unsteady shear layer case in Figure 4.14. The mean lift coefficient curves exhibit a similar behavior of relatively constant magnitude of lift at low frequency oscillations and then gradually increasing after a reduced frequency of $k = 2.5$. The main difference between the different downstream positions seems to be a fairly constant shift in the curve based on their lift magnitude at zero angle of attack. This would suggest that to the first order, the lift performance

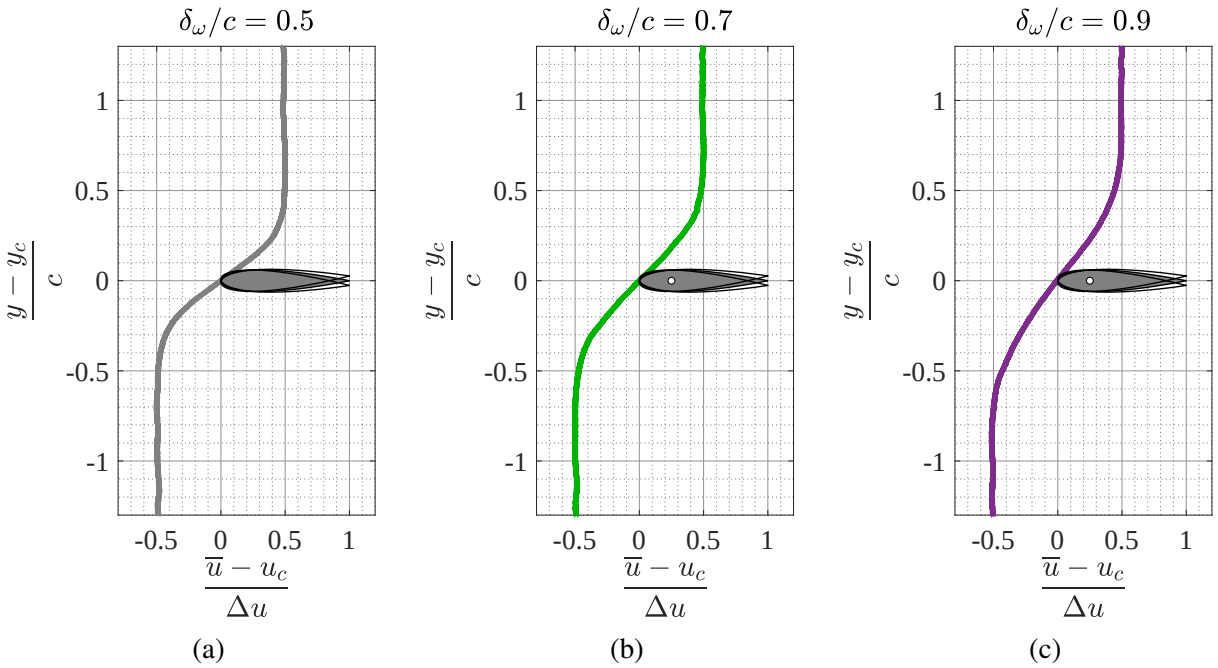

Figure 4.13: Extent of airfoil angular displacement (±2°) compared to the two-stream shear layer thickness at each measurement location.

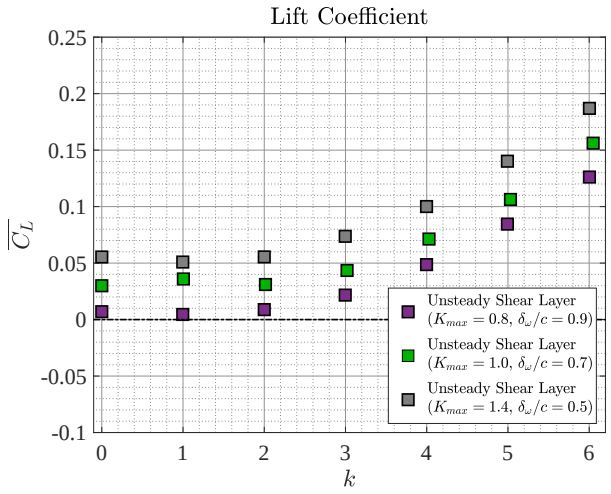

Figure 4.14: Comparison of aerodynamic force coefficients measured on a pitching airfoil placed in two-stream shear layer at different downstream locations: **(a)** mean lift coefficient, $\overline{C_L}$, **(b)** mean thrust coefficient, $\overline{C_T}$. The airfoil is pitching with zero mean angle of attack ($\alpha_m = 0^\circ$) and an oscillation amplitude of $\alpha_0 = 2^\circ$ around its quarter chord point.

of the airfoil in the unsteady shear seems closely related to the shear rate and the initial lift of the stationary airfoil.

4.3 Phase Ordered Aerodynamic Forces on Oscillating Airfoil

Because of the oscillatory nature of forces in this problem and high repeatability of the measurements, phase ordering/phase averaging the measured force time series can provide more insight into the dynamics of the forces. The mean force results presented in the previous section have shown two regions where the behavior of the unsteady shear layer was different from that of steady shear layer; at low oscillation frequencies the unsteady shear layer produced a positive lift as opposed to the negative lift observed in the steady shear layer, whereas at higher frequencies the two shear layers behaved closer to each other with both generating positive lift with similar magnitudes. These two regions are highlighted in Figure 4.15. To further investigate the difference in aerodynamic performance between these two regions, two sample frequencies ($k = 2$ and 5, each in one region) are selected to compare the phase ordered/averaged behavior of the measured forces.

Figures 4.16, 4.17 and 4.18 show the phase ordered and phase averaged lift and thrust coefficients for uniform flow, steady shear layer and unsteady shear layer respectively, with the airfoil pitching

with a reduced frequency of $k = 2$ and oscillation amplitude of $\alpha_0 = 2^\circ$. Each of these plots are from a single force measurement experiment data sorted into 128 phase bins based on the airfoil angular position (with a minimum of $\sim$ 1300 points per bin for cases with the largest oscillation period). In these plots, the blue lines represent the phase ordered data, while the red lines portray the phase averaged values and the black lines highlight the standard deviation of the data grouped in each phase bin. Figures 4.19, 4.20 and 4.21 depict the same results for the reduced frequency of $k = 5$.

Through the first glance at the phase ordered lift coefficient results for $k = 2$ cases, it becomes obvious that the cycle to cycle variation is much larger in the unsteady shear layer compared to the steady shear and uniform flows. While the same observation is true for the larger reduced frequency of $k = 5$, the ratio of cycle to cycle variation to the actual force oscillations is smaller in this case. This difference can be demonstrated better by comparing the average value of all the phase bin variations for each flow at each reduced frequency $\left(\overline{\langle C_L \rangle'}\right)$. Figure 4.22 displays these values both straightaway and normalized by the overall lift coefficient fluctuations $\left(\dfrac{\overline{\langle C_L \rangle'}}{C_L'}\right)$ in that case. It is observed that although the average phase bin variations are significantly higher for unsteady shear layer across all reduced frequencies, its normalized magnitude becomes much smaller moving towards the higher frequencies. For example, at $k = 1$ the phase bin variation

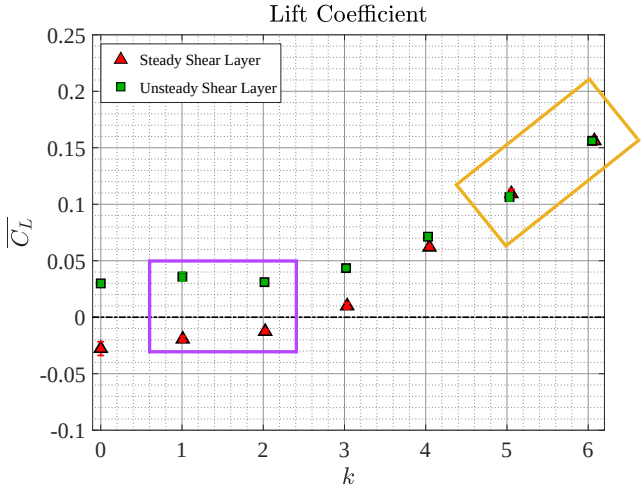

Figure 4.15: Highlighted comparison of mean lift curve between unsteady versus steady shear layer.

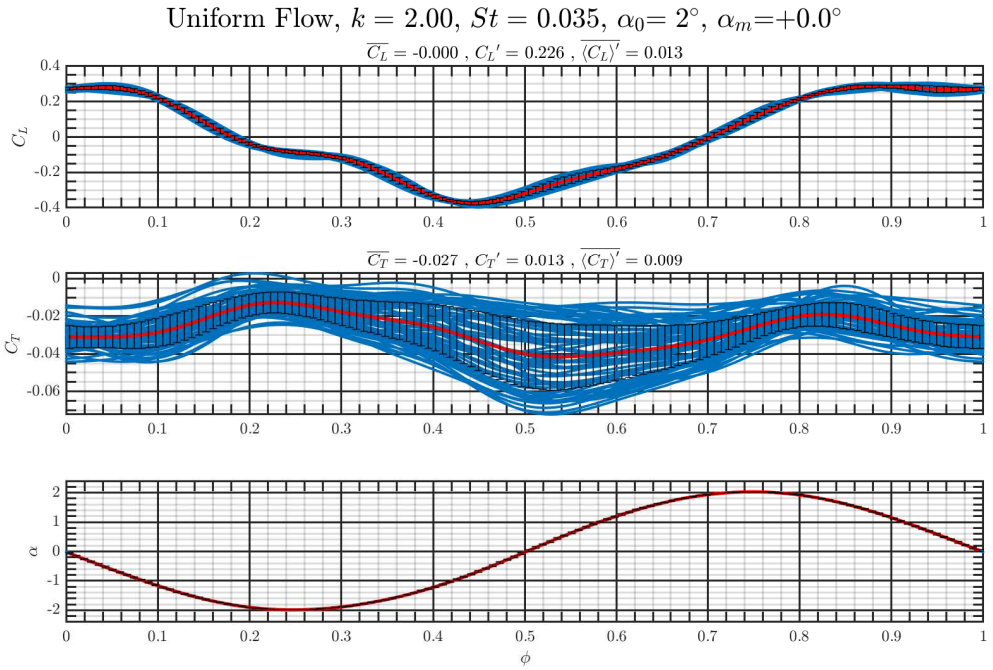

Figure 4.16: Sample of phase ordered force measurements performed in uniform flow for a pitching airfoil with oscillation amplitude of $\alpha_0 = 2°$ and reduced frequency of $k = 2$. Blue lines represent the phase ordered data, red lines portray the phase averaged values with the black lines highlighting the standard deviation of the data in each phase bin.

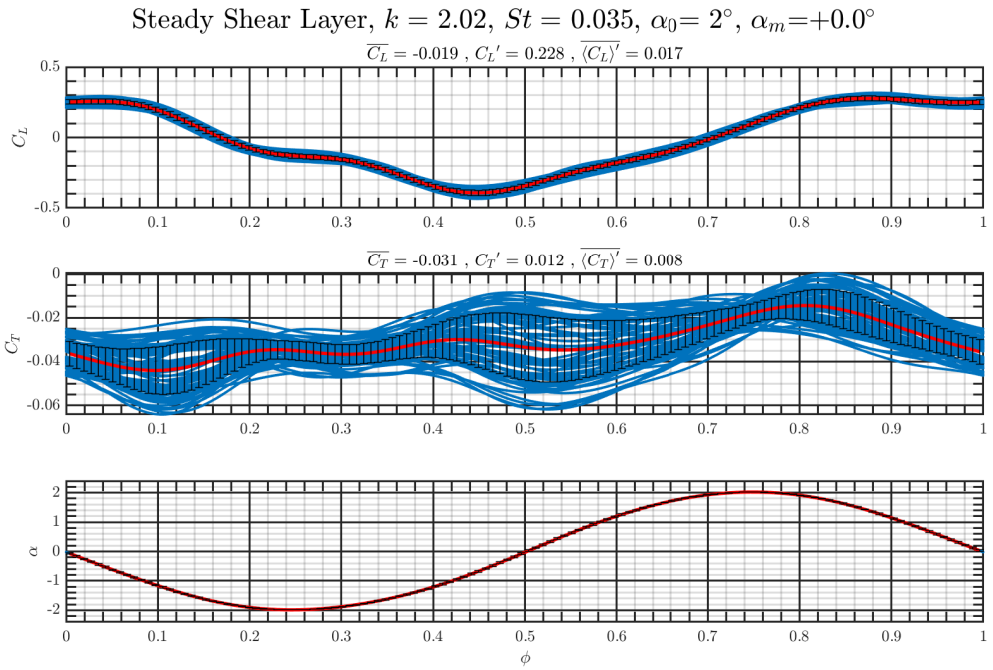

Figure 4.17: Sample of phase ordered force measurements performed in steady shear flow for a pitching airfoil with oscillation amplitude of $\alpha_0 = 2°$ and reduced frequency of $k = 2$. Blue lines represent the phase ordered data, red lines portray the phase averaged values with the black lines highlighting the standard deviation of the data in each phase bin.

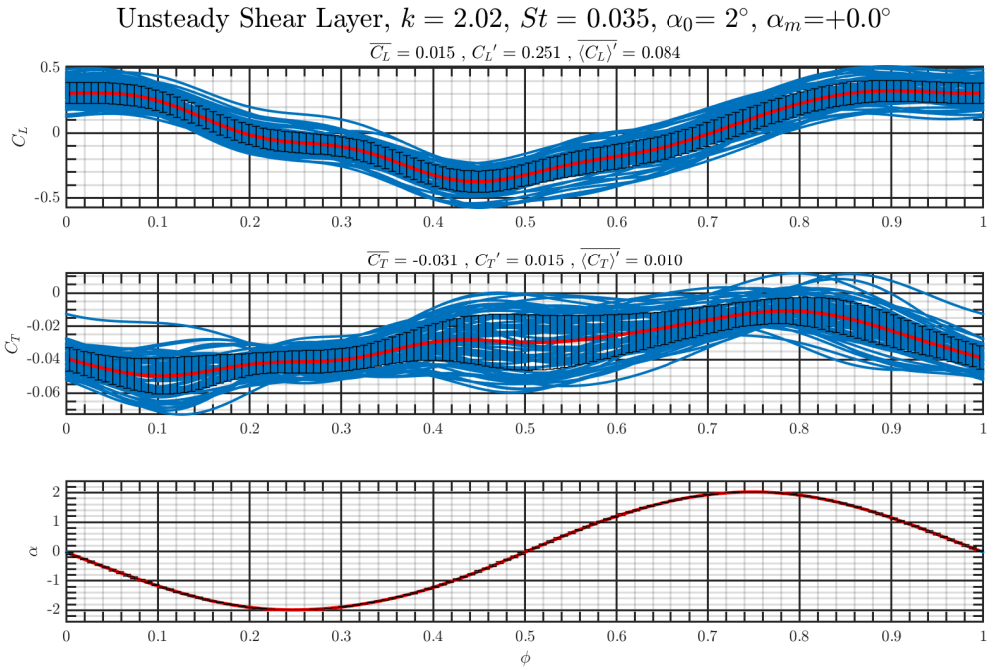

Figure 4.18: Sample of phase ordered force measurements performed in unsteady shear flow for a pitching airfoil with oscillation amplitude of $\alpha_0 = 2°$ and reduced frequency of $k = 2$. Blue lines represent the phase ordered data, red lines portray the phase averaged values with the black lines highlighting the standard deviation of the data in each phase bin.

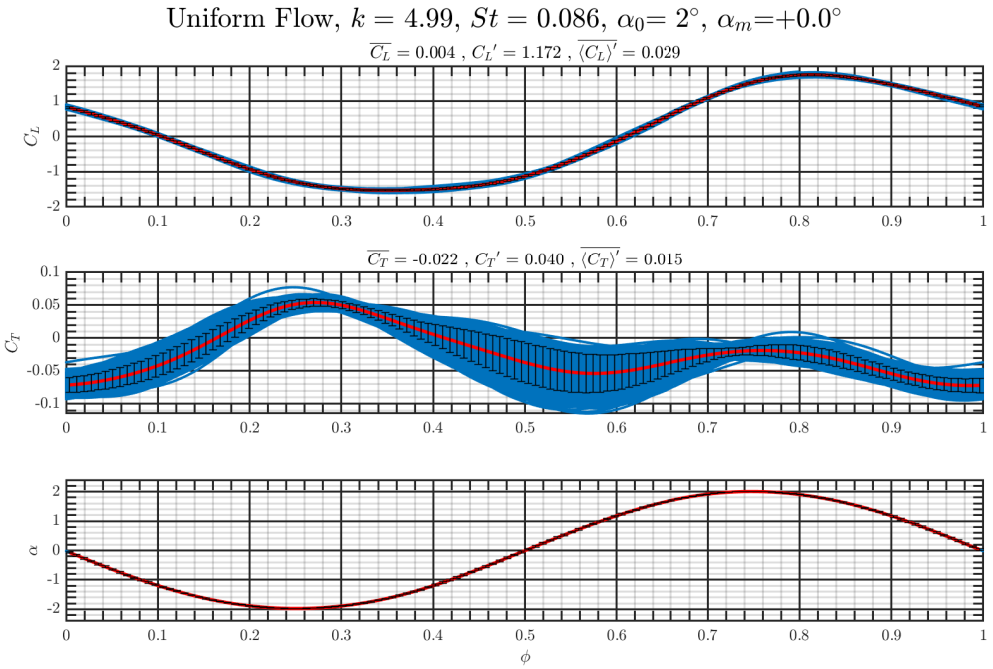

Figure 4.19: Sample of phase ordered force measurements performed in uniform flow for a pitching airfoil with oscillation amplitude of $\alpha_0 = 2°$ and reduced frequency of $k = 5$. Blue lines represent the phase ordered data, red lines portray the phase averaged values with the black lines highlighting the standard deviation of the data in each phase bin.

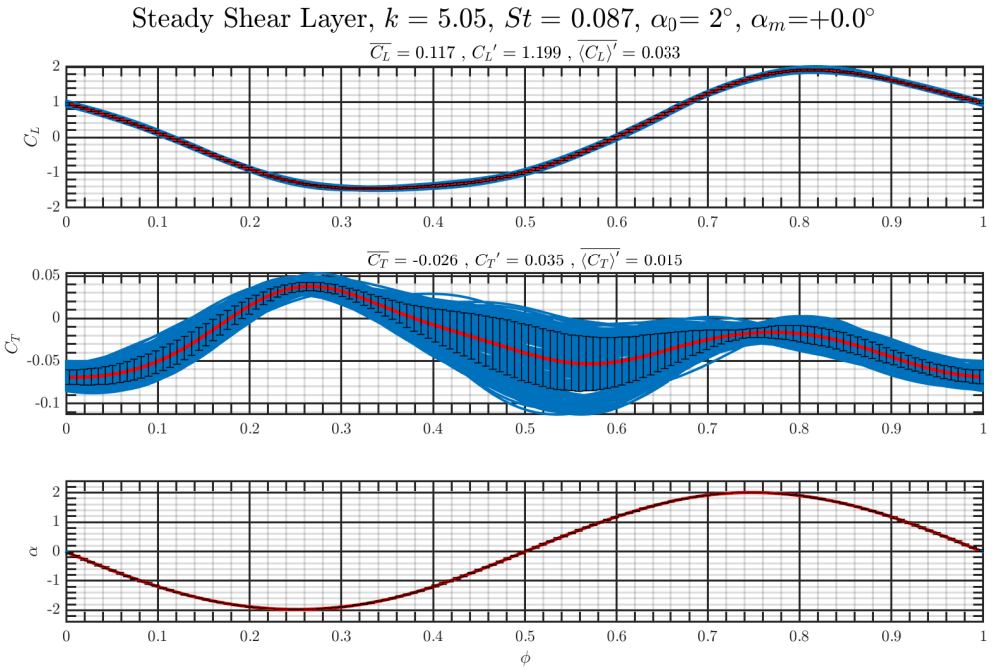

Figure 4.20: Sample of phase ordered force measurements performed in steady shear flow for a pitching airfoil with oscillation amplitude of $\alpha_0 = 2°$ and reduced frequency of $k = 5$. Blue lines represent the phase ordered data, red lines portray the phase averaged values with the black lines highlighting the standard deviation of the data in each phase bin.

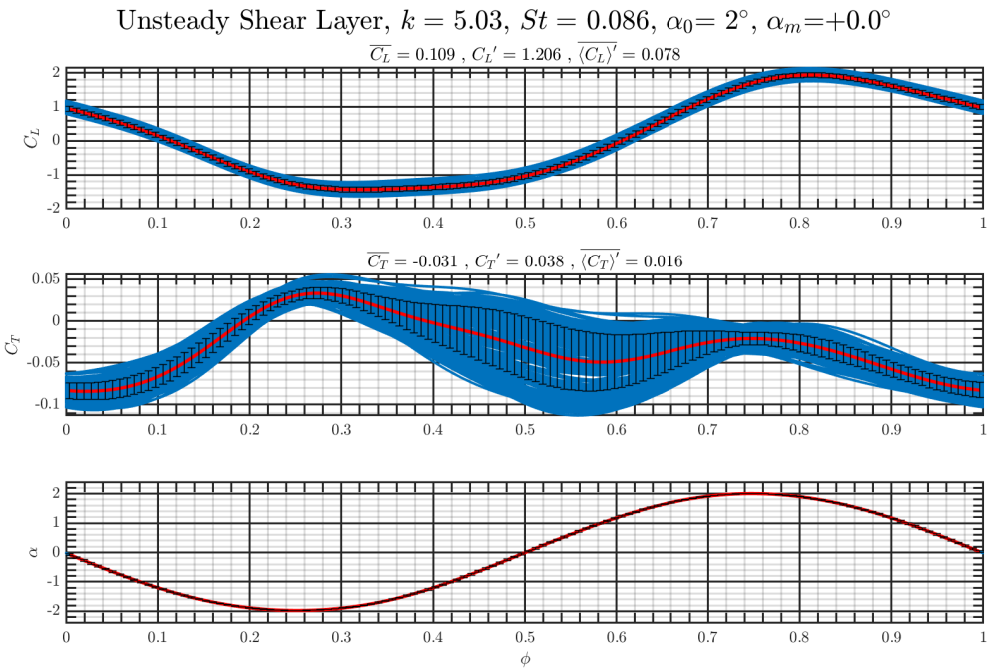

Figure 4.21: Sample of phase ordered force measurements performed in unsteady shear flow for a pitching airfoil with oscillation amplitude of $\alpha_0 = 2°$ and reduced frequency of $k = 5$. Blue lines represent the phase ordered data, red lines portray the phase averaged values with the black lines highlighting the standard deviation of the data in each phase bin.

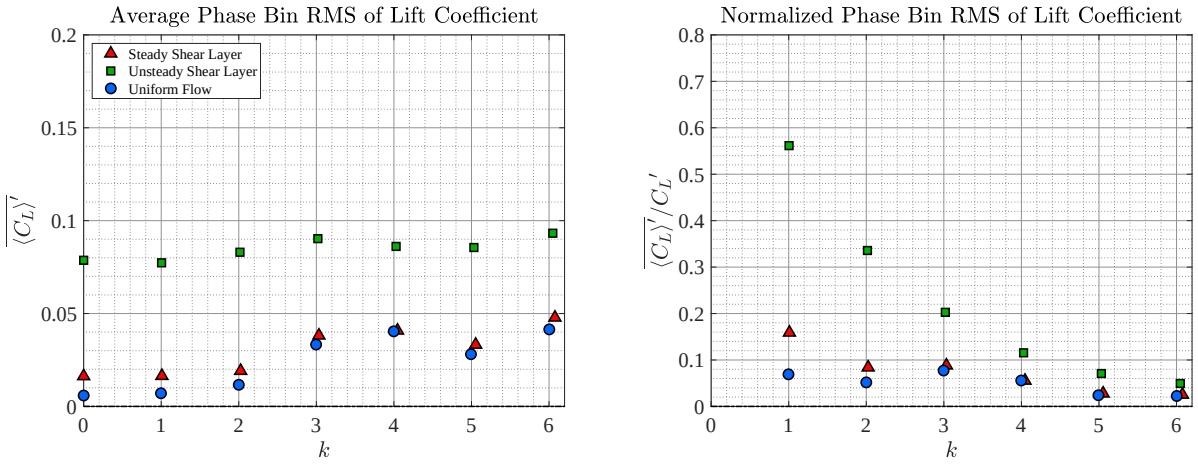

(a) (b)

Figure 4.22: Comparison of **(a)** raw and **(b)** normalized average phase bin standard deviation in lift for different upstream flow conditions as a function of reduced frequency.

in unsteady shear layer is ~56% of the overall fluctuations, however, at $k = 5$ this ratio drops to ~7%. This indicates that the contribution of the upstream flow unsteadiness to lift diminishes significantly at higher oscillation frequencies and the flow becomes dominated by the perturbations due to the airfoil oscillations. It is interesting to see that the same conclusion dos not apply to thrust coefficient fluctuations (see Figure 4.23), where it was previously observed it is only weakly affected by the the changes in approach flow conditions. Figure 4.23b suggests that a large portion

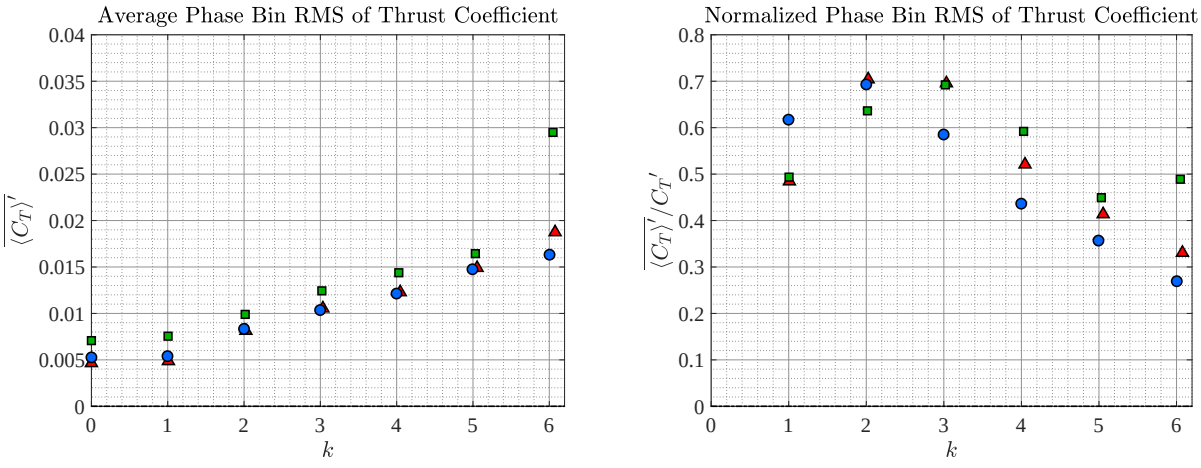

(a) (b)

Figure 4.23: Comparison of **(a)** raw and **(b)** normalized average phase bin standard deviation in thrust for different upstream flow conditions as a function of reduced frequency.

of thrust fluctuations are due to the contribution of cycle-to-cycle variation, even for the uniform flow and steady shear layer.

CHAPTER 5

VELOCIMETRY INSIDE AIRFOIL BOUNDARY LAYER

Comparison of the forces measured on the stationary airfoil positioned at the center of unsteady and steady shear layers showed significant differences, especially in the behavior of the lift curve. These observations lead to the hypothesis that the aerodynamic performance of the airfoil is affected by the unsteady shear layer through the influence of its higher level of fluctuations on the laminar separation on the surface of the airfoil.

To examine this hypothesis, streamwise component of the velocity is measured using 1c-MTV near the surface of a stationary airfoil placed in both steady and unsteady shear layers over a range of angles of attack. The results of these measurements are used to provide an overview of the behavior of the flow around the airfoil.

Since it was observed from the force measurements that the aerodynamic performance of the airfoil was asymmetric in the presence of approach shear flows, the objective here is to perform boundary layer resolved measurements on the suction side of the airfoil when it is placed at both positive and negative angles of attack. Furthermore, it is desired to carry out similar measurements on the pressure side of the airfoil at a couple of select angles of attack. However, as described earlier in the experimental methods chapter, optical access is limited to only one side of the airfoil due to physical constraints of the experimental setup. In normal configuration of the setup this will restrict the measurements to the suction side of the airfoil when it is placed at a positive angle in the approach flow with positive shear. To overcome this limitation, a portion of measurements are performed with the shear generation devices used in a reverse arrangement (i.e. shear layers generated with the placement of the high and low speed sides reversed in the water tunnel frame of reference). This strategy made it possible to gain optical access to the suction side of the airfoil when placed in negative angles of attack in the positive shear, as well as to the pressure side of the airfoil at positive angles of attack. The consistency of generated shear layers in reverse versus normal arrangement is confirmed by double checking the mean and fluctuating velocity profiles of

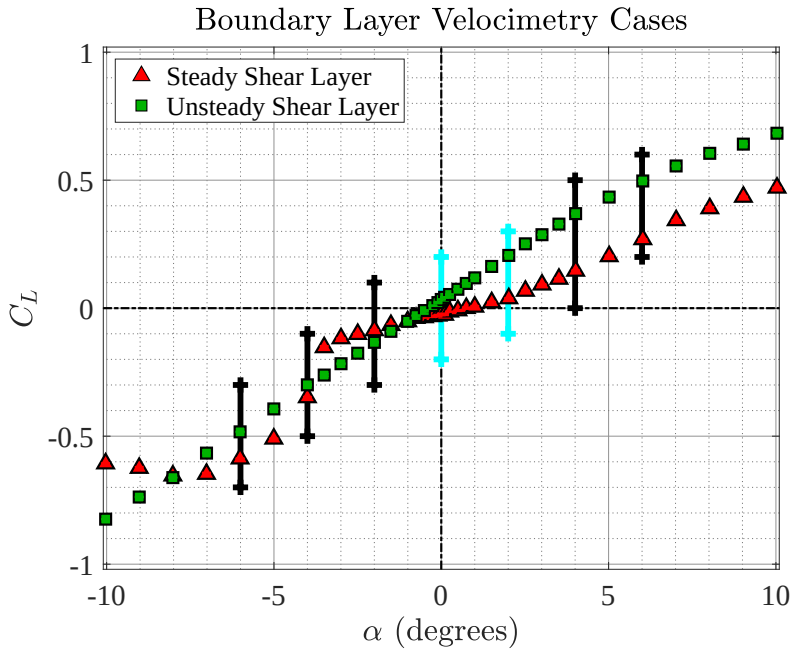

Figure 5.1: Schematic of airfoil angles of attack investigated through boundary layer measurements superposed on the lift coefficients measured for steady and unsteady shear flows. The cyan lines highlight the cases that both the suction and pressure sides of the airfoil have been considered, whereas for the cases shown with black lines only the suction side of the airfoil is evaluated.

each reverse shear against its original arrangement. Additionally, aerodynamic performance of the airfoil in each reverse shear flow was measured to be in agreement with that of the original shear layers. These results are not shown in this document for brevity.

The airfoil angles of attack that have been investigated in this chapter are illustrated in Figure 5.1 with vertical lines overlaid on the plot of corresponding lift coefficients measured at these angles of attack in steady and unsteady shear layers. The cyan lines highlight the cases that both the suction and pressure sides of the airfoil have been considered, whereas for the rest of the cases (shown with black lines) boundary layer velocimetry is only performed on the suction side of the airfoil.

Figures 5.2 presents the mean and fluctuating velocity contours measured around the airfoil at zero angle of attack in the steady shear layer. The color map used for generating the contour plots are designed to show a sharp change from dark blue to purple at a velocity of zero to further highlight the regions with reverse flow. The mean streamwise velocity values are normalized by the centerline velocity of the shear flow (U_c) while the shear layer velocity difference, ΔU, is used

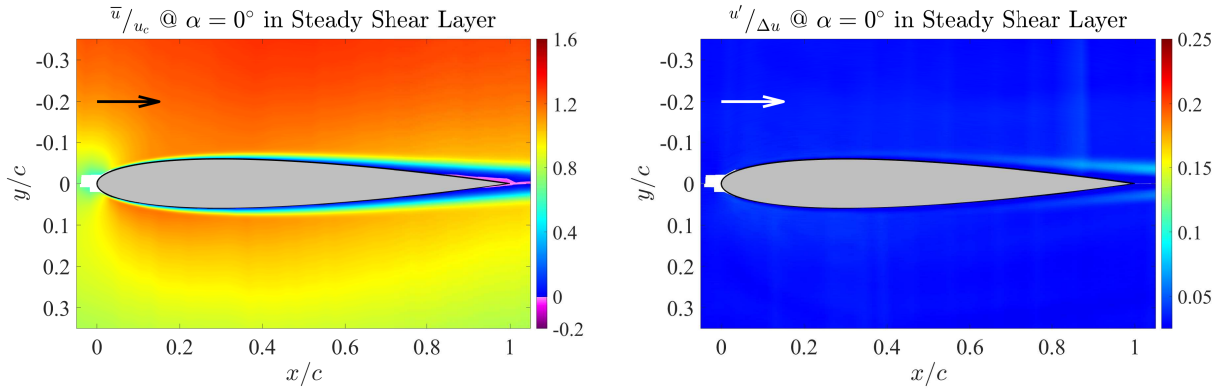

(a) (b)

Figure 5.2: Contour of **(a)** mean and **(b)** fluctuating streamwise velocities measured near the surface of the airfoil positioned at $\alpha = 0°$ at the center of the steady shear layer. The arrow indicates direction of the free-stream flow.

to normalize the velocity fluctuations. The white patches in the contours are regions that are either partially blocked by the airfoil or have been affected by the glow from the airfoil surface.

The mean velocity contour in Figure 5.2a indicates that in the presence of steady shear, the boundary layers separate asymmetrically on the upper and lower surfaces of the airfoil, with the separation of the boundary layer on the upper side of the airfoil (the surface towards the high speed side of the shear flow) first detected at a more upstream location. This finding is in agreement with numerical simulations of Hammer et al. (2018) for a similar NACA0012 airfoil in a uniform shear flow, where they found that this asymmetry increases with the shear rate. The asymmetry of the flow is also noticeable in the slightly larger boundary layer thickness on the upper side towards the trailing edge of the airfoil.

Figure 5.2b displays a lopsided distribution of velocity fluctuations in the presence of the steady shear flow, with a wider band of higher fluctuation magnitudes near the upper side of the airfoil. The vertical streak observed in the fluctuating velocity contour is an artifact of the experimental errors due to the lower signal to noise ratio of the tagged line combined with low levels of fluctuations in this flow.

Corresponding results for the airfoil set at zero angle of attack in the unsteady shear layer are shown in Figure 5.3. While the mean flow field further away from the airfoil may look similar

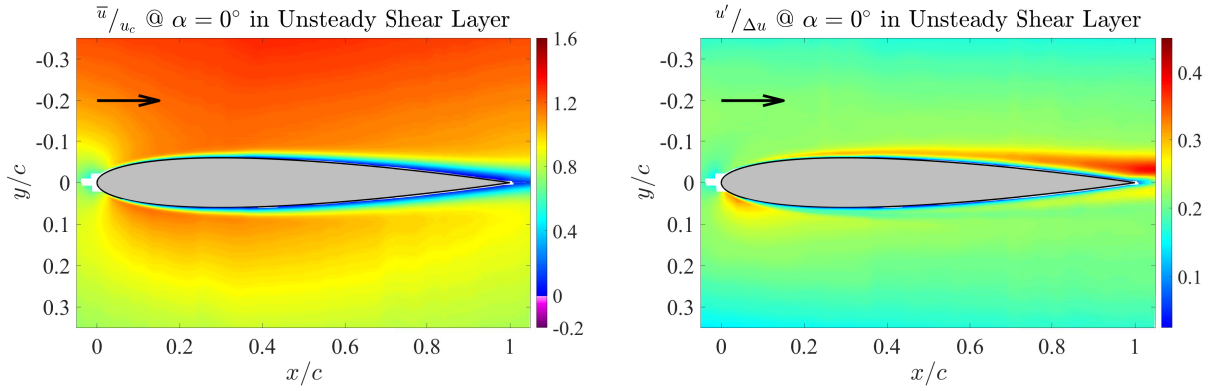

(a) (b)

Figure 5.3: Contour of **(a)** mean and **(b)** fluctuating streamwise velocities measured near the surface of the airfoil positioned at $\alpha = 0°$ at the center of the unsteady shear layer. The arrow indicates direction of the free-stream flow.

to that of the steady shear layer in the first glance, there is a crucial difference that no boundary layer separation or reverse flow is detected in the unsteady shear layer (Figure 5.3a). This means that either there is no separation happening in this flow or this region is thinner than the near wall spatial resolution of these experiments. The fluctuating velocity contour for the unsteady shear layer shown in Figure 5.3b exhibits an asymmetric distribution of velocity fluctuations similar to the steady shear layer case, however, it should be noted that the maximum level of fluctuation is roughly 6 times higher in the unsteady shear flow.

For non-zero angles of attack contours and to provide a better visual comparison of the flow field over different angles of attack, the fields of view are rotated such that the airfoil is portrayed at zero angle. However, the contour is still showing the actual streamwise component of the velocity, whose direction is indicated by the arrow shown on each plot. Different versions of these plots with the airfoil shown at its actual angle of attack are presented in Appendix E.

A comparison between the flow field around the airfoil set at 2° angle of attack in the steady shear layer (shown in Figure 5.4) and a similar geometry in the unsteady shear layer (shown in Figure 5.5) leads to a parallel observation. There is a clear reverse flow region on the suction side of the airfoil in the steady shear layer, but no sign of such region or separation is spotted in the unsteady shear flow. The general behavior of the velocity fluctuations in the two flows are mostly

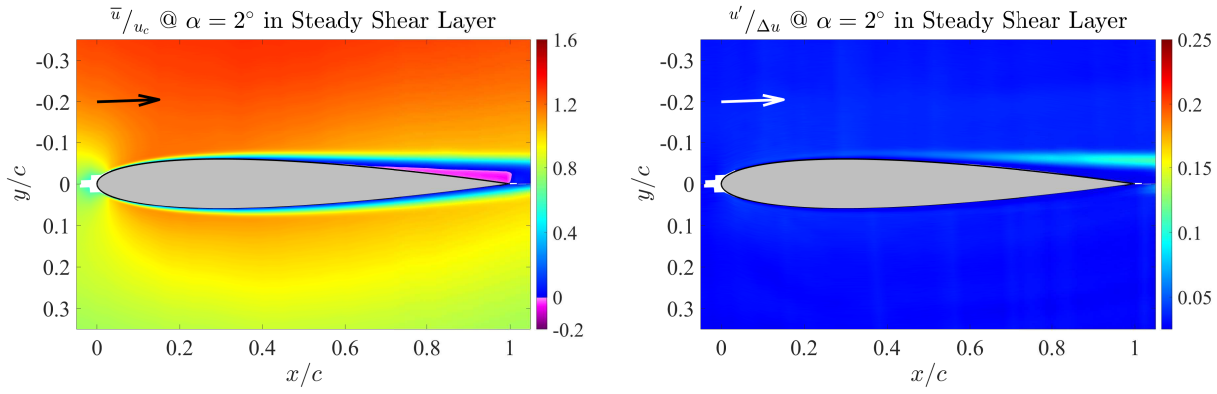

(a) (b)

Figure 5.4: Contour of **(a)** mean and **(b)** fluctuating streamwise velocities measured near the surface of the airfoil positioned at $\alpha = 2°$ in the steady shear layer. The field of view is rotated such that the airfoil is portrayed at zero angle but arrow indicates direction of the free-stream flow.

different in the amplitude of oscillations (with higher levels of fluctuations in the unsteady shear flow). Since no noticeable distinction is observed on the pressure side of the airfoil between the steady and unsteady shear flows and the flow fields are mostly different on the suction side, the rest of the measurements are only performed on the suction side of the airfoil.

Figure 5.6 depicts the flow field for a stationary airfoil placed at multiple positive angles of attack in the steady shear flow. Comparison of the mean velocity contours reveals that the separation

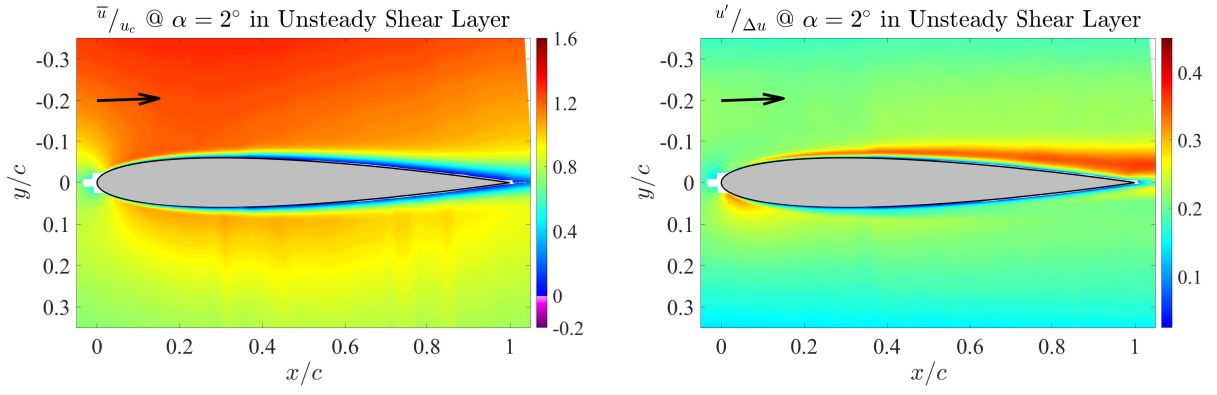

(a) (b)

Figure 5.5: Contour of **(a)** mean and **(b)** fluctuating streamwise velocities measured near the surface of the airfoil positioned at $\alpha = 2°$ in the unsteady shear layer. The field of view is rotated such that the airfoil is portrayed at zero angle but arrow indicates direction of the free-stream flow.

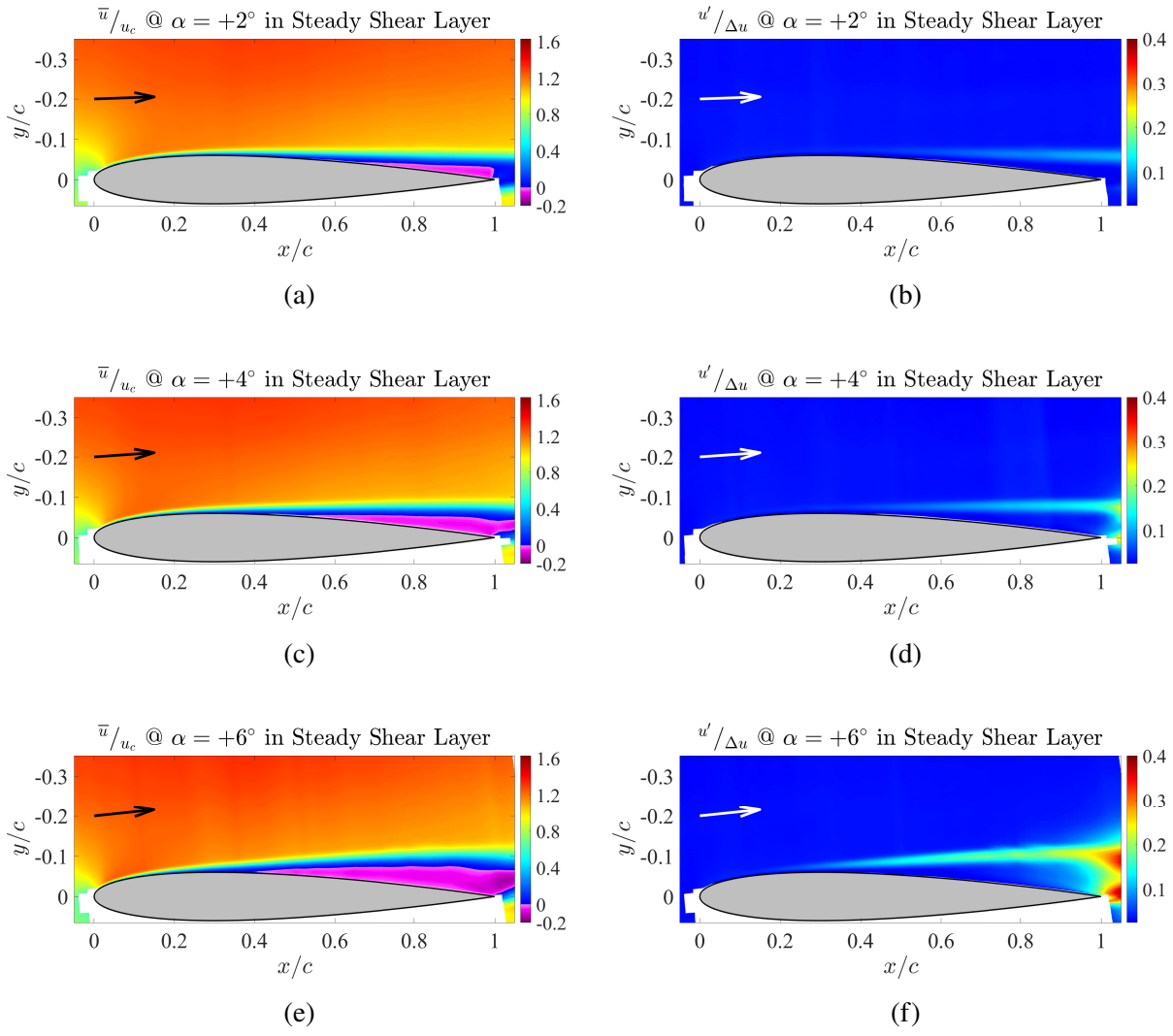

Figure 5.6: Comparison of mean (left), and fluctuating (right) streamwise velocity contours measured near the suction surface of the airfoil positioned at positive angles of attack in the center of the steady shear layer. The field of view is rotated such that the airfoil is portrayed at zero angle but arrow indicates direction of the free-stream flow.

point on the suction side of the airfoil moves upstream and the separated region grows in both width and height as the airfoil angle of attack increases. The main features of the velocity fluctuations remain the same, but the magnitude of fluctuations increases with airfoil angle of attack.

The effect of airfoil angle of attack on the flow field in the unsteady shear layer is found to be much subtler, as shown in Figure 5.7. There is still no explicit sign of separation in any of the geometries and the mean velocity contours are fairly close for the portrayed angles of attack, with

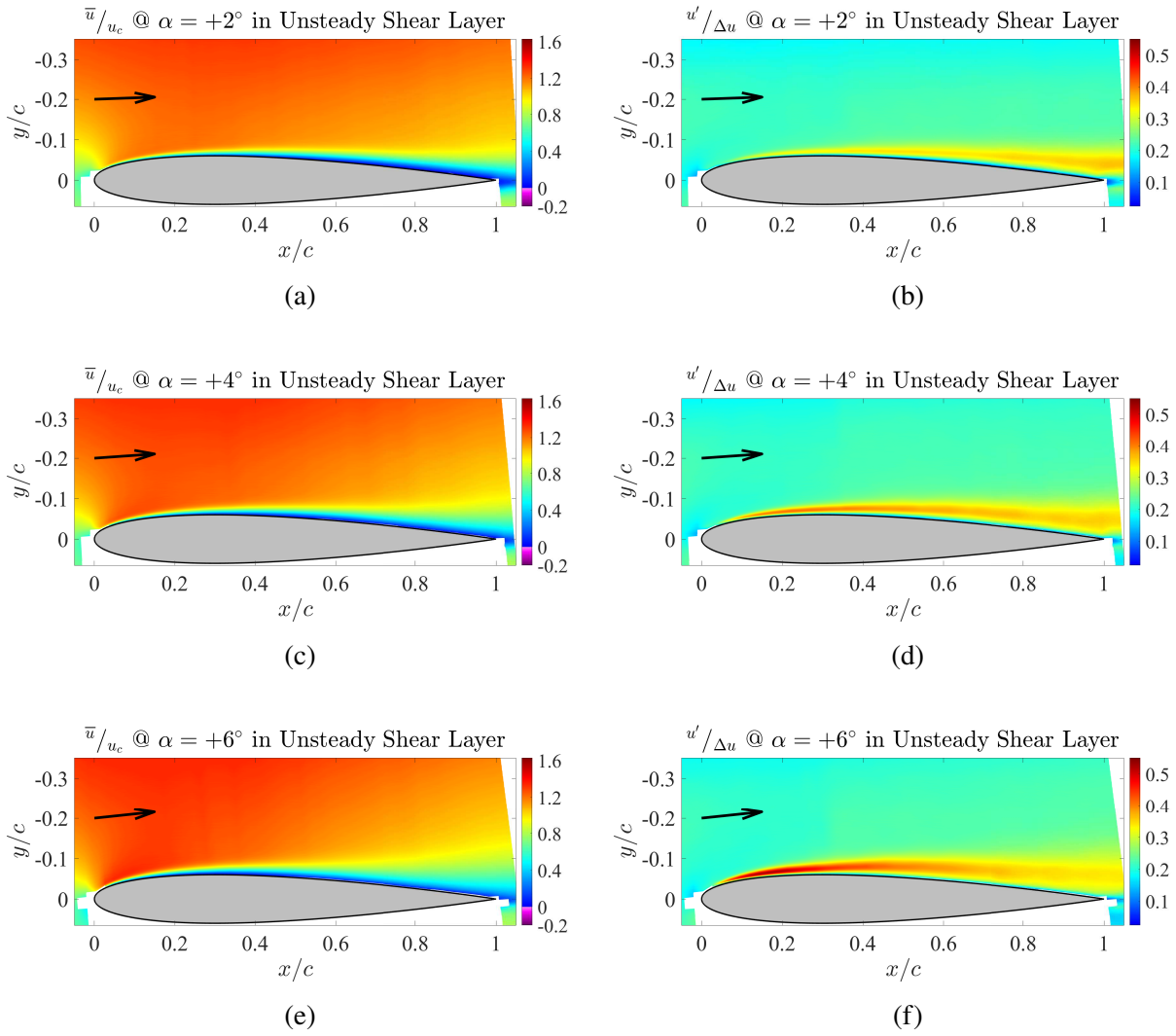

Figure 5.7: Comparison of mean (left), and fluctuating (right) streamwise velocity contours measured near the suction surface of the airfoil positioned at positive angles of attack in the center of the unsteady shear layer. The field of view is rotated such that the airfoil is portrayed at zero angle but arrow indicates direction of the free-stream flow.

an increase in the size of the sheared region above the trailing edge. The increase in angle of attack seems to shift the region of maximum fluctuations upstream towards the leading edge of the airfoil, in addition to raising the maximum level of fluctuations.

The flow field around the airfoil at negative angles of attack in the steady shear flow is presented in Figure 5.8. it is observed that at $\alpha = -2°$ and $-4°$ the flow behaves similar to the positive angles of attack with a open separation growing in height and the separation point moving upstream with

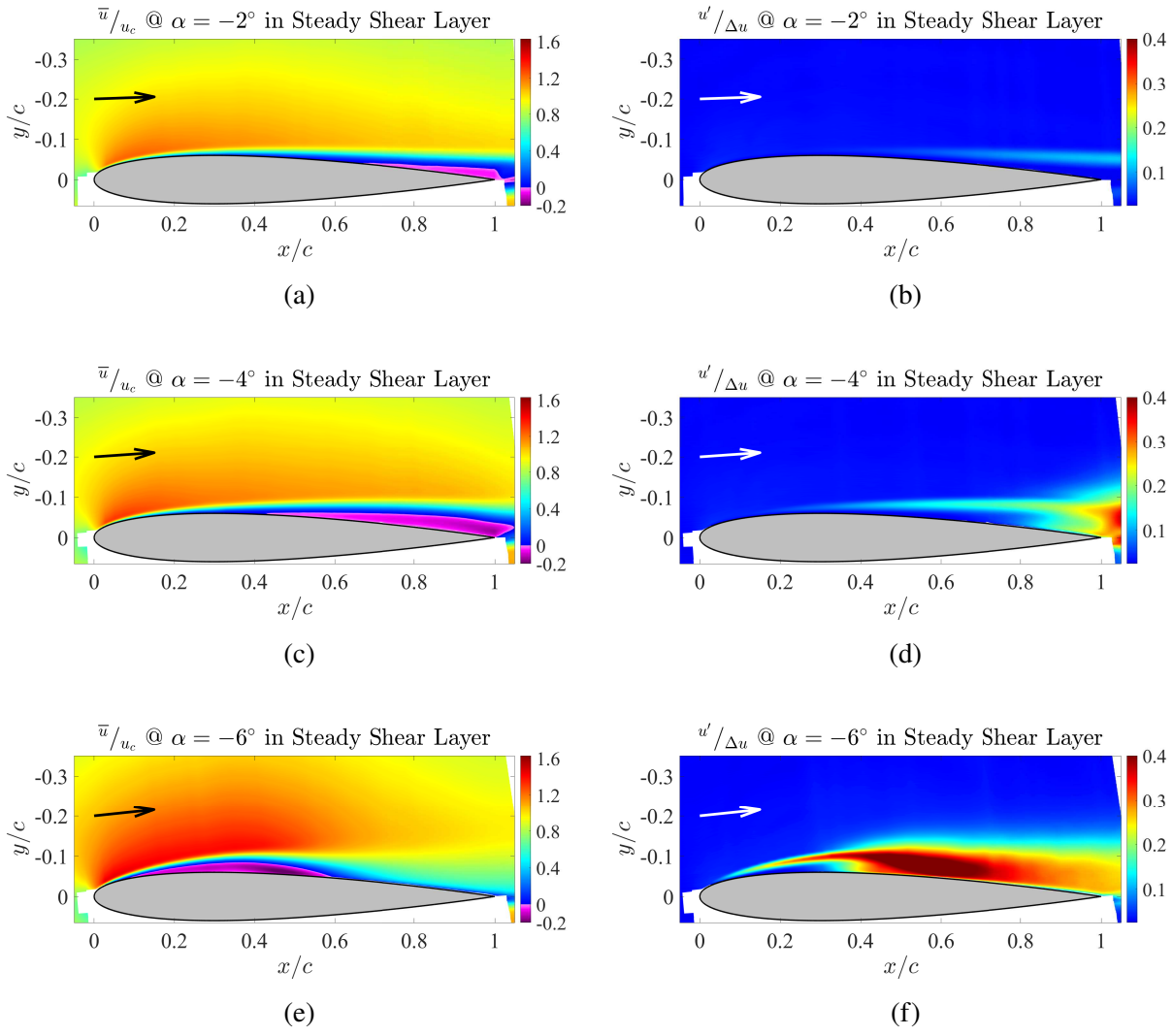

Figure 5.8: Comparison of mean (left), and fluctuating (right) streamwise velocity contours measured near the suction surface of the airfoil positioned at negative angles of attack in the center of the steady shear layer. The field of view is rotated such that the airfoil is portrayed at zero angle but arrow indicates direction of the free-stream flow.

an increase in angle of attack. At $\alpha = -6°$, however, the mean velocity contour indicates a closed laminar separation bubble. The signature of velocity fluctuations is also very different at this angle, where the initially thin region of high fluctuations shows an abrupt increase in height and quickly extends up to the airfoil surface.

Once more, no separation or reverse flow region is detected in the unsteady shear flow with the airfoil set at negative angles of attack, as shown in Figure 5.9. The primary feature of these flow

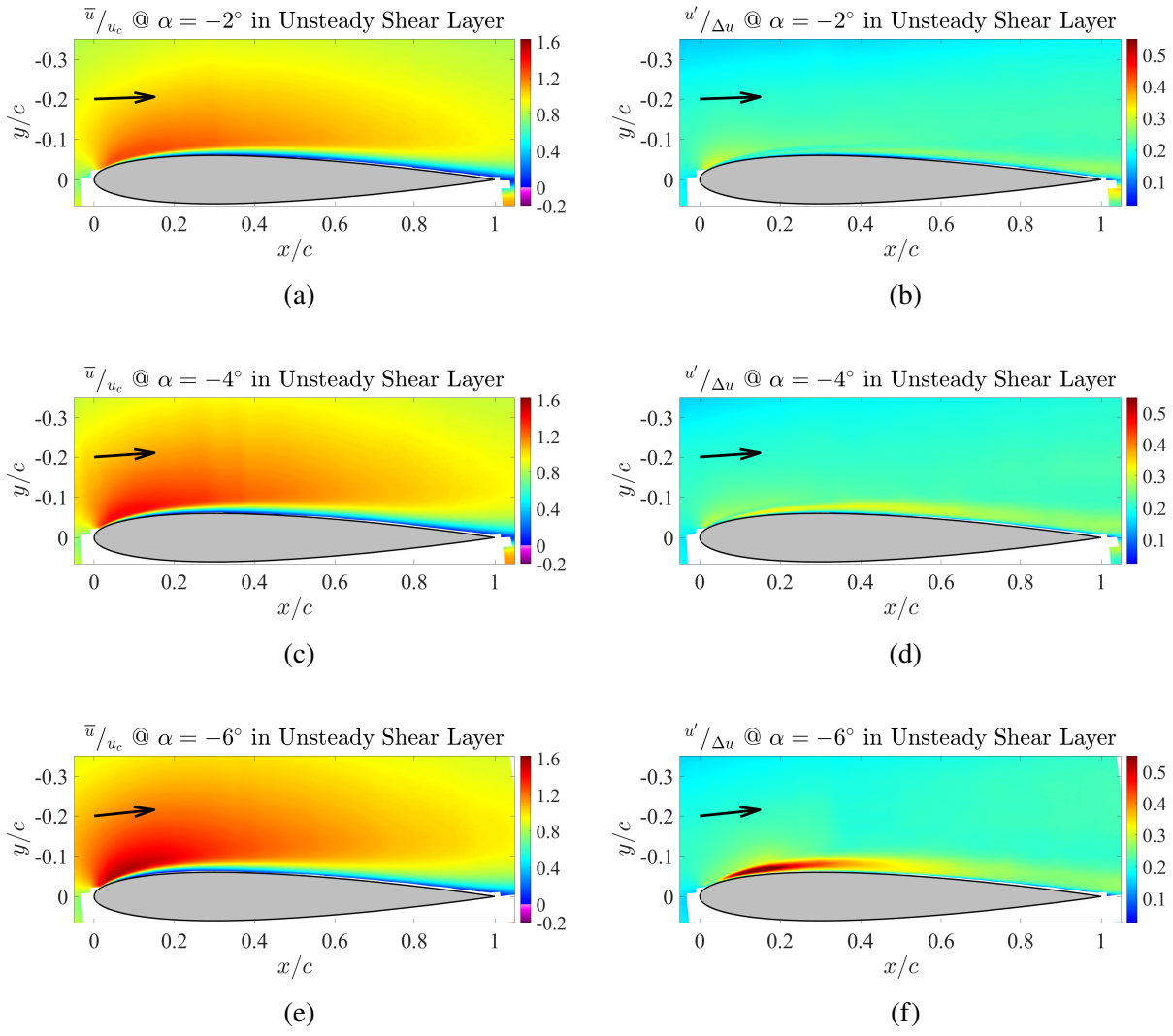

Figure 5.9: Comparison of mean (left), and fluctuating (right) streamwise velocity contours measured near the suction surface of the airfoil positioned at negative angles of attack in the center of the unsteady shear layer. The field of view is rotated such that the airfoil is portrayed at zero angle but arrow indicates direction of the free-stream flow.

fields is found to be an increase in both mean and fluctuating velocities near the leading edge of the airfoil, with the magnitudes rising with negative angle of attack.

Based on these observations, it was confirmed that unsteadiness of the shear flow affects the laminar separation on the surface of the airfoil to the extent that no separation region was observed within the near wall resolution of current measurements. This absence of laminar separation bubble can contribute to the differences observed in the lift characteristics of the NACA0012 airfoil at low

Reynolds number in the unsteady versus the steady shear layer.

CHAPTER 6

PITCHING AIRFOIL WAKE VISUALIZATION

Molecular tagging visualization is used for a qualitative exploration of the effect of the shear flow unsteadiness on the wake flow behind a symmetrically pitching airfoil. The resulting images from both shear flows (steady and unsteady shear layers with $K_{\max} = 1.0$ and $\frac{\delta_\omega}{c} = 0.7$) are also compared to those of a uniform approach flow to highlight the similarities and differences between all these cases. Figure 6.1 illustrates a sample of the initial tagging pattern (shown as violet) and a delayed state of these lines (shown as green) on a static airfoil in uniform flow. A few of the lines are set to strike the surface of the airfoil to provide a reference point for the position of the airfoil trailing edge. Delayed images are taken 30 ms after each laser pulse to give the tagged regions of fluid enough time to distort and underline the main flow features. To improve the visibility of flow structures through the deformed delayed lines, the initial tagged lines are not shown in the rest of the figures in this chapter.

Since these flow visualizations images are taken at such long delay times after the tagging laser

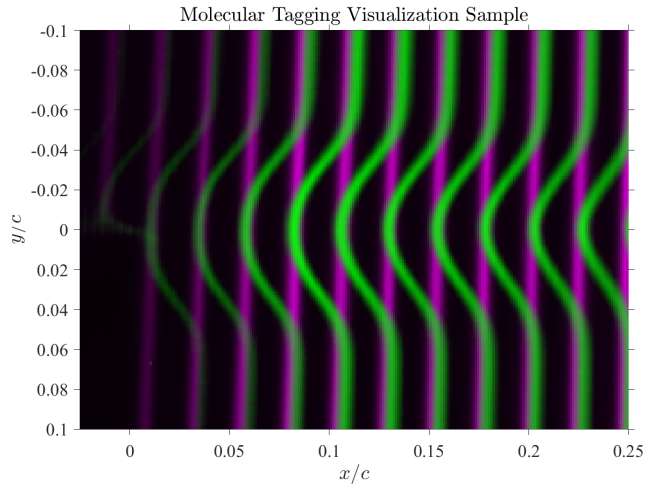

Figure 6.1: A sample pair of molecular tagging flow visualization tagged lines shown at initial (violet) and delayed (green) states. The initial image is taken $\sim 2\mu s$ after the laser pulse, while the delayed image is captured 30 ms after the laser pulse. The axes are normalized by the chord length of the airfoil with the trailing edge of the airfoil at zero angle of attack set as the origin.

pulse (30 ms compared to 3.5 ms nominal phosphorescence lifetime of the MTV solution), the results are phase ordered into 64 phase bins based on the frequency of airfoil oscillation and then phase averaged over each phase bin to reduce the noise and increase the quality of the images. A sample of these phase averaged images are presented in Figure 6.2 for the airfoil oscillating with oscillation amplitude of $\alpha_0 = 2^\circ$ and reduced frequency of $k = 6$ in uniform flow. The axes of these figures are normalized by the chord length of the airfoil with the trailing edge of the airfoil at zero angle of attack set as the origin. The location of the trailing edge is highlighted by a white circle and the dashed lines indicate the direction of the flow from the trailing edge. The phased averaged images are colored green to mimic the phosphorescence color of the actual tagged regions in the flow.

These 4 images portray the average state of the wake flow at different phases of one airfoil oscillation period, denoted by ϕ varying from 0 to 1. Figure 6.2a corresponds to the start of each oscillation cycle, described with $\phi = 0$ and defined as when the airfoil is at $\alpha = 0^\circ$ and is pitching upward with $\frac{d\alpha}{dt} > 0$. This means that the trailing edge of the airfoil is moving downward in this picture. The location and motion direction of the trailing edge are marked on each image as well. Figures 6.2b and 6.2d show the flow field when airfoil is at $\alpha = +2^\circ$ and $\alpha = -2^\circ$, respectively ($\phi = 0.25$ and 0.75), while Figure 6.2c coincides with $\alpha = 0^\circ$ and $\frac{d\alpha}{dt} < 0$ ($\phi = 0.5$), where the airfoil is pitching downward and the trailing edge is moving up.

To facilitate following the development of the flow in these figures, the approximate locations of the two most recently formed vortices can be detected at $\phi = 0$ and tracked in the sequence of images. For example, in Figure 6.2a, these two vortices are approximately located at $x/c \sim 0.02$ and 0.27 near the centerline, which then move to around $x/c \sim 0.14$ and 0.42 in the second image (Figure 6.2b).

Corresponding images for the same oscillation parameters in steady shear and unsteady shear layers are presented in Figures 6.3 and 6.4 respectively. It should be noted that in the cases with non-uniform flow, the high speed side is passing over the top side of the airfoil as shown in these figures, meaning at $\phi = 0$ the airfoil leading edge moves towards the high speed side and its trailing

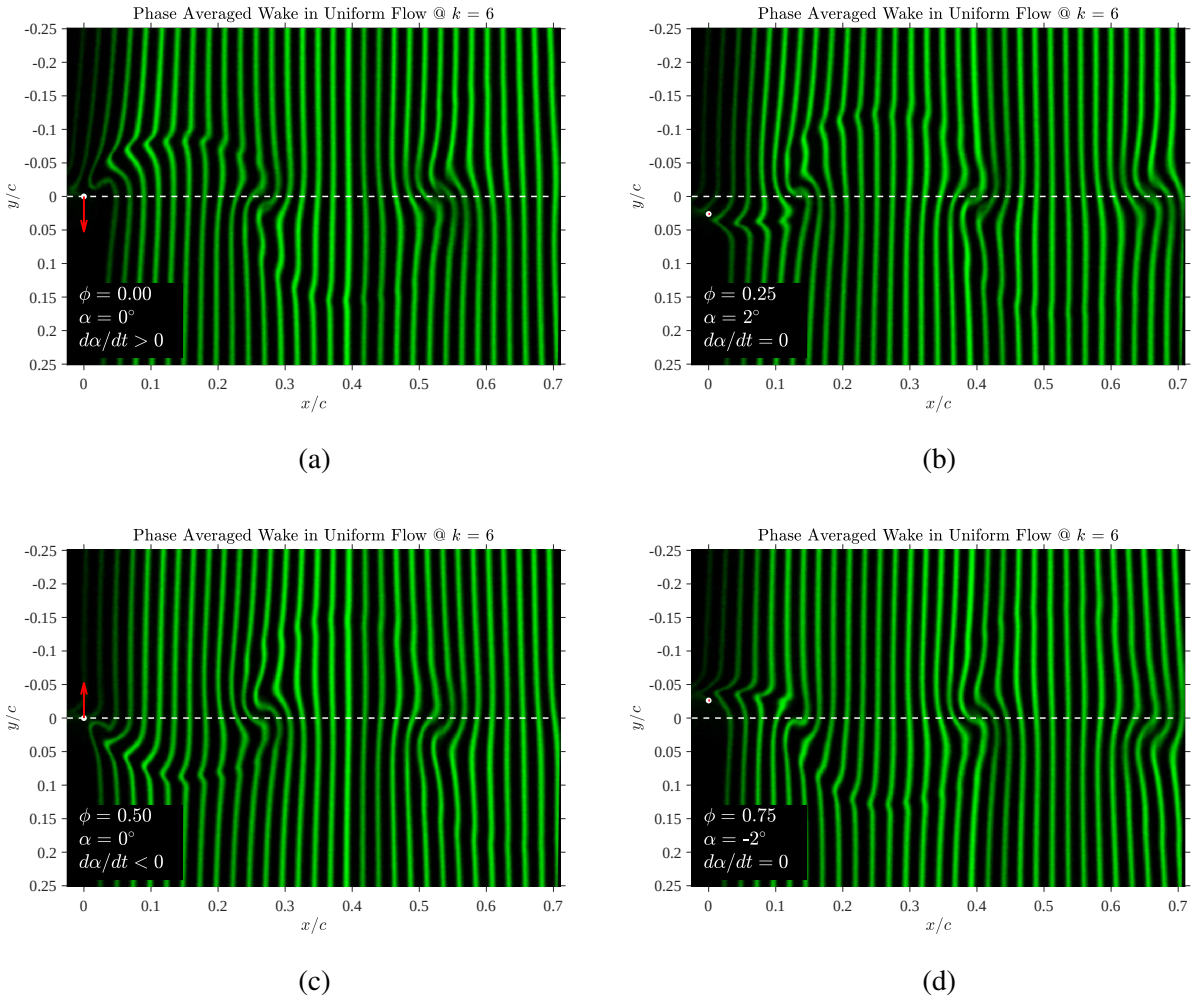

Figure 6.2: Phase averaged molecular tagging visualization of the flow in the wake of an oscillating NACA0012 airfoil with oscillation amplitude of $\alpha_0 = 2$ at a reduced frequency of $k = 6$ in uniform flow at 4 different phases of one airfoil oscillation cycle. The location of the trailing edge is highlighted by a white circle and the dashed lines indicate the direction of the flow from the trailing edge. The red arrows indicate the direction of trailing edge motion.

edge goes in the direction of the low speed side.

In the phase averaged image sequences for both the uniform and steady shear flows (Figures 6.2 and 6.3), the vortices travel parallel to the flow and are nearly aligned with the wake centerline. This observation is in agreement with experiments of Bohl (2002) and Bohl & Koochesfahani (2009) for this airfoil motion in uniform flow and numerical results of Hammer et al. (2019) for both a similar uniform flow and a linear steady shear layer (see Figure 6.5).

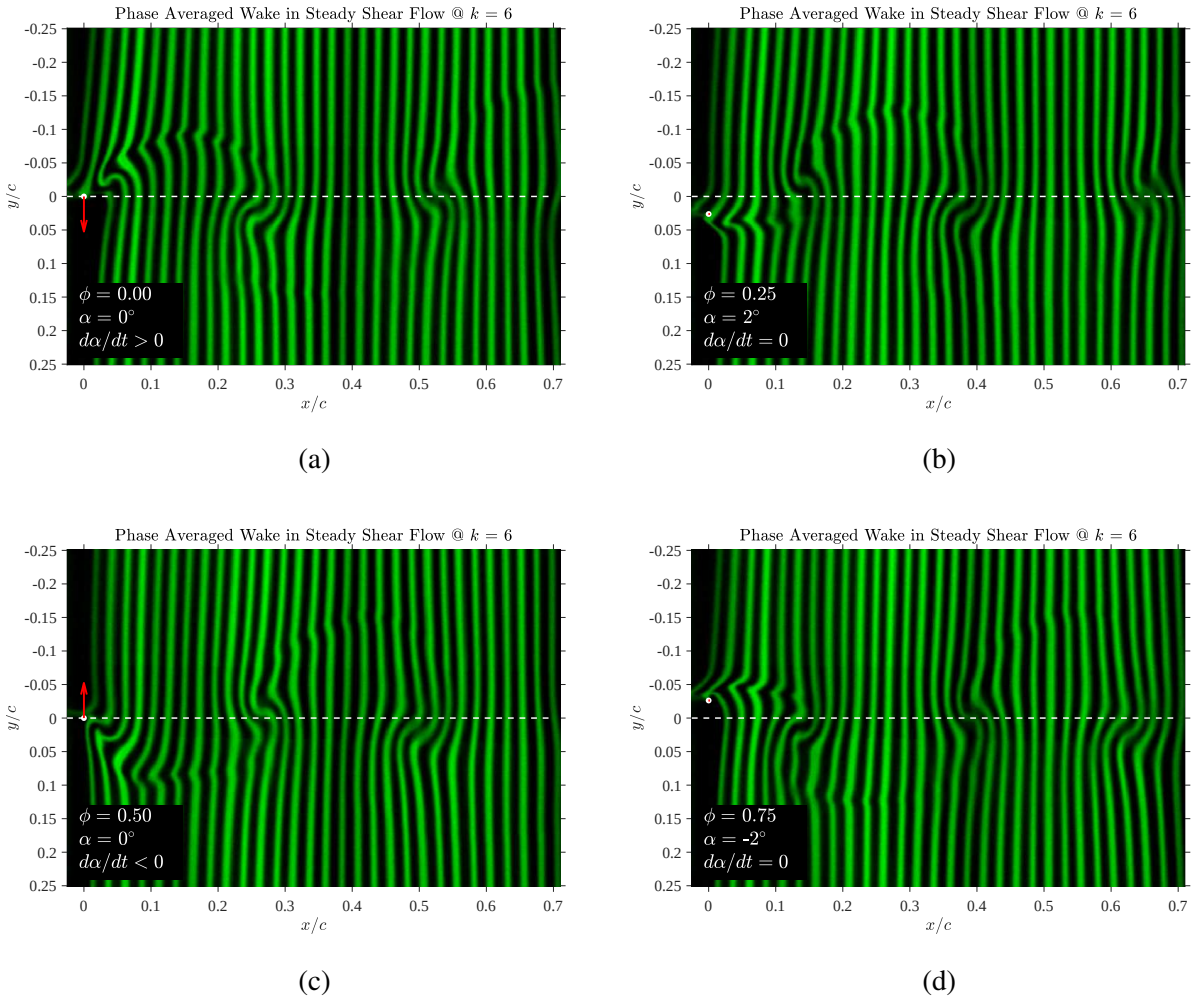

Figure 6.3: Phase averaged molecular tagging visualization of the flow in the wake of an oscillating NACA0012 airfoil with oscillation amplitude of $\alpha_0 = 2$ at a reduced frequency of $k = 6$ in steady shear layer at 4 different phases of one airfoil oscillation cycle. The location of the trailing edge is highlighted by a white circle and the dashed lines indicate the direction of the flow from the trailing edge. The red arrows indicate the direction of trailing edge motion.

While the wake flow field in the unsteady shear layer indicates similar flow features as the previous two flows, it is harder to follow the structures clearly due to the blurry averaged lines. This is a direct result of the high level of fluctuations in the approach flow which introduces large cycle to cycle variations to the mostly oscillatory flow. Figure 6.6 shows the phase averaged image of the flow field in the two stream shear layer at $\phi = 0$ (the same as Figure 6.4a) alongside 3 samples of the instantaneous images at this phase that are used to generate the phase averaged image. It can be

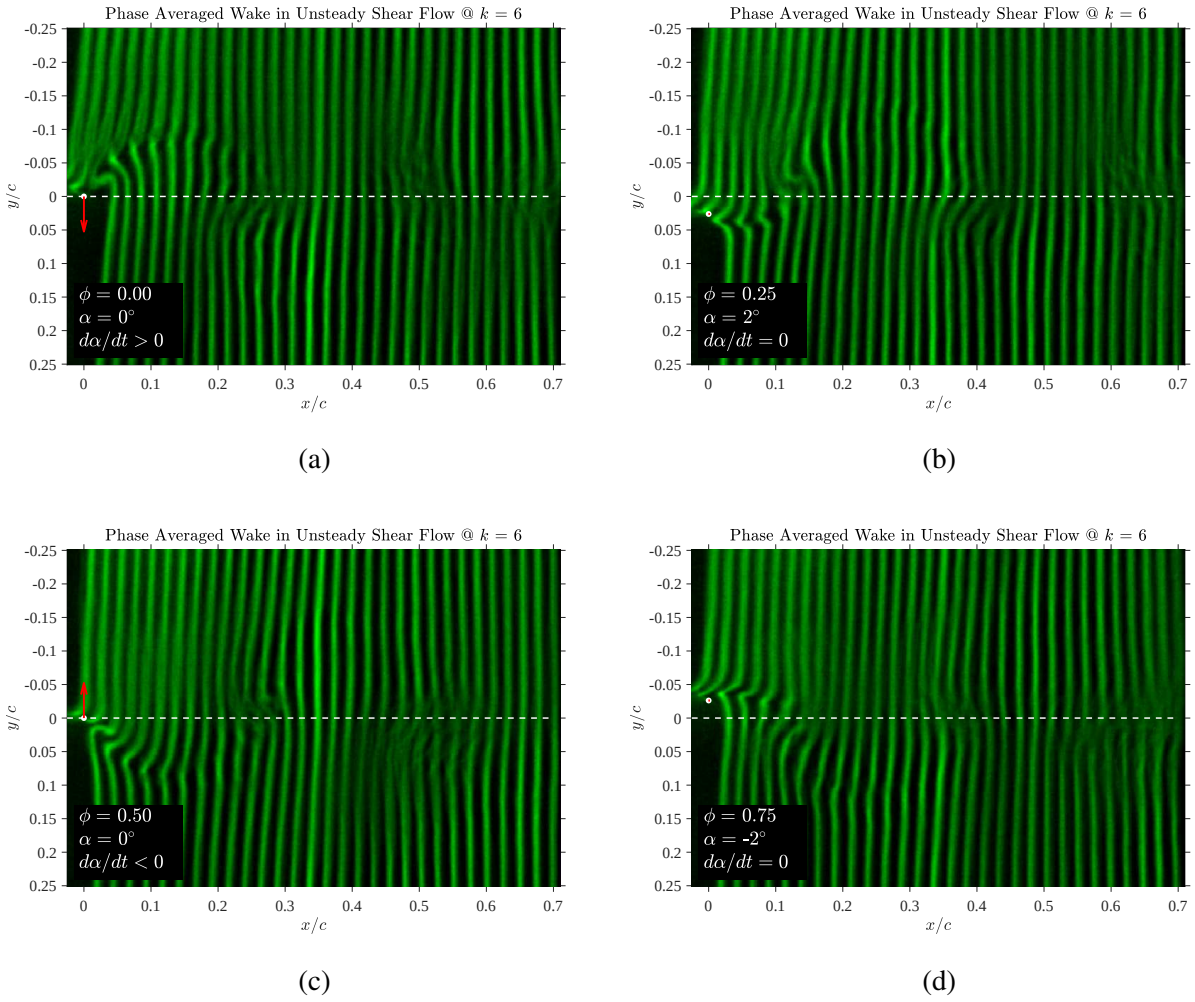

Figure 6.4: Phase averaged molecular tagging visualization of the flow in the wake of an oscillating NACA0012 airfoil with oscillation amplitude of $\alpha_0 = 2$ at a reduced frequency of $k = 6$ in unsteady shear layer at 4 different phases of one airfoil oscillation cycle. The location of the trailing edge is highlighted by a white circle and the dashed lines indicate the direction of the flow from the trailing edge. The red arrows indicate the direction of trailing edge motion.

seen that the two vortices located around $x/c = 0.22$ and 0.5 do not appear at the same location in these three images and their features are also not identical. Differences similar to the ones shown in Figure 6.6 between the instantaneous samples lead to the phase averaged images not being as sharp as for the other two flows shown here.

Figures 6.7, 6.8 and 6.9 compare the flow field in the wake of the airfoil oscillating with a reduced frequency of $k = 8$ in uniform flow, steady shear and unsteady shear layer respectively. The wake

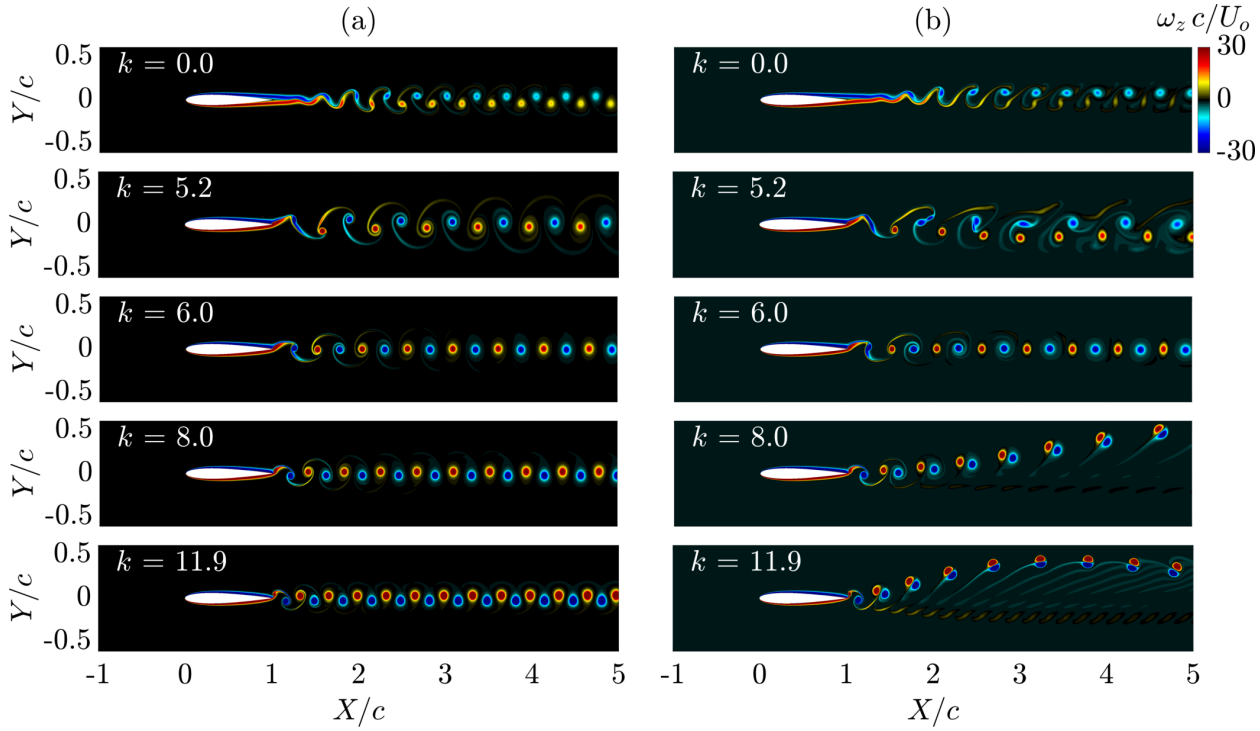

Figure 6.5: Instantaneous spanwise vorticity fields for **(a)** uniform flow and **(b)** linear steady shear flow simulated by Hammer et al. (2019). The airfoil is at $\alpha = 0^\circ$ and pitching up. (Figure Courtesy of Hammer et al., 2019)

in the uniform flow shows the signature of a reverse von Kármán vortex street pattern, which travels parallel to the free-stream flow. The steady shear flow displays a similar vortex arrangement pattern as the reverse von Kármán vortex street, but the vortices deflect upward towards the high speed side of the shear layer as they progress downstream. This is consistent with simulations of Hammer et al. (2019) which demonstrated after $k = 8$, the angle of wake deflection increases with reduced frequency (see Figure 6.5). This increase in deflection angle is observed in current visualizations as well, as shown in Figure 6.10 for a reduced frequency of $k = 10$ in the steady shear layer.

Another interesting feature of the flow in the steady shear layer at this reduced frequency ($k = 10$) is that the two vortices shed in the same airfoil oscillation get close to each other while they travel downstream, and upward towards the high speed side. This pattern also occurs in the unsteady shear flow (Figure 6.11), which mainly displays similar general features to that of the steady shear flow. Although performed on different two-stream shear layers, the airfoil oscillation and other flow parameters of this case are close to the experiments of Naguib & Koochesfahani

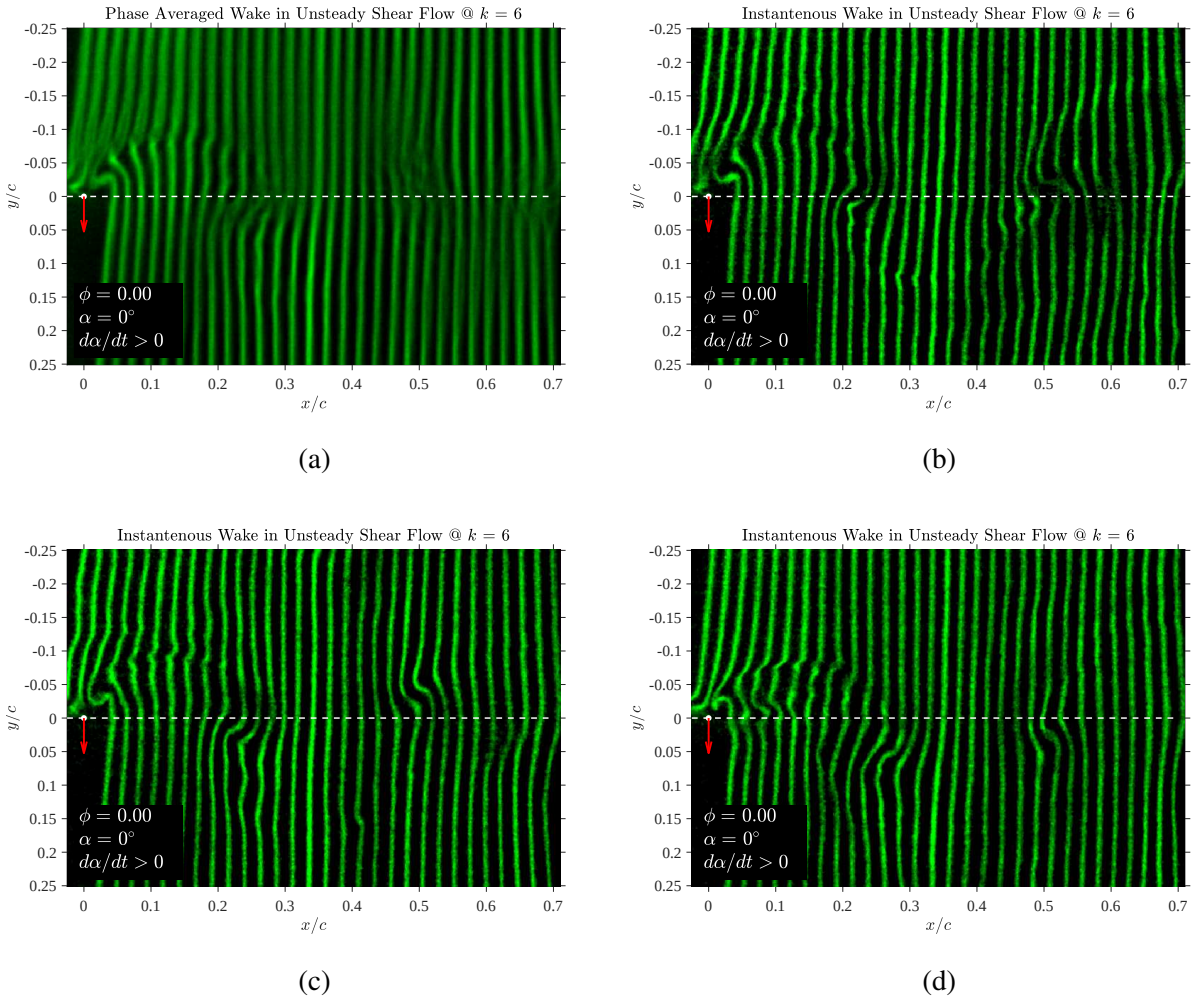

Figure 6.6: **(a)** Phase averaged molecular tagging visualization of the flow in the wake of an oscillating NACA0012 airfoil with oscillation amplitude of $\alpha_0 = 2$ at a reduced frequency of $k = 6$ in unsteady shear layer at starting phase of one airfoil oscillation cycle. **(b)** through **(c)** show sample instantaneous molecular tagging visualization images from the same case and phase in cycle used to generate **(a)**. The location of the trailing edge is highlighted by a white circle and the dashed lines indicate the direction of the flow from the trailing edge. The red arrows indicate the direction of trailing edge motion.

(2012), where their phase-resolved spatial map of the streamwise velocity for one oscillation cycle at one chord length downstream of the trailing edge showed evidence of only one region of velocity undershoot/overshoot, suggesting only one vortex was shed during each airfoil oscillation cycle in the presence of the unsteady shear flow (see Figure 6.12). Based on the indications from Figure 6.11, it is possible that the close proximity of the two vortices in the wake of the oscillating airfoil

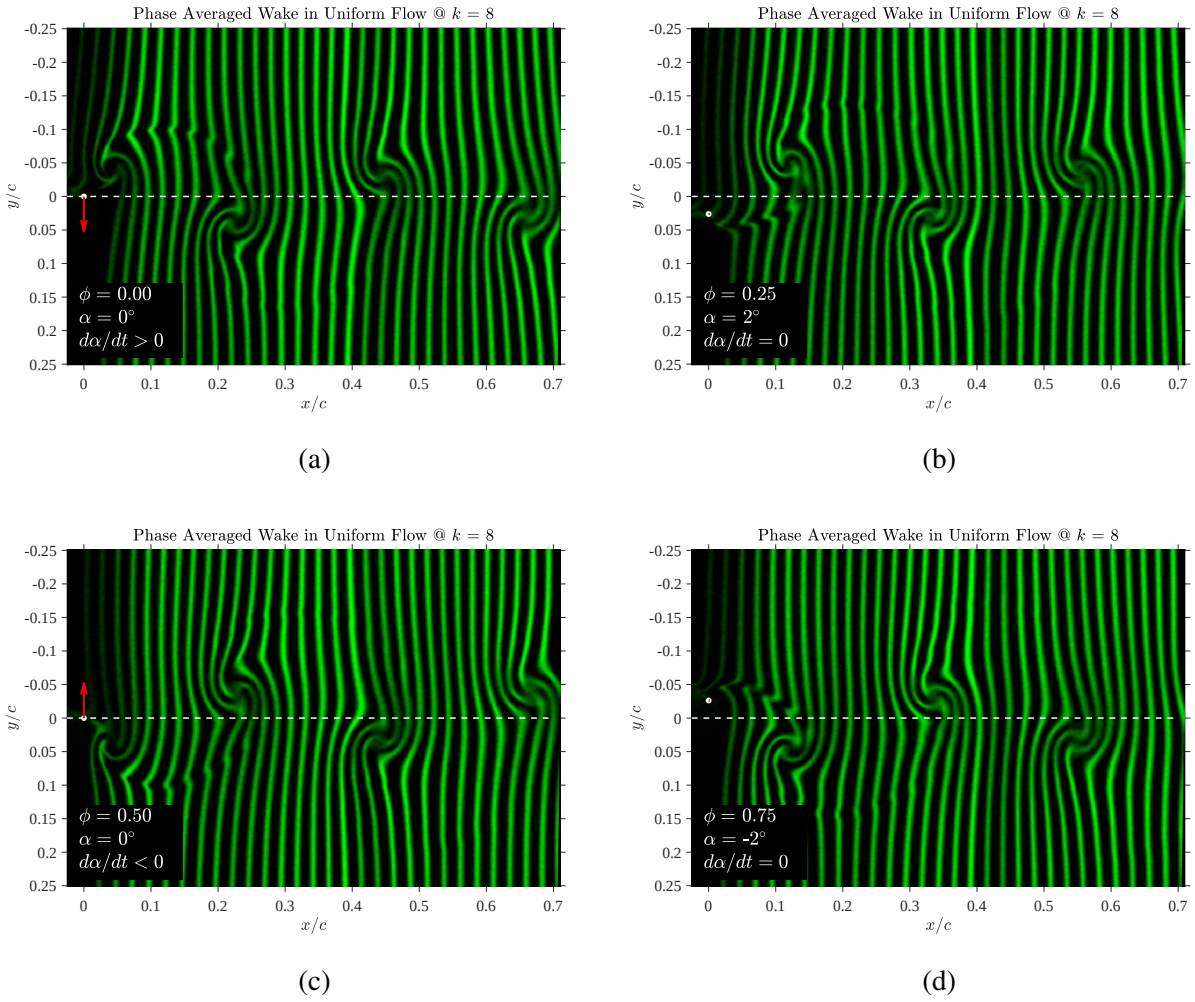

Figure 6.7: Phase averaged molecular tagging visualization of the flow in the wake of an oscillating NACA0012 airfoil with oscillation amplitude of $\alpha_0 = 2$ at a reduced frequency of $k = 8$ in uniform flow at 4 different phases of one airfoil oscillation cycle. The location of the trailing edge is highlighted by a white circle and the dashed lines indicate the direction of the flow from the trailing edge. The red arrows indicate the direction of trailing edge motion.

in the unsteady shear layer combined with the high level of fluctuations in the flow may have contributed to only one vortex being detected in the work of Naguib & Koochesfahani (2012).

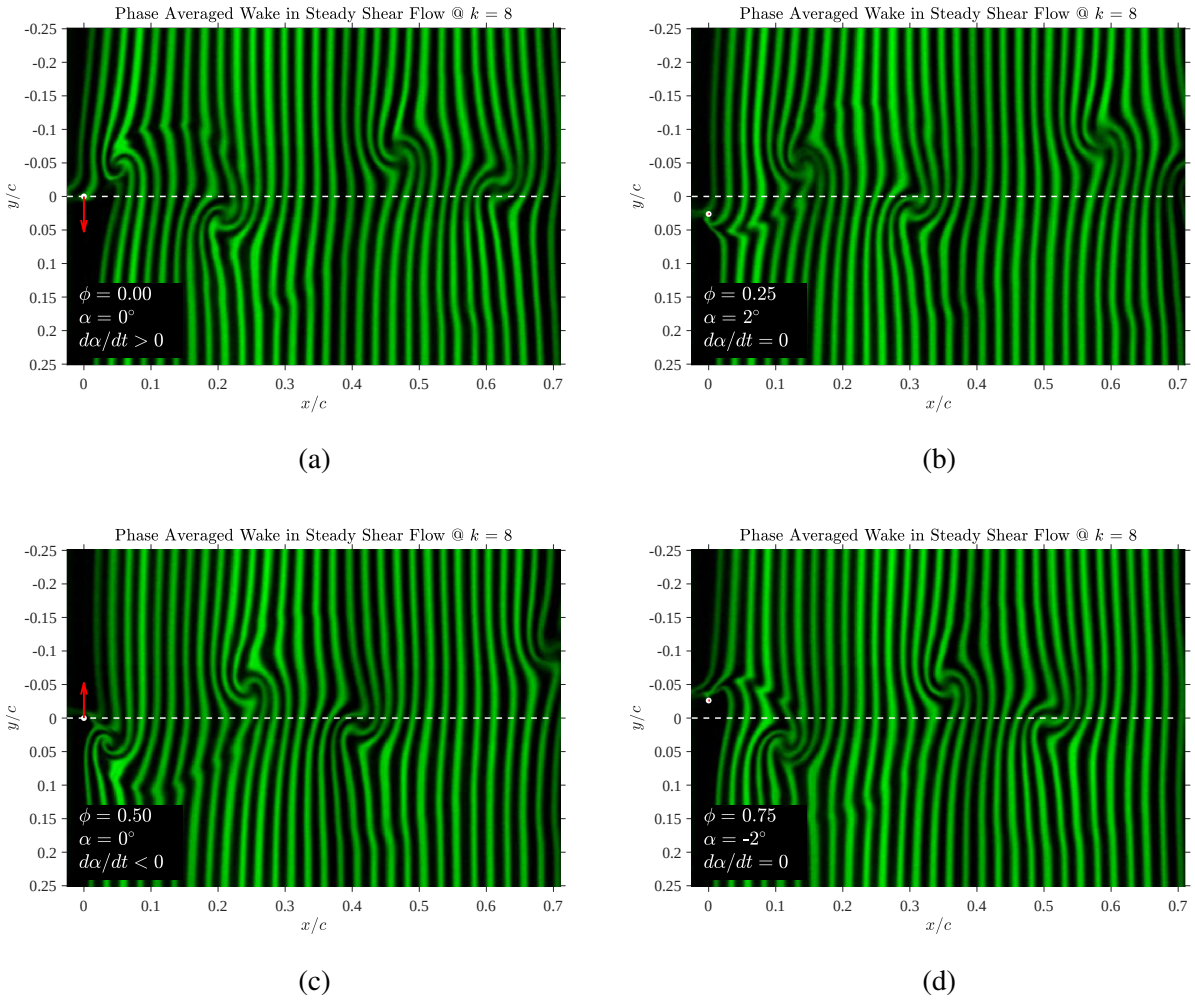

Figure 6.8: Phase averaged molecular tagging visualization of the flow in the wake of an oscillating NACA0012 airfoil with oscillation amplitude of $\alpha_0 = 2$ at a reduced frequency of $k = 8$ in steady shear layer at 4 different phases of one airfoil oscillation cycle. The location of the trailing edge is highlighted by a white circle and the dashed lines indicate the direction of the flow from the trailing edge. The red arrows indicate the direction of trailing edge motion.

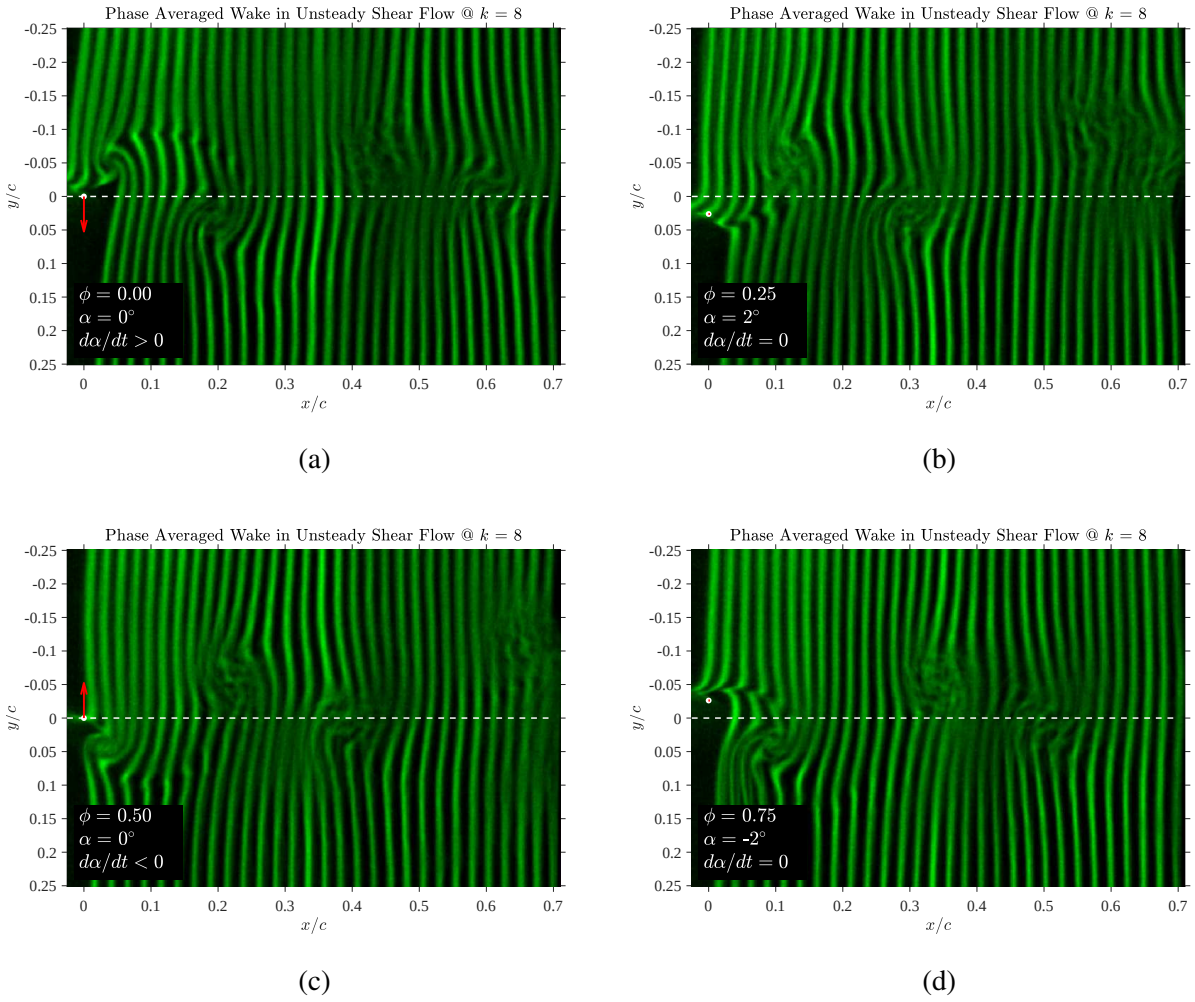

Figure 6.9: Phase averaged molecular tagging visualization of the flow in the wake of an oscillating NACA0012 airfoil with oscillation amplitude of $\alpha_0 = 2$ at a reduced frequency of $k = 8$ in unsteady shear layer at 4 different phases of one airfoil oscillation cycle. The location of the trailing edge is highlighted by a white circle and the dashed lines indicate the direction of the flow from the trailing edge. The red arrows indicate the direction of trailing edge motion.

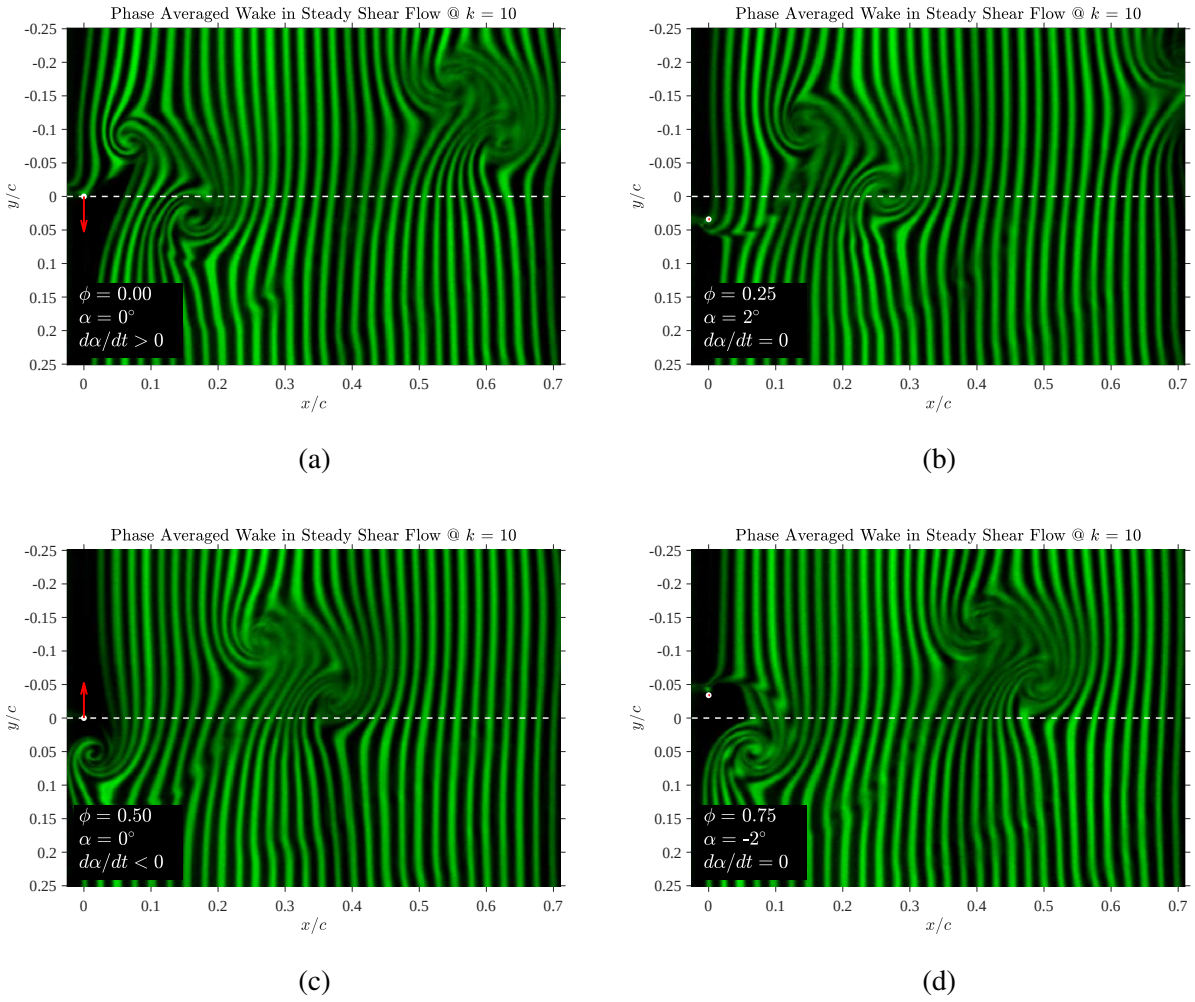

Figure 6.10: Phase averaged molecular tagging visualization of the flow in the wake of an oscillating NACA0012 airfoil with oscillation amplitude of $\alpha_0 = 2$ at a reduced frequency of $k = 10$ in steady shear layer at 4 different phases of one airfoil oscillation cycle. The location of the trailing edge is highlighted by a white circle and the dashed lines indicate the direction of the flow from the trailing edge. The red arrows indicate the direction of trailing edge motion.

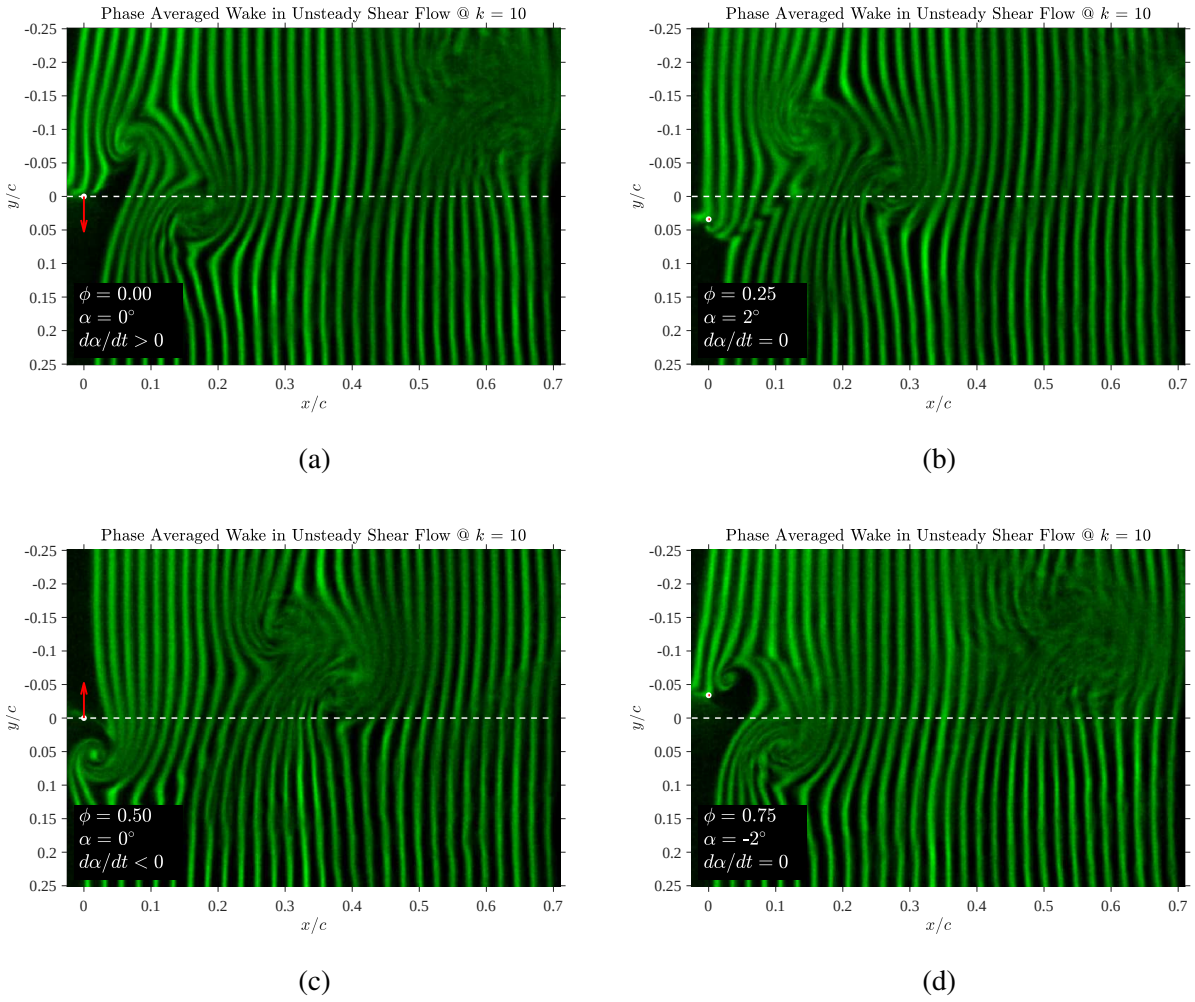

Figure 6.11: Phase averaged molecular tagging visualization of the flow in the wake of an oscillating NACA0012 airfoil with oscillation amplitude of $\alpha_0 = 2$ at a reduced frequency of $k = 10$ in unsteady shear layer at 4 different phases of one airfoil oscillation cycle. The location of the trailing edge is highlighted by a white circle and the dashed lines indicate the direction of the flow from the trailing edge. The red arrows indicate the direction of trailing edge motion.

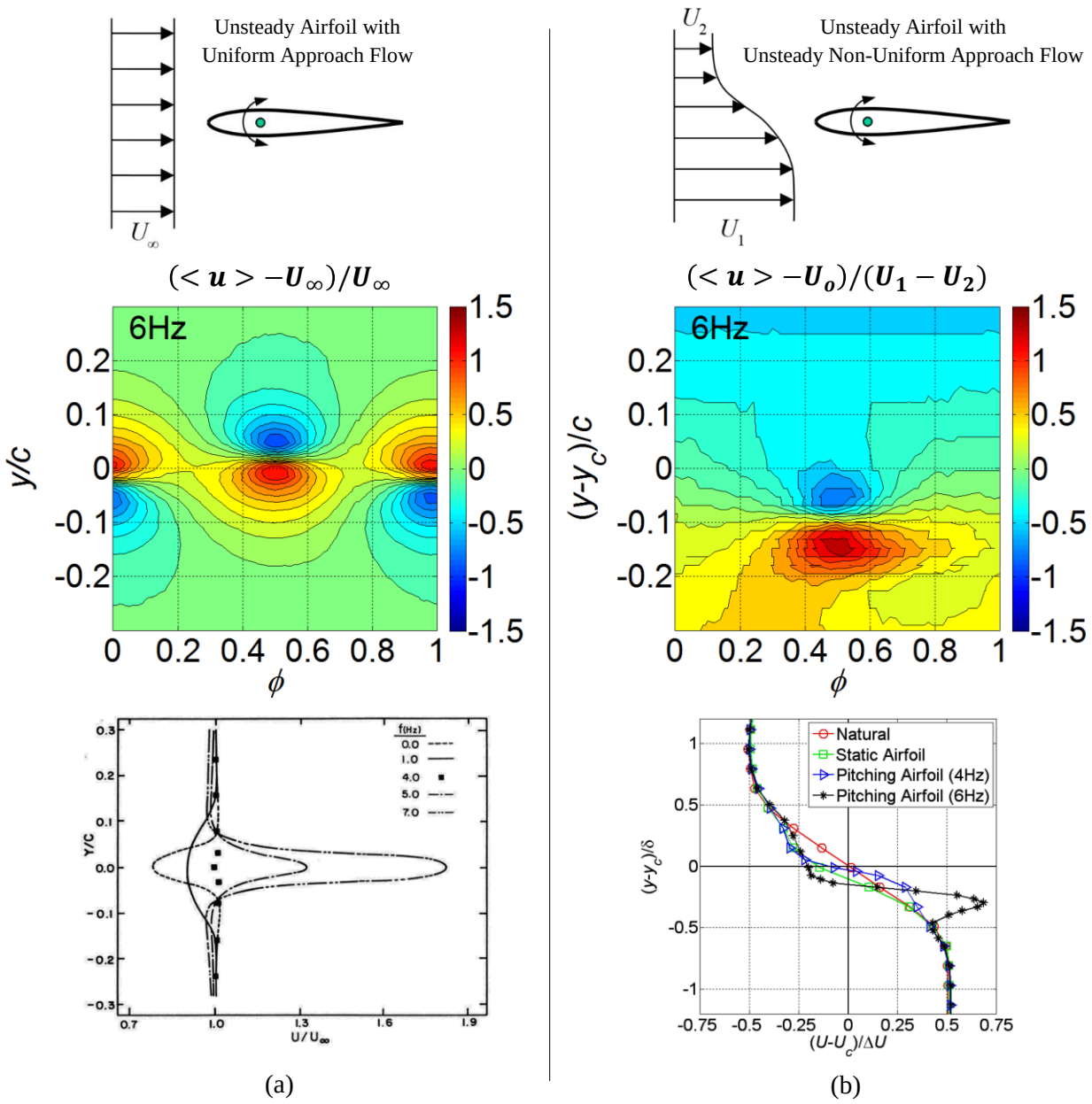

Figure 6.12: Color contour map of phase-averaged streamwise velocity results of Naguib & Koochesfahani (2012), showing the variation of velocity profiles with phase during one cycle of oscillation in the wake of the pitching airfoil ($k = 10.6$, $\alpha_0 = 2°$). **(a)** The baseline case of uniform approach flow shows the expected signature of alternating sign vortex pair. **(b)** In the case of shear layer approach flow, there is evidence for only one vortex core. (Figure courtesy of Naguib & Koochesfahani, 2012)

CHAPTER 7

CONCLUSIONS

Motivated by many situations of complex, non-uniform and mostly unsteady flows encountered in nature, this study experimentally explores how the unsteady behavior of a shear flow affects the aerodynamic performance of a NACA0012 airfoil in low Reynolds numbers ($Re = 1.2 \times 10^4$). This objective is achieved by examining the performance of the airfoil in static condition over a range of angles of attack, as well as when it is pitching sinusoidally around its quarter chord with a small oscillation amplitude over a range of oscillation frequencies.

The effects of shear flow unsteadiness are isolated from those of the mean shear flow itself by performing the measurement in 2 different shear flows with matching mean velocity profiles where one has a uniform distribution of low level fluctuations while the other exhibits large scale spatially non-uniform fluctuations. This way it would be possible to discern between the effects attributed to the mean shear profile from those caused by unsteadiness of the shear flow.

A plane mixing layer is selected as a representative of an unsteady shear layer, since they are very well studied and are known to contain vortical structures and high level of fluctuations. Such two-stream shear layer with a centerline velocity of 10 cm/s and a two-to-one velocity ratio is generated in the water tunnel facility. The behavior of the resulting two stream shear layer is characterized through measurements of its streamwise velocity profile at multiple downstream locations utilizing single component molecular tagging velocimetry. After a development length, the two-stream shear layer is found to produce the typical self-similar hyperbolic tangent mean velocity profile and a spatially non-uniform fluctuations profile with a high level of fluctuations in the center and a gradual decrease in fluctuations moving away from the shear layer center line. The two stream shear layer width increases linearly as a function of downstream distance with a growth rate similar to the ones reported in literature for two-stream shear layers.

After validating the behavior of the unsteady shear layer, the mean velocity profile of this two-stream shear layer at a specific downstream location ($x - x_0 = 107$ cm) is used as a reference for

generation of a duplicate steady shear flow. The steady counterpart of this shear layer is produced by a shaped honeycomb shear generation method based on the original model proposed by Kotansky (1966). This modified model utilizes a variable friction factor model to estimate the pressure drop of the laminar flow inside honeycomb tubes (applicable inside and after the tube entrance length). Additionally, the model is further refined to eliminate the need to calibrate the pressure drop experimentally for each design. The effectiveness of the modified method is demonstrated through its ability to generate the desired velocity profile with high fidelity while maintaining velocity fluctuation levels at or below that of the freestream prior to installation of the device. Mean streamwise velocity profiles measured in this steady shear flow show a good agreement with the mean velocity profile of the target two-stream shear layer, while its streamwise velocity fluctuations are spatially uniform and at the level of the background fluctuations in the test facility

With a pair of matching steady and unsteady shear flows, aerodynamic force measurements are performed on a stationary airfoil over a wide range of angles of attack, placed at the center of each shear layer as well as in the reference uniform freestream flow. In the presence of steady shear approach flow, the lift coefficient curve exhibits the same general trend as that of the uniform flow and it produces a negative lift at zero angle of attack, which is consistent with the results of Hammer et al. (2016, 2018, 2019) and Olson et al. (2016). However the unsteady shear approach flow resulted in a significantly different behavior of the lift curve, where the region around zero angle of attack shows a linear behavior with a larger slope and extending over a larger range of angles of attack compared to that of steady shear and uniform flow. Furthermore, the unsteady shear flow induces a positive lift at zero angle of attack. This behavior of the lift curve in the unsteady shear layer is hypothesized to be due to effects of high levels of fluctuations present in the approach flow on the laminar separation on the surface of the airfoil. The unsteady shear flow also generates a smaller amplitude of drag over small angles of attack compared to both uniform and steady shear flows.

Force measurements on the pitching airfoils show that at small oscillation frequencies ($k < 2.5$), the steady and unsteady shear flows produce opposite sign lift forces consistent with their static

performance, but both result in positive lift coefficients of similar magnitudes at higher reduced frequencies ($k > 4$). The presence of shear and its unsteadiness seem to only weakly affect the mean and fluctuations of the streamwise force, with almost no effect observed on lift fluctuations. These observations are in agreement with findings of Hammer et al. (2019).

To look further into the hypothesis of the laminar separation being affected by the unsteady shear layer, streamwise velocity of the flow around the airfoil is measured in both shear flows with the stationary airfoil set at multiple angles of attack. In the steady shear approach flow, all of the angles of attack investigated here ($-6 < \alpha < +6$), demonstrate a region of reverse flow on the suction side of the airfoil, indicating the presence of a laminar separation. However, none of the angles of attack in the unsteady shear flow show any sign of a reverse flow region. This suggests that the high level of fluctuations in the unsteady shear flow have significantly affected the formation of laminar separation.

Flow visualizations in the wake of the pitching airfoil through molecular tagging flow visualization shows that at the high reduced frequencies visualized here ($k \geq 6$), the overall behavior of the wake flow and vortical structures is similar for both steady and unsteady shear flows, with the wake flow deflecting towards the high speed side of the flow at higher frequencies ($k > 7$). The main difference between the observations from the steady vs unsteady shear layer is the fact that the unsteady shear layer results exhibit larger perturbations to the vortex arrangement and considerable cycle to cycle variations.

APPENDICES

APPENDIX A

SHAPED HONEYCOMB SHEAR GENERATION METHOD

With the purpose of improving the performance of the original variable length honeycomb model, our proposed modified model utilizes a variable friction factor coefficient model to estimate the pressure drop inside honeycomb tubes. This friction factor coefficient model is applicable inside the tube entrance length as well as in the fully developed region, in the limit of laminar flow inside tubes ($Re_d \leq 2300$), and is a function of tube length and Reynolds number. Additionally, the model is further refined to eliminate the need to calibrate the pressure drop experimentally for each design. With these modifications, the new method can be used in two fashions: to design a honeycomb shape required to generate a desired non-uniform velocity profile; and to predict the velocity profile resulting from a given honeycomb shape profile under different operating conditions. The performance of the proposed technique is investigated through experimental measurements of streamwise velocity downstream of two sample honeycomb devices. Furthermore, the downstream evolution of the flow after the honeycomb device is studied to determine the distance required for the flow to develop into the smooth desired velocity profile.

A.1 Theoretical Model

The present model follows the same main assumptions as in the original model by Kotansky (1966). A schematic of the model and its main assumptions is shown in Figure A.1. The flow far upstream of the honeycomb ($x_{-\infty}$) is assumed to be a uniform flow with known inlet velocity ($u_{-\infty}$) and uniform pressure distribution ($P_{-\infty}$). Far downstream of the honeycomb ($x_{+\infty}$), the velocity profile is expected to have developed into the known and desired velocity profile, $u(y)$, with the uniform pressure distribution ($P_{+\infty}$). Furthermore, Kotansky (1966) presumed that the flow entering/exiting each honeycomb tube has the streamwise velocity equal to the desired velocity profile, $u(y)$ and the flow exiting honeycomb tubes is only in the streamwise direction.

Following these assumptions, the overall pressure change (ΔP) between far upstream and far

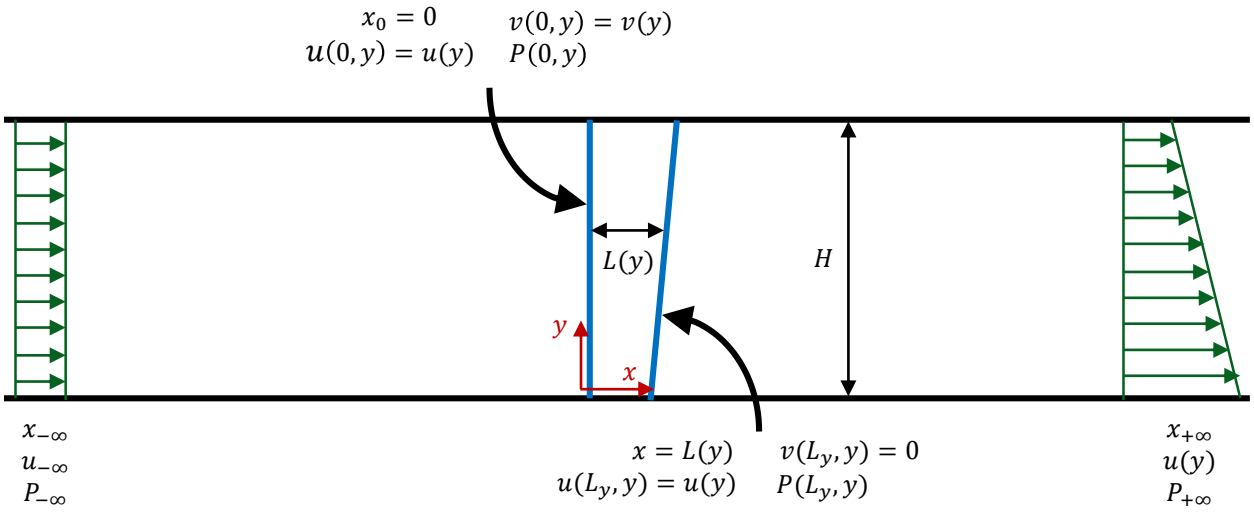

Figure A.1: A schematic of the variable length honeycomb model along with the main assumptions involved.

downstream can be divided into 3 segments as:

$$\Delta P = P_{-\infty} - P_{+\infty} = \Big[P_{-\infty} - P(0,y)\Big] + \Big[P(0,y) - P(L,y)\Big] + \Big[P(L,y) - P_{+\infty}\Big]. \tag{A.1}$$

The first term on the right hand side of Equation A.1 is the pressure change upstream of the honeycomb, the second term represents the pressure drop within the honeycomb tubes, and the last term stands for the pressure change downstream of the honeycomb. Similar to the original model, upstream of the honeycomb is treated as a potential region and the pressure change in this potential region (the first term) is found using Bernoulli's equation. The pressure drop inside the honeycomb tubes (the second term) is estimated using a friction factor coefficient and the Darcy-Weisbach equation. The pressure change downstream of the honeycomb (the third term) is assumed to be negligible compared to the other two terms, consistent with Kotansky (1966) assumption of parallel streamlines downstream of the honeycomb. The entrance and exit losses are ignored in this analysis.

The terms $\Big[P_{-\infty} - P(0,y)\Big]$ and $\Big[P(0,y) - P(L,y)\Big]$ in Equation A.1 can be substituted from Bernoulli's equation on a streamline (between far upstream and the entrance of the honeycomb) and Darcy-Weisbach equation respectively, which then after rearrangement yields:

$$L(y) = \frac{d}{4f}\left[\frac{\frac{2}{\rho}\Delta P + {u_{-\infty}}^2 - v(y)^2}{u(y)^2} - 1\right], \tag{A.2}$$

where $L(y)$ is the honeycomb tube length at each y, d the honeycomb tube diameter, f the Fanning friction factor and ρ the fluid density. In order to use Equation A.2 to calculate the honeycomb length distribution, one still needs to find the distribution of lateral component of the velocity entering the honeycomb tubes, $v(y)$, Fanning friction factor, f, and the overall pressure drop value, ΔP.

A.1.1 Distribution of Cross-Stream Velocity Component, $v(y)$

As mentioned previously, Kotansky (1966) considered the flow upstream of the honeycomb, excluding wall boundary layers, as a potential flow with $\nabla^2\psi = 0$, where ψ is the two-dimensional stream function. The boundary conditions of this potential flow region include no flow normal to the side walls, undisturbed parallel flow at far upstream, and $u(y)$ as the known streamwise component of velocity entering the honeycomb at $x = 0$. Applying these boundary conditions to the general potential flow solution, the cross-stream component of velocity at the entrance of the honeycomb, $v(y)$ can be estimated as:

$$v(y) = \sum_{n=1}^{\infty} a_n \frac{n\pi}{H} \sin\frac{n\pi y}{H}, \tag{A.3}$$

where a_n are coefficients of the Fourier series representing the difference between streamwise component of velocity entering the honeycomb and the uniform velocity of far upstream:

$$a_n = \frac{2}{n\pi}\int_0^H \cos\frac{\pi y}{H}\left[u(y) - u_{-\infty}\right] dy. \tag{A.4}$$

A.1.2 Friction Factor, f

The original model of Kotansky (1966) assumed that the flow was fully developed in all of the honeycomb tubes and used an experimentally measured constant friction factor coefficient for all of the honeycomb tubes. However, as mentioned previously, this assumption is not always valid. The

two most probable instances that this assumption fails are when the honeycomb tubes are not long enough (due to material, fabrication or facility size constraints), or when lower Reynolds number ranges are of interest. Utilizing shorter tubes means there is no guarantee that the flow is fully developed in all of the tubes, while operating in lower Reynolds number ranges entails that the variation of even fully developed friction factor coefficient with Reynolds number is not negligible, as Reynolds number can vary by a factor of 2-3 across the honeycomb device. Moreover, based on the relationship suggested by Shah (1978) for a laminar developing flow in a circular tube, a tube length of approximately 5 times the commonly defined entrance length (where the centerline velocity reaches 99% of fully developed velocity limit) is required for the apparent friction factor to approach within 5% of the fully developed friction factor value. A more recent scaling analysis for internal laminar flows by Muzychka & Yovanovich (2009) suggests that it can take about 10 times the entrance length for all boundary layer effects to be lost in the pressure drop. These highlight the shortcomings of a constant friction factor coefficient assumption when laminar flow could be present inside honeycomb tubes.

Thus, for a more general and accurate variable length honeycomb model, it is required to utilize a variable friction factor coefficient model that is valid for the entire range of developing flow to fully developed flow. This demands the friction factor coefficient model to be a function of both tube length and Reynolds number. For the proposed variable length honeycomb method, such a variable friction factor model proposed by Du Plessis & Collins (1992) is employed. This model estimates the apparent friction factor coefficient of a laminar flow within tubes of different cross-sections in the range of developing to fully developed flows. For a simple circular tube, the apparent friction factor can be approximated by:

$$f(y) = \frac{16}{Re_d(y)} \left[1 + \left(\frac{0.0462}{x_y^+} \right)^{\frac{2.17}{2}} \right]^{\frac{1}{2.17}}, \tag{A.5}$$

where $Re_d(y)$ is the Reynolds number based on tube diameter and x_y^+ the dimensionless axial

distance from tube entrance at each y:

$$x_y^+ = \frac{[L(y)/d]}{Re_d(y)}. \tag{A.6}$$

A.1.3 Overall Pressure Drop, ΔP

In order to use Kotansky's original method, one needs to find the value of overall pressure drop, ΔP, through calibration, by experimentally measuring the pressure difference between the far upstream and far downstream locations in the test section of the flow facility. This is not the best approach for a design method, though, since introducing the honeycomb device into the facility affects this overall pressure drop value. This calibration requirement leads to an iterative process for a more accurate design process. For a more robust approach in our modified model, this overall pressure drop term is calculated using a reference honeycomb length and other design specifications to eliminate the need for a priori requirement of ΔP during the design of the honeycomb tube length distribution.

Considering $\Delta P = P_{-\infty} - P_{+\infty}$ is uniform across the channel width, once its value is found at one point, one can use the same value for the rest of the channel width. Using this approach, a prescribed reference honeycomb length can be assigned to a specific point in y, where both the velocity components are known. After estimating the friction factor coefficient based on this information, a reorganized version of Equation A.2 can be used to find ΔP for this point. In practice it is usually convenient to use the maximum honeycomb length (a practical constraint from raw material, manufacturing, or facility dimension limitations) as the reference length. This length typically coincides with where the lowest streamwise velocity would occur. This yields:

$$\Delta P = \Delta P_0 = \left(\frac{4 f_0 L_0}{d} + 1\right) \frac{1}{2}\rho u_0^2 + \frac{1}{2}\rho v_0^2 - \frac{1}{2}\rho u_{-\infty}^2, \tag{A.7}$$

where L_0 is the reference honeycomb length, and u_0, v_0 and f_0 are velocity components and friction factor coefficient that coincide with the y location of this reference honeycomb length.

A.1.4 Final Model

The incorporation of a variable friction factor coefficient model comes at the expense of making the final expression for the honeycomb length distribution implicit. To solve for the final honeycomb tube length distribution, one can rearrange Equation A.2 to isolate the unknown variables in the left hand side of the expression, as:

$$f(y)L(y) = \frac{d}{4}\left[\frac{\frac{2}{\rho}\Delta P + u_{-\infty}^2}{u(y)^2} - \frac{v(y)^2}{u(y)^2} - 1\right]. \tag{A.8}$$

For any specified velocity profile, $u(y)$, the right hand side of Equation A.8, $C(y)$, is known for every y location; through using Equation A.3 for cross-stream velocity component, $v(y)$, and Equation A.7 along with a reference honeycomb length for overall pressure drop, ΔP. Finally, inputting the expression for friction factor coefficient from Equations A.5 into the left hand side of Equation A.8 yields the final expression for honeycomb tube length distribution,

$$\frac{16}{Re_d(y)}\left[1 + \left(\frac{0.0462}{\frac{L(y)/d}{Re_d(y)}}\right)^{\frac{2.17}{2}}\right]^{\frac{1}{2.17}} = C(y), \tag{A.9}$$

where $L(y)$ is the only unknown. This expression can be numerically solved to obtain the honeycomb length distribution, $L(y)$, that would generate the specified desired velocity profile, $u(y)$.

A.2 Experimental Method

The performance of the proposed model is demonstrated by considering a hyperbolic tangent velocity profile (shown in Figure A.2) as the target velocity profile to be generated in a water tunnel facility with test section dimensions of 15 × 15 × 46 cm. The shear generation device was designed for a mean flow velocity of 10 cm/s and a maximum normalized shear rate of $K_{max} = \left(\frac{du}{dy}\right)_{max}\frac{H}{u_c} = 2.1$. A polycarbonate honeycomb (PC2 Polycarbonate Honeycomb, Plascore, Zeeland, MI) with circular 3.175 mm diameter tubes and a maximum tube length of 15 cm was used to fabricate the shear generation device. This maximum tube length was selected so

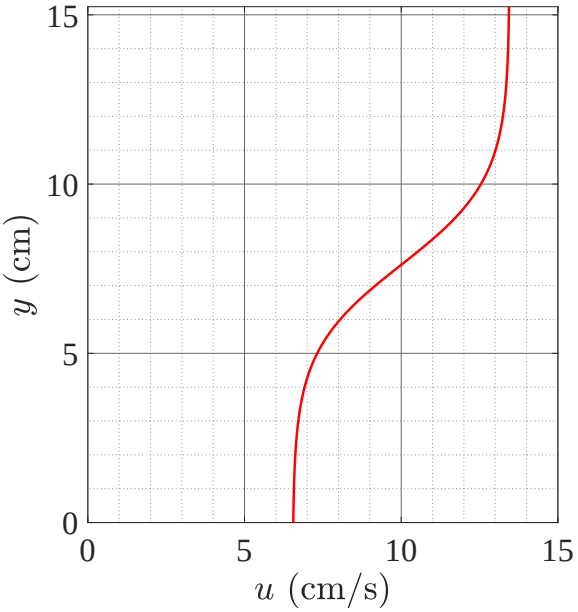

Figure A.2: Non-uniform hyperbolic tangent velocity profile selected with centerline velocity of $u_c = 10$ cm/s.

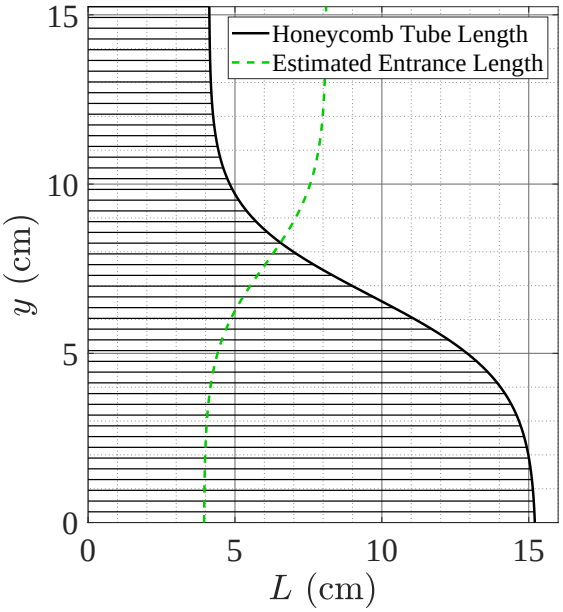

Figure A.3: Calculated honeycomb length distribution for the hyperbolic tangent profile based on the present model compared to the estimated entrance length of the flow at each y (based on $L_e \approx 0.06Re(y)$). The horizontal lines depict the approximate diameter of honeycomb tubes.

that the shear generation device would not occupy more than 1/3 of the test section in the facility, leaving enough space downstream of the device to observe the flow development.

Figure A.3 presents the designed honeycomb length distribution using our proposed model. An estimate of the entrance length distribution is also shown in Figure A.3 to highlight that more than 1/3 of the designed honeycomb tubes are shorter than the approximate entrance length, and hence, do not have fully developed flows. A specialized band saw blade (Simmons Knife & Saw, Glendale Heights, IL) was used to cut the designed honeycomb shape form a rectangular block with a uniform length of 15 cm. The final cut shear generation device is shown in Figure A.4.

Single component molecular tagging velocimetry (1c-MTV) is used to characterize the resulting mean and fluctuating velocity profiles and their streamwise development. In the single-component implementation of MTV used here, straight laser lines are used as the tagging pattern, with which,

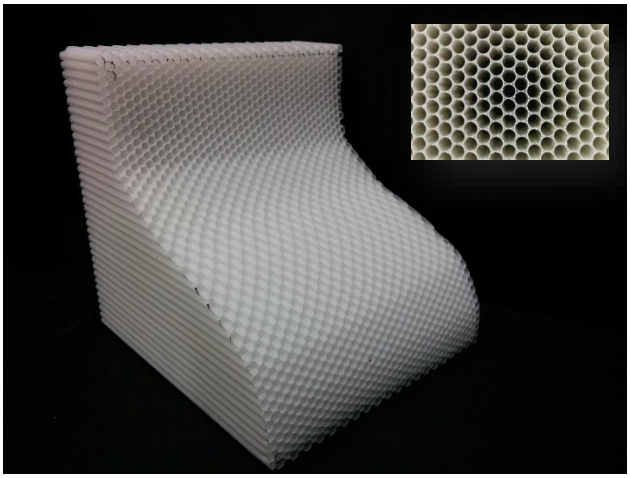

Figure A.4: Image of the shear generation device cut according to designed length profile based on the present model and shown in Figure A.3

only the streamwise component of the velocity field is obtained. A schematic of the measurement setup is provided in Figure A.5. Based on the flow velocity range and spatial correlation technique considerations, a time delay of 10 ms was used to capture 1024 undelayed and delayed images at a rate of 12.27 Hz. An average sample of the 1c-MTV image pair is presented in Figure A.6, where the green lines are the tagged regions in the fluid captured right after the laser pulse (Figure A.6i) and after the prescribed delay of 10 ms (Figure A.6ii). The yellow lines demonstrate the approximate location of the honeycomb tubes. Visually comparing the two average images of Figure A.6 quickly yields the flow pattern of small individual jets from each honeycomb tube and how they mix and become smoother as the flow develops downstream of the honeycomb.

A.3 Results

The streamwise development of the resulting non-uniform flow is presented in Figure A.7, where the mean velocity profiles measured from the honeycomb exit up to 20 cm $\left(\frac{x}{d} \approx 62\right)$ downstream are compared to the design velocity profile. Consistent with expectations, the flow at the exit of the device is dominated by the individual jets coming out from each honeycomb cell (see Figure A.7a), and quickly smooths out (Figure A.7b-c). The presence of individual jets is non-existent and the mean velocity profile shows a very good agreement with the design profile after a distance

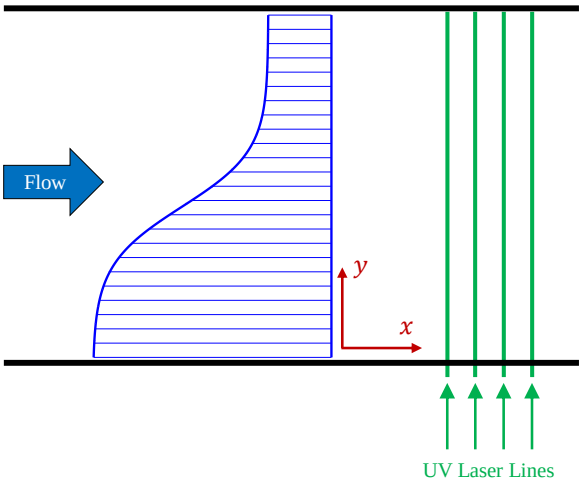

Figure A.5: A schematic of the flow measurement setup in the presence of the shear generation device.

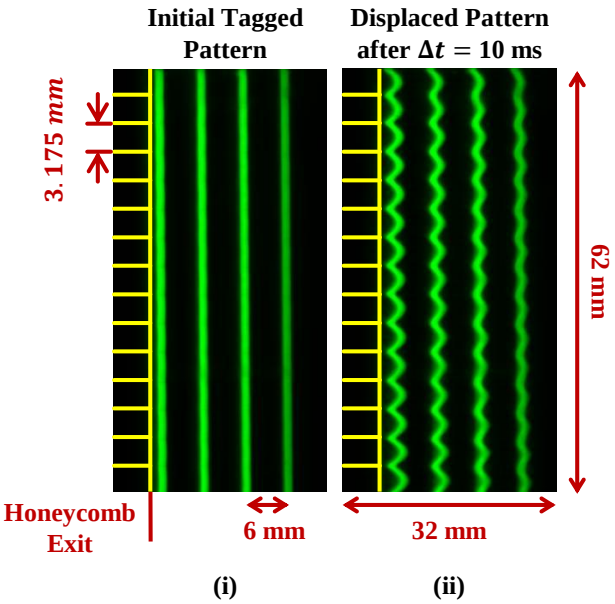

Figure A.6: A sample image pair showing a portion of the tagged region captured with a time delay of 10 ms. (i) the tagged region right after the laser pulse (ii) the same tagged region 10 ms later. The individual honeycomb cells are shown in yellow on the images.

of approximately 60 tube diameters (Figure A.7d).

Figure A.8 compares temporal velocity fluctuations of the hyperbolic tangent velocity profile at the downstream location where the mean velocity has become smooth, $\frac{x}{d} \approx 62$, with freestream temporal velocity fluctuations in the same location without the shear generation device present. Not only the addition of the honeycomb device does not induce any additional temporal velocity fluctuation, it even slightly reduces these fluctuations, a not so unexpected result considering the typical usage of honeycombs as flow management devices.

The smoothness of the velocity profile at each downstream location can be quantified by fitting a hyperbolic tangent curve to the measured velocity profile and calculating the root mean square of its spatial deviations, σ, from this curve. The reason behind using a hyperbolic tangent fit instead of the actual design velocity profile is to avoid introducing a bias error, especially at the initial locations, where the velocity profile has yet to develop into the design velocity profile. This

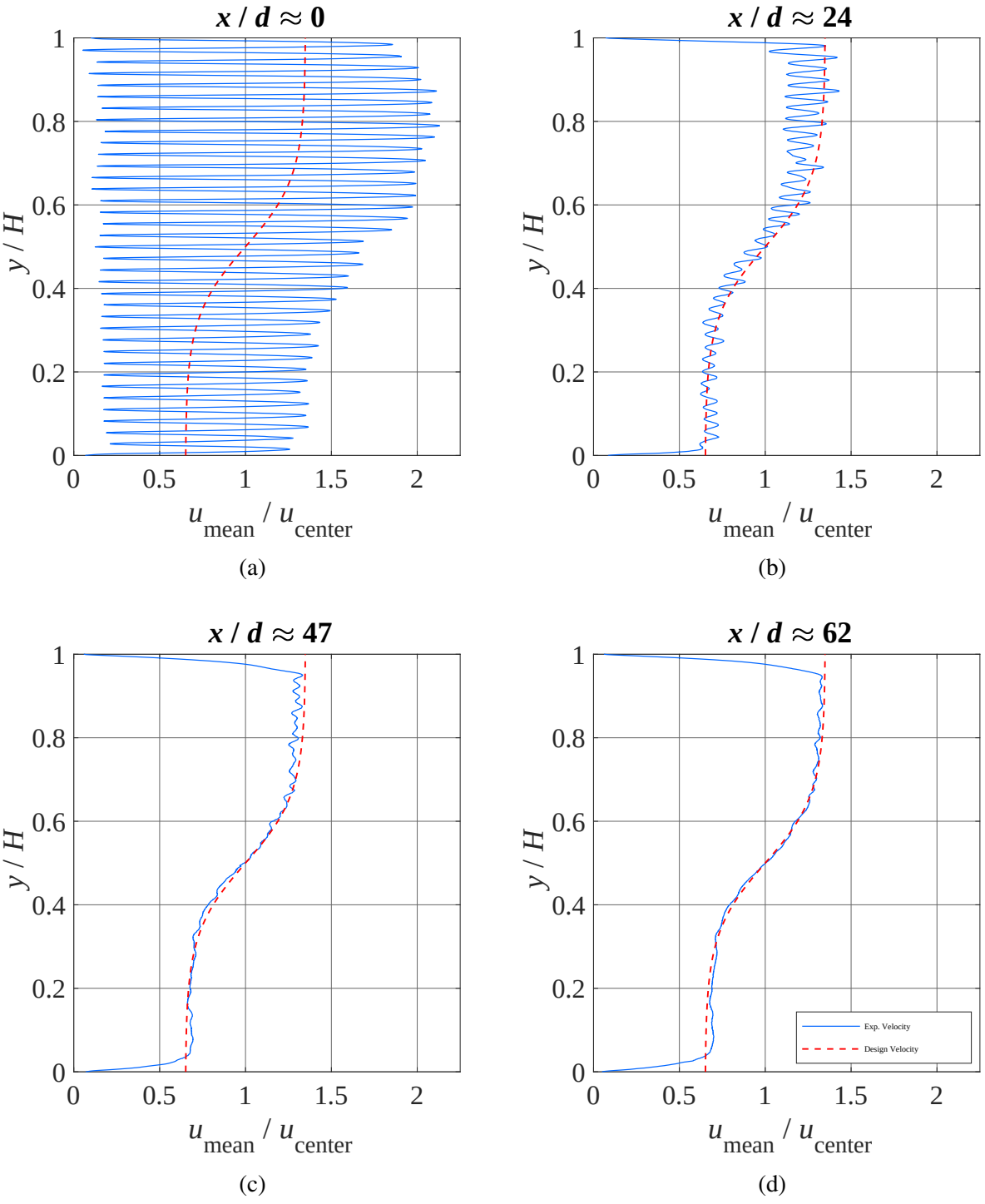

Figure A.7: Normalized velocity profiles showing development of the flow downstream of the honeycomb compared with the design velocity profile.

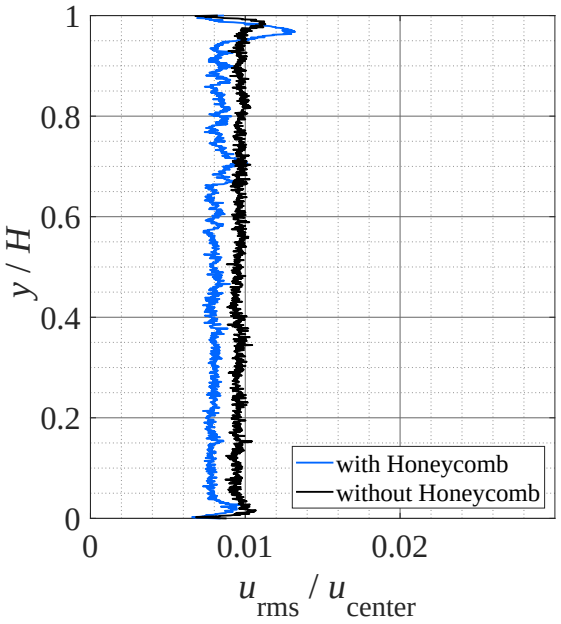

Figure A.8: Temporal velocity fluctuations of the generated hyperbolic tangent profile compared with that of the free stream flow without the shear generation device at a downstream location of $x/d \approx 62$.

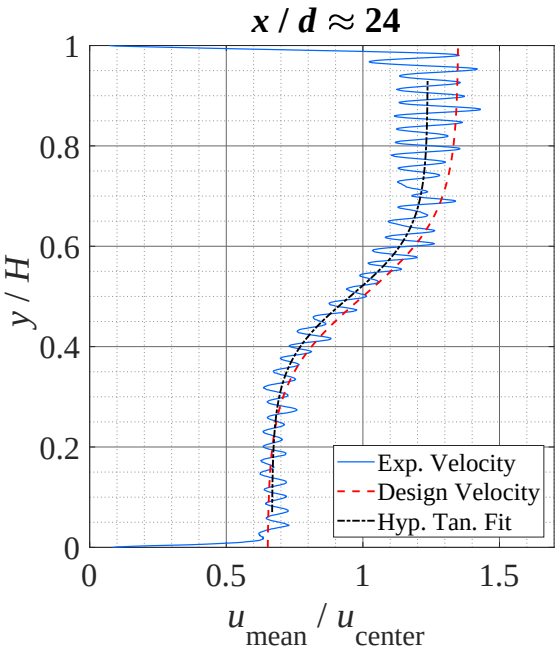

Figure A.9: A hyperbolic tangent curve fitted to the experimental velocity profile at a downstream location of $x/d \approx 24$.

is evident by considering the velocity profile in Figure A.9 for $\frac{x}{d} \approx 24$, where the flow has not developed into its final profile yet, but is still represented well by a hyperbolic tangent curve. The development of these spatial deviations between the mean velocity profile and a hyperbolic tangent fit to the data, is shown as a function of the distance downstream of the honeycomb exit in Figure A.10. After a distance of roughly 60 honeycomb tube diameters, spatial deviations from a smooth hyperbolic tangent profile fall within 1% of the centerline velocity.

The flexibility of the model is demonstrated with the fabrication of a second device to generate a more complicated velocity profile, modeled to mimic the streamwise velocity component of a Gaussian vortex convecting in a uniform flow. Figures A.11 and A.12 present the designed honeycomb length distribution profile and an image of the final honeycomb device, respectively.

A comparison between the design velocity profile and the experimental measurements at a downstream location of $x/d \approx 72$ is shown in Figure A.13. Overall, consistent with the pre-

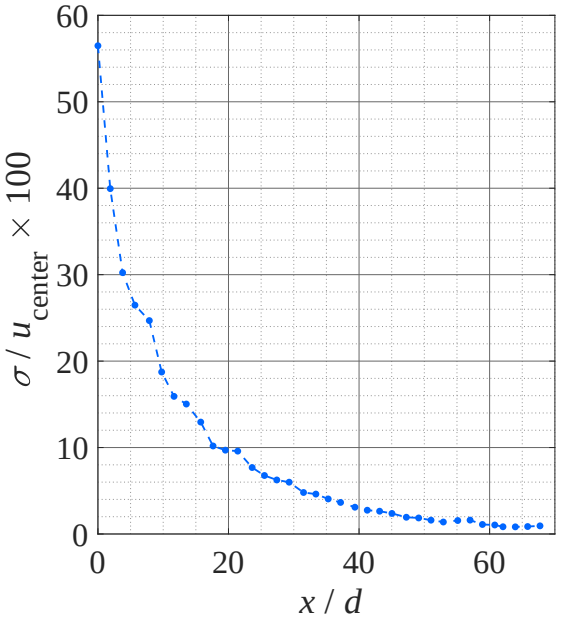

Figure A.10: Development of spatial deviation of the measured velocity profile form the hyperbolic tangent fit as a function of distance downstream.

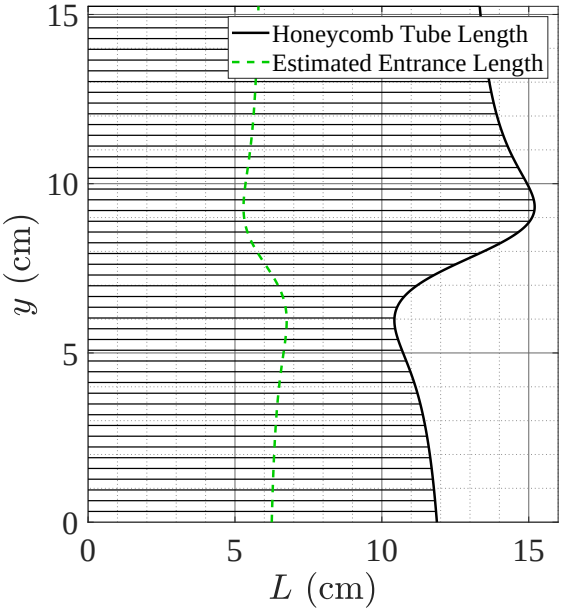

Figure A.11: Calculated honeycomb length distribution for the streamwise velocity component of a convecting Gaussian vortex profile based on the present model compared to the estimated entrance length of the flow at each y (based on $L_e \approx 0.06Re(y)$). The horizontal lines depict the approximate diameter of honeycomb tubes.

vious hyperbolic tangent device, very good agreement between the design velocity profile and experimentally generated velocity profile is observed. Another example of a non-uniform flow generated using this modified model is presented in Hammer et al. (2019), where they studied a harmonically-pitching airfoil in a uniform-shear approach flow.

In addition to the described honeycomb design method, the procedure presented in this article can also be utilized in a reverse fashion to estimate the expected velocity profile generated by a known honeycomb length profile and operating conditions. This perquisite provides the opportunity to predict the performance of a shear generation honeycomb device in off-design situations like using a different approach velocity or an entirely different fluid.

Figure A.12: Image of the shear generation device cut according to designed length profile based on the present model (shown in Figure A.12).

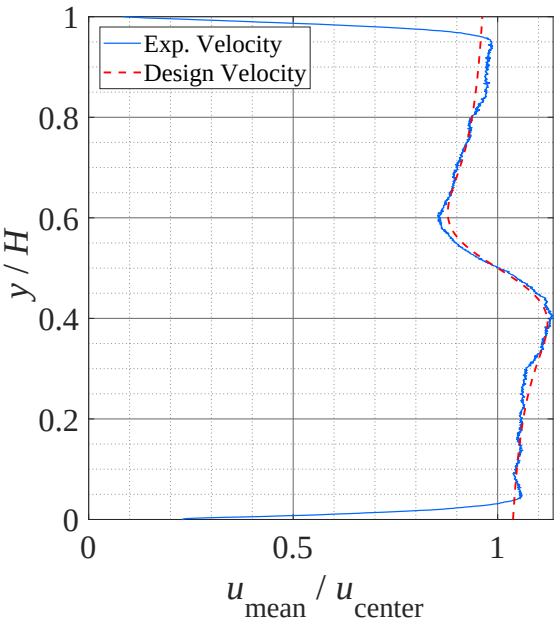

Figure A.13: Normalized experimental velocity of the streamwise component of a convecting Gaussian vortex measured at a downstream location of $x/d \approx 72$ compared to the design velocity profile.

A.4 Comparison with Original Model

A brief comparison of our modified model versus the original model is performed through using a constant friction factor coefficient (equal to the average value estimated by our model) to design another honeycomb to generate the previously described hyperbolic tangent velocity profile. Figure A.14 shows this constant friction factor coefficient honeycomb alongside the earlier design based on our modified model. The assumption of constant friction factor results in a 13% larger variation in tube length across the honeycomb compared to our modified model with a variable friction factor. Varying the value of the constant friction factor coefficient by ±20% changed the tube length difference across the device less than ±2%.

Finally, the resulting velocity profiles from the two different honeycomb designs are evaluated against the experimental results by using our method in reverse (i.e. given a certain honeycomb length distribution to compute the resulting velocity profile). The device was evaluated at the operating conditions similar to the experiment. As exhibited in Figure A.15, the constant friction

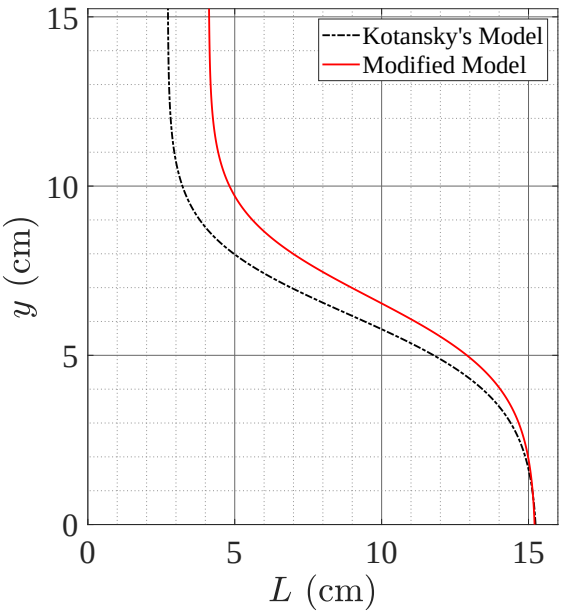

Figure A.14: Comparison of the shape of the honeycomb devices designed using Kotansky's and the modified model to generate the hyperbolic tangent velocity profile shown in Figure 2 A.2).

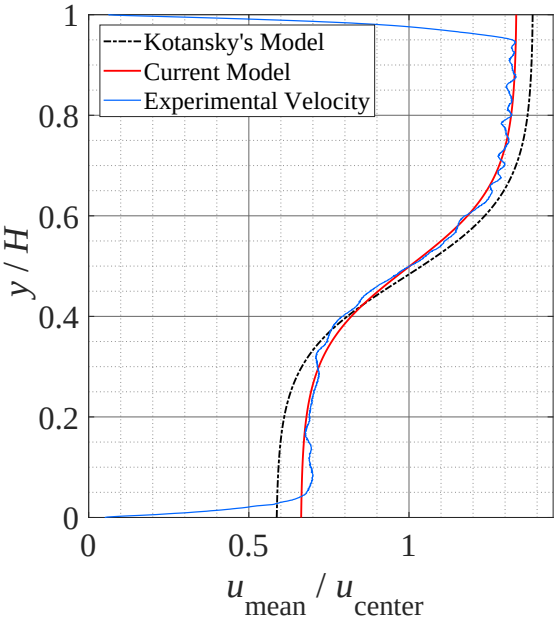

Figure A.15: Estimated velocity profile from Kotansky's honeycomb design compared to that of the modified model and the experimental velocity profile.

factor honeycomb would produce a velocity difference that is 20% larger than desired.

A.5 Discussion

The improvements presented in this study to Kotansky's original variable length honeycomb model enhance the accuracy and tractability of the technique. There are, however, a few key limitations observed that are prudent to discuss. The most important point to keep in mind is the fact that the variable friction factor coefficient model used in this work is based on the assumption of laminar flow in honeycomb tubes. One way to side-step this issue for high speed applications can be through employing honeycombs with small enough tube diameter to satisfy the laminar flow condition inside the tubes. Regarding the fabrication of the device, care should be taken to use a method that produces a clean-cut surface without damaging the honeycomb tubes, while providing sufficient maneuverability. Specialized band saw blades used in this work satisfied these conditions for the desired shape profiles, but for more complicated geometries involving higher

curvatures, we suggest using a water-jet cutting technique instead. When used in water tunnel facilities, it is critical to thoroughly remove all the bubbles trapped inside the honeycomb tubes, as these bubbles would significantly affect the pressure drop distribution across the honeycomb and alter the resulting velocity profile.

APPENDIX B

EFFECT OF AIRFOIL PRESENCE ON UPSTREAM FLOW BOUNDARY CONDITION

Figures presented in this appendix demonstrate the effects of presence of a stationary or pitching airfoil on the upstream shear flow conditions. These plots are based on single component velocimetry measurements performed 2 chord lengths upstream of the airfoil. Raw and normalized mean and fluctuating velocity profiles are presented to highlight the effects of airfoil on the upstream flow. In the case of stationary airfoils, the magnitude of high speed and low speed velocities, as well as centerline location shear layer thickness are also reported as a function of airfoil angle of attack, α.

B.1 Effect of Stationary Airfoil on Upstream Steady Shear Layer

It is observed that while the normalized behavior of the steady shear layer does not change with airfoil angle of attack, the shear layer center position moves slightly towards the hight speed side with positive angles of attack and towards the low speed side with negative angles of attack. This is consistent with trailing edge of the airfoil blocking path of the shear layer at large angles of attack. For example, when the airfoil is places at a positive angle of attack, the trailing edge extends in the path of the low speed side, resulting in a decrees in the low speed side velocity. This in turn, shifts the shear layer towards the high speed side. The thickness of the shear layer does not seem to be affected by the angle of the stationary airfoil.

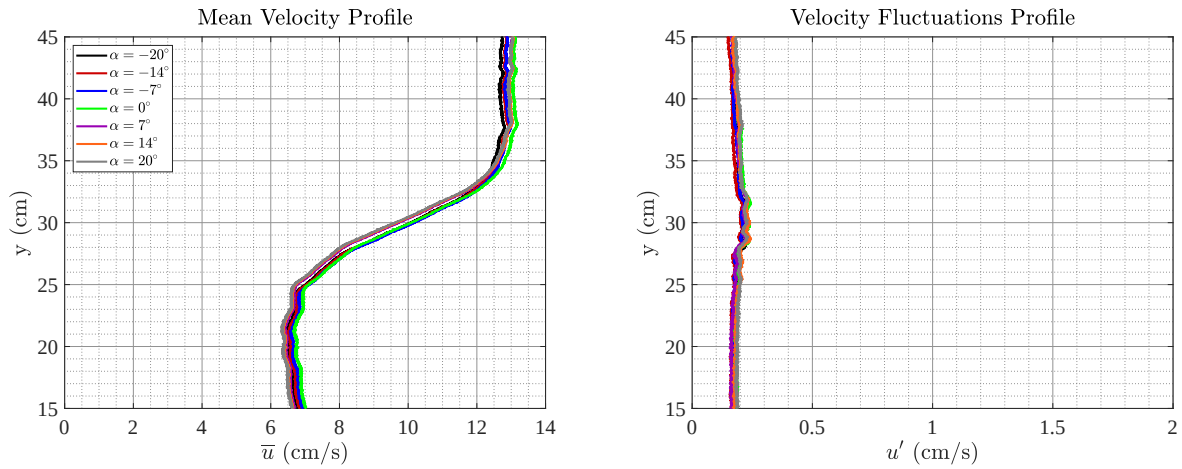

(a) (b)

Figure B.1: Effect of stationary airfoil angle on raw streamwise **(a)** mean and **(b)** fluctuating velocity profiles in the steady shear layer.

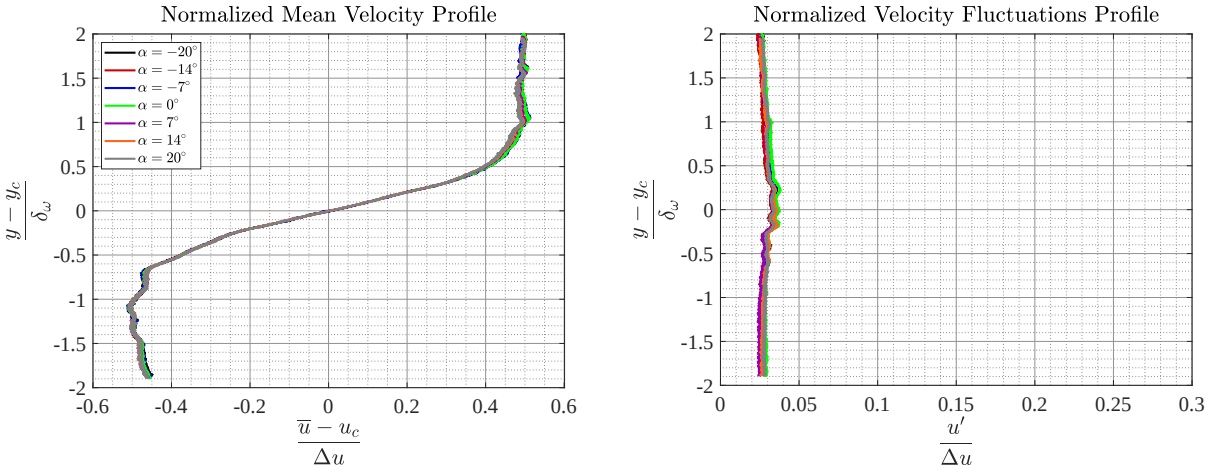

(a) (b)

Figure B.2: Effect of stationary airfoil angle on normalized streamwise **(a)** mean and **(b)** fluctuating velocity profiles in the steady shear layer.

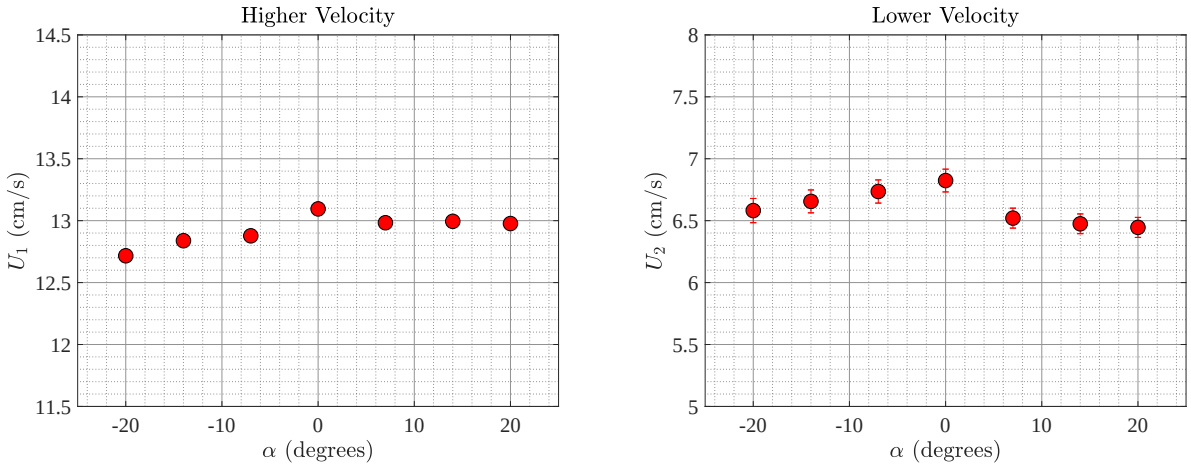

(a) (b)

Figure B.3: Effect of stationary airfoil angle on streamwise **(a)** high-speed and **(b)** low-speed velocities in the steady shear layer.

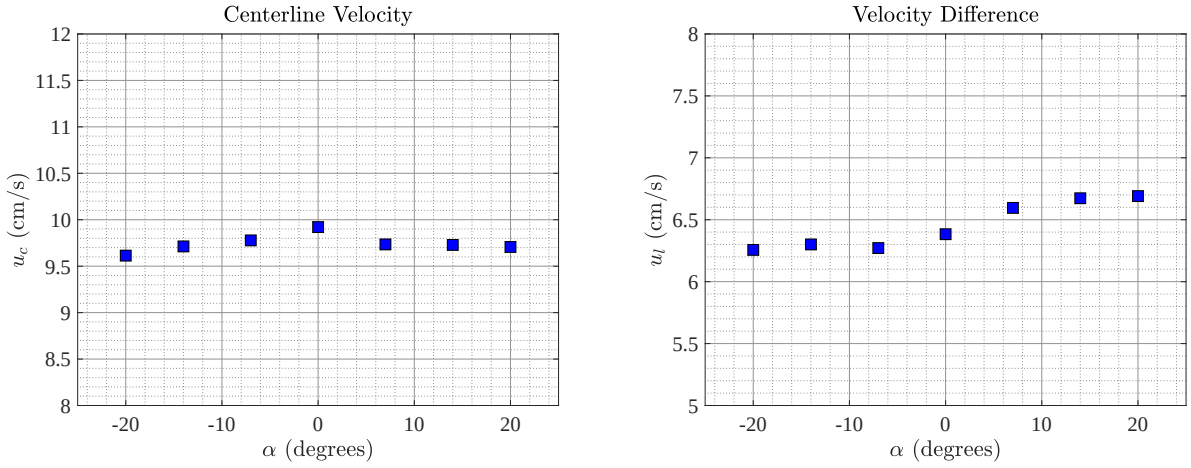

(a) (b)

Figure B.4: Effect of stationary airfoil angle on streamwise **(a)** centerline velocity and **(b)** velocity difference in the steady shear layer.

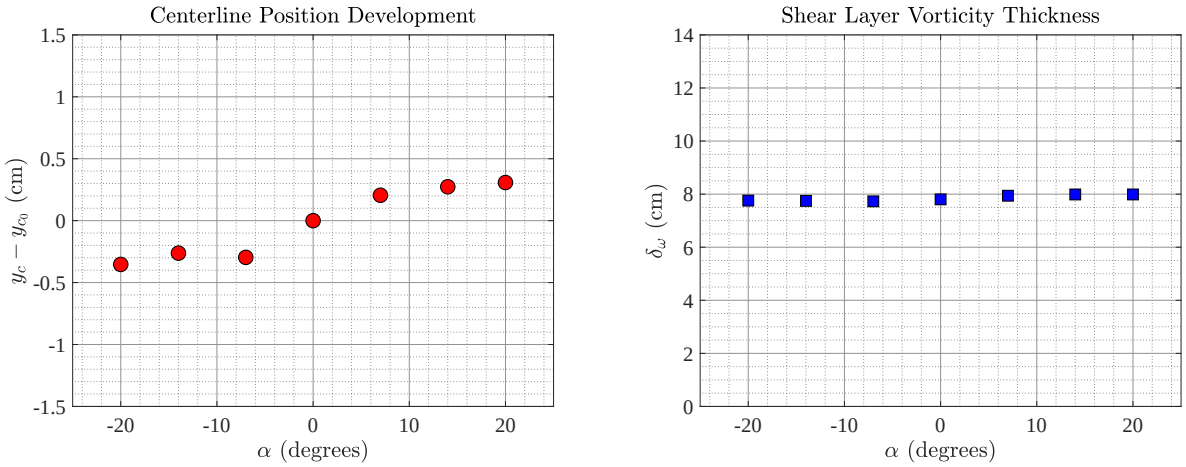

(a) (b)

Figure B.5: Effect of stationary airfoil angle on streamwise **(a)** centerline position and **(b)** vorticity thickness in the steady shear layer.

B.2 Effect of Stationary Airfoil on Upstream Unsteady Shear Layer

Similar to the observations in the steady shear layer, while the normalized behavior of the steady shear layer does not change with airfoil angle of attack, the shear layer center position moves slightly towards the hight speed side with positive angles of attack and towards the low speed side with negative angles of attack. This is consistent with trailing edge of the airfoil blocking path of the shear layer at large angles of attack. For example, when the airfoil is places at a positive angle of attack, the trailing edge extends in the path of the low speed side, resulting in a decrees in the low speed side velocity. This in turn, shifts the shear layer towards the high speed side. The thickness of the shear layer does not seem to be affected by the angle of the stationary airfoil.

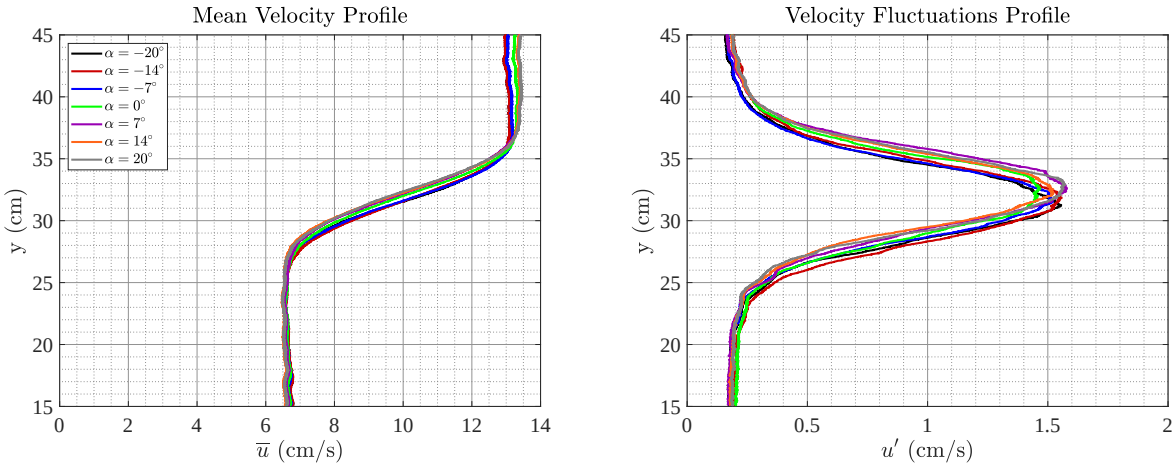

(a) (b)

Figure B.6: Effect of stationary airfoil angle on raw streamwise **(a)** mean and **(b)** fluctuating velocity profiles in the unsteady shear layer.

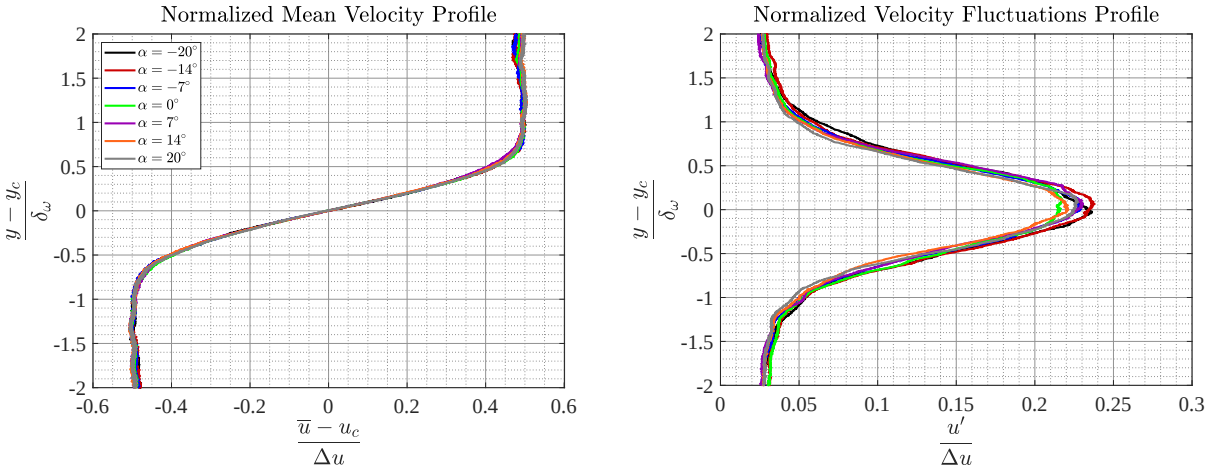

(a) (b)

Figure B.7: Effect of stationary airfoil angle on normalized streamwise **(a)** mean and **(b)** fluctuating velocity profiles in the unsteady shear layer.

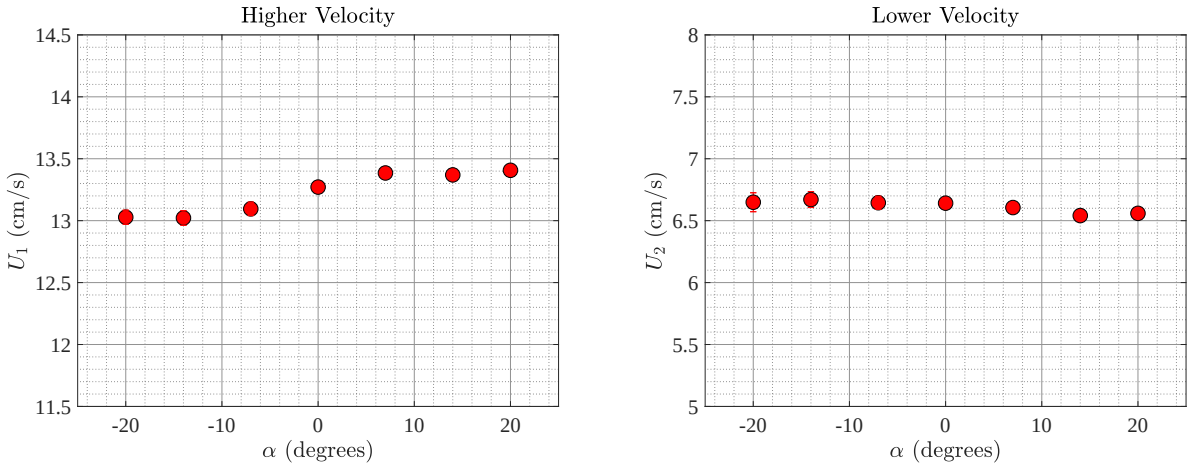

(a) (b)

Figure B.8: Effect of stationary airfoil angle on streamwise **(a)** high-speed and **(b)** low-speed velocities in the unsteady shear layer.

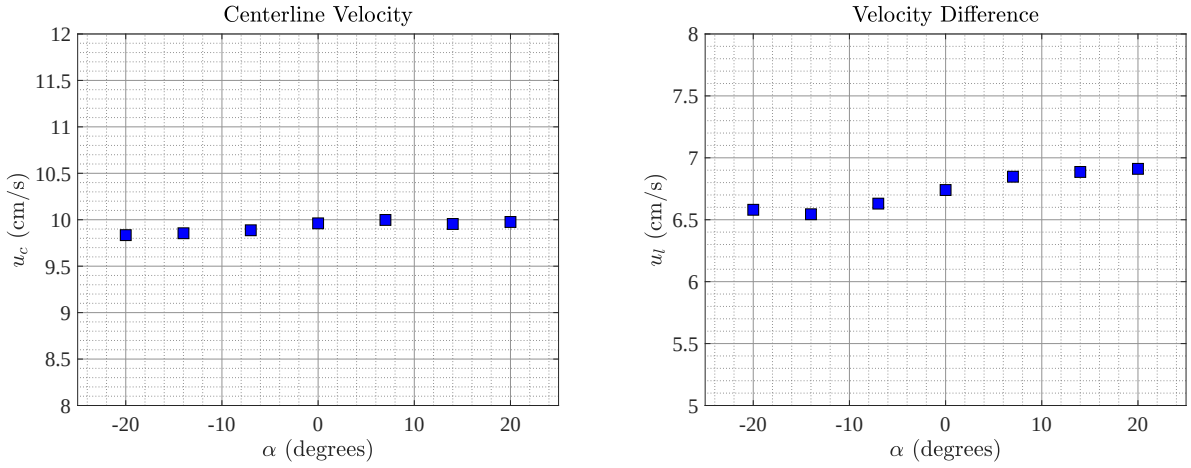

(a) (b)

Figure B.9: Effect of stationary airfoil angle on streamwise **(a)** centerline velocity and **(b)** velocity difference in the unsteady shear layer.

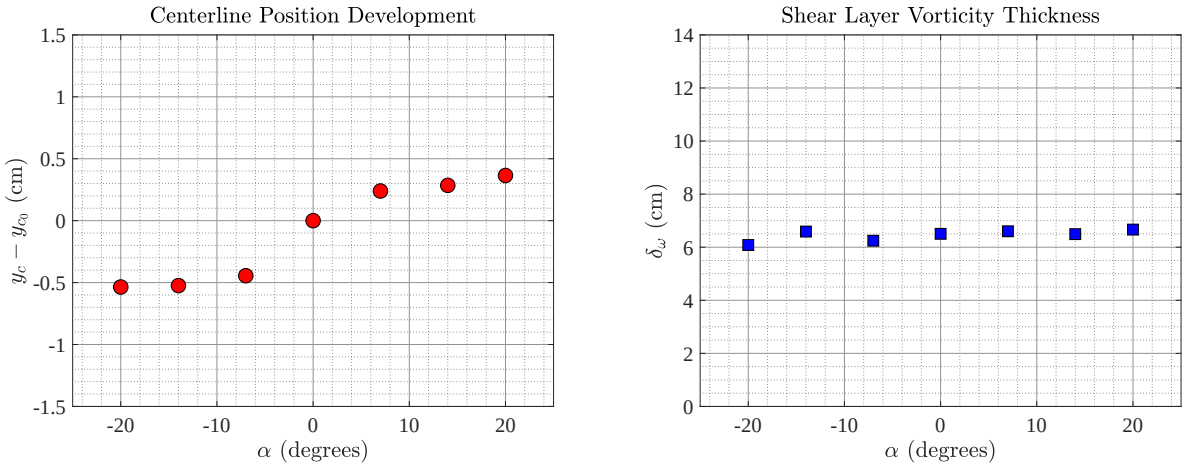

(a) (b)

Figure B.10: Effect of stationary airfoil angle on streamwise **(a)** centerline position and **(b)** vorticity thickness in the unsteady shear layer.

B.3 Effect of Pitching Airfoil on Upstream Unsteady Shear Layer with $\frac{\delta_\omega}{c} = 0.5$

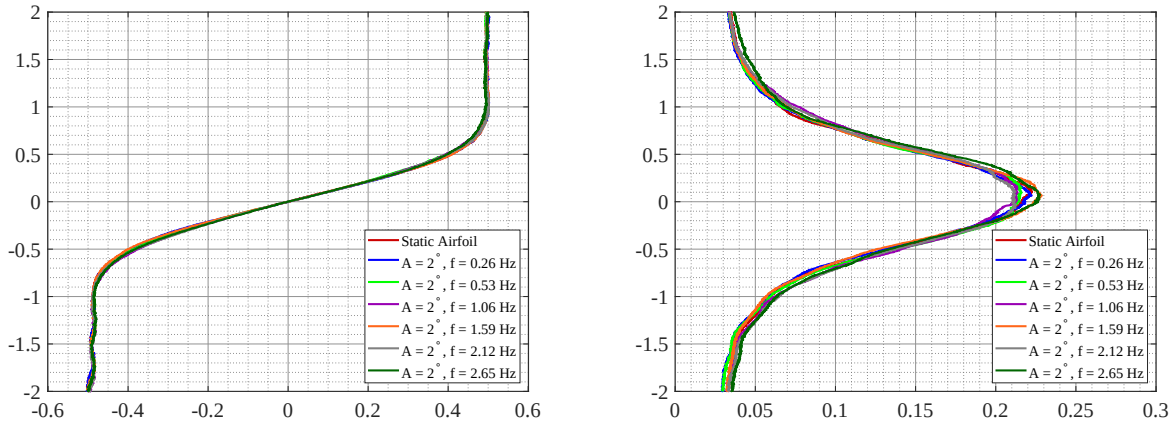

(a) (b)

Figure B.11: Effect of pitching airfoil angle on normalized streamwise **(a)** mean and **(b)** fluctuating velocity profiles in the unsteady shear layer with $\frac{\delta_\omega}{c} = 0.5$ and $K_{\max} = 1.4$.

B.4 Effect of Pitching Airfoil on Upstream Unsteady Shear Layer with $\frac{\delta_\omega}{c} = 0.9$

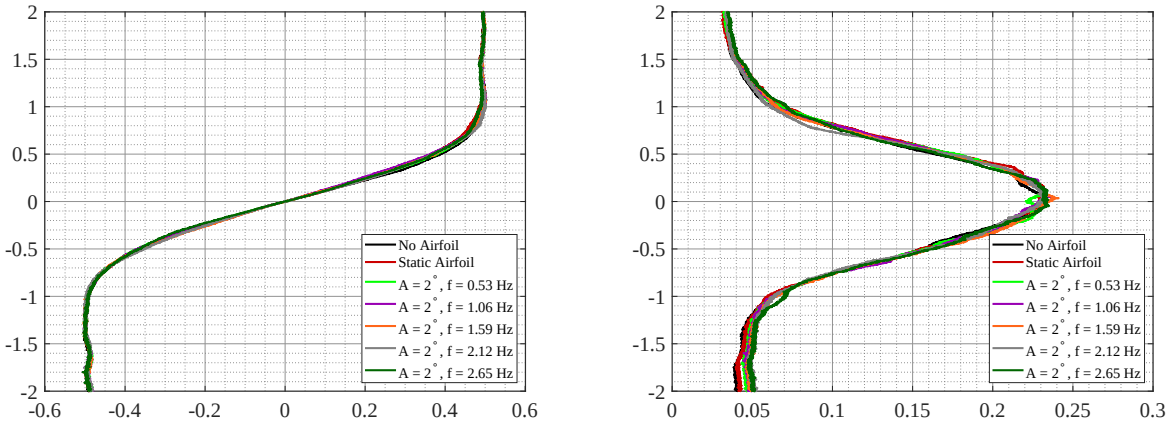

(a) (b)

Figure B.12: Effect of pitching airfoil angle on normalized streamwise **(a)** mean and **(b)** fluctuating velocity profiles in the unsteady shear layer with $\frac{\delta_\omega}{c} = 0.9$ and $K_{\max} = 0.8$.

APPENDIX C

AERODYNAMIC FORCES ON OSCILLATING AIRFOIL WITH $\alpha_0 = 4^\circ$

Figures presented in this appendix demonstrate the aerodynamic performance of a NACA0012 airfoil sinusoidally pitching around its quarter chord with an oscillation amplitude of $\alpha_0 = 4^\circ$ in various flow conditions considered in this work. In all of these figures the symbols depict the average value of 4 independent measurement repetitions for each combination of flow and oscillation frequency. The error bars for mean values are based on the propagation of sensor drift during each measurement, while the uncertainty in fluctuations is shown as the standard deviation of the fluctuation magnitudes between the 4 repetitions.

C.1 Effect of Shear Flow Unsteadiness

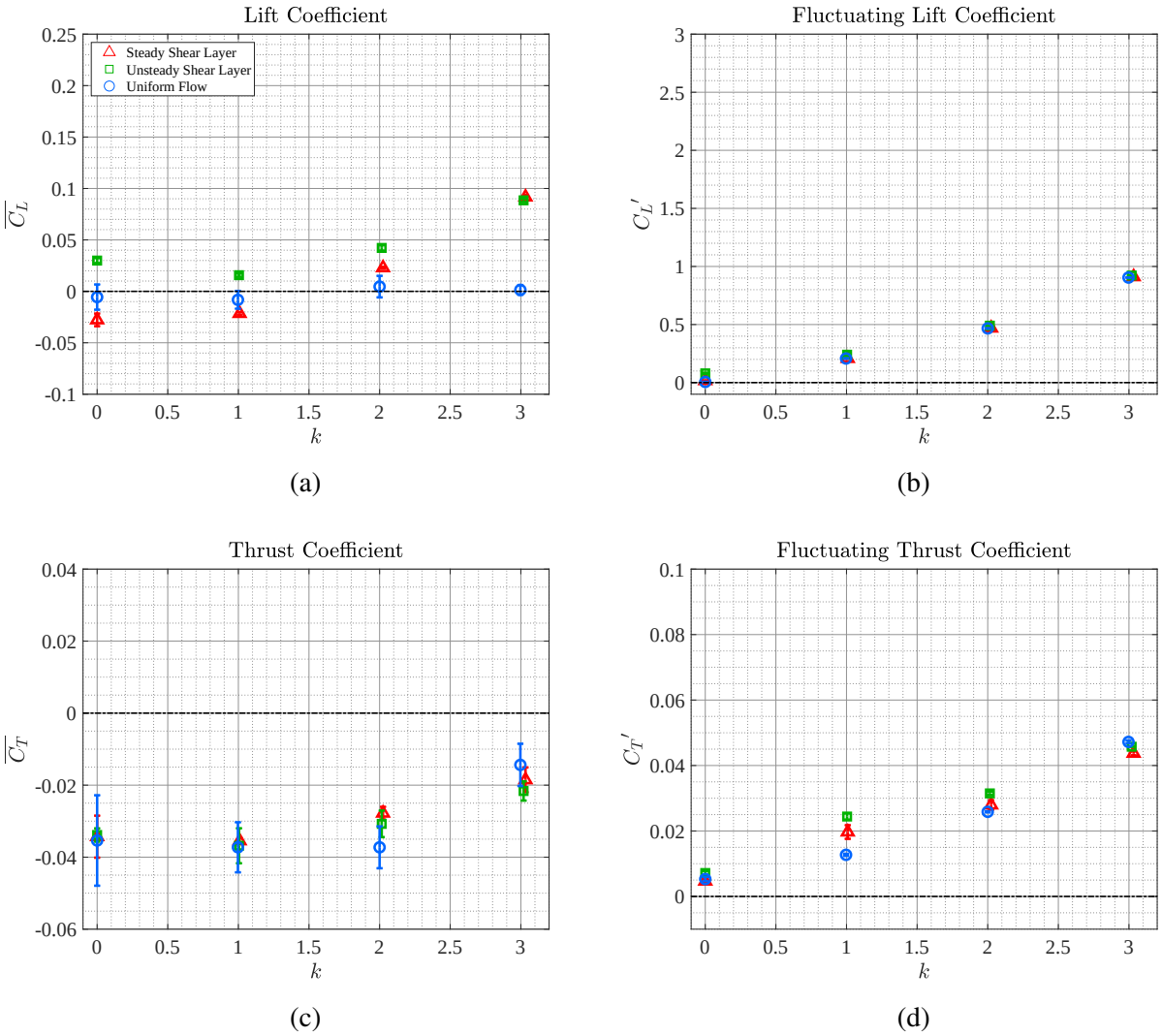

Figure C.1: Comparison of aerodynamic force coefficients measured on a pitching airfoil placed in uniform, steady shear and unsteady shear flows: **(a)** mean lift coefficient, $\overline{C_L}$, **(b)** lift coefficient fluctuations, $C_L{}'$, **(c)** mean thrust coefficient, $\overline{C_T}$, **(d)** thrust coefficient fluctuations, $C_T{}'$. The airfoil is pitching with zero mean angle of attack and an oscillation amplitude of 4° around its quarter chord point.

C.2 Effect of Unsteady Shear Flow Thickness and Shear Rate

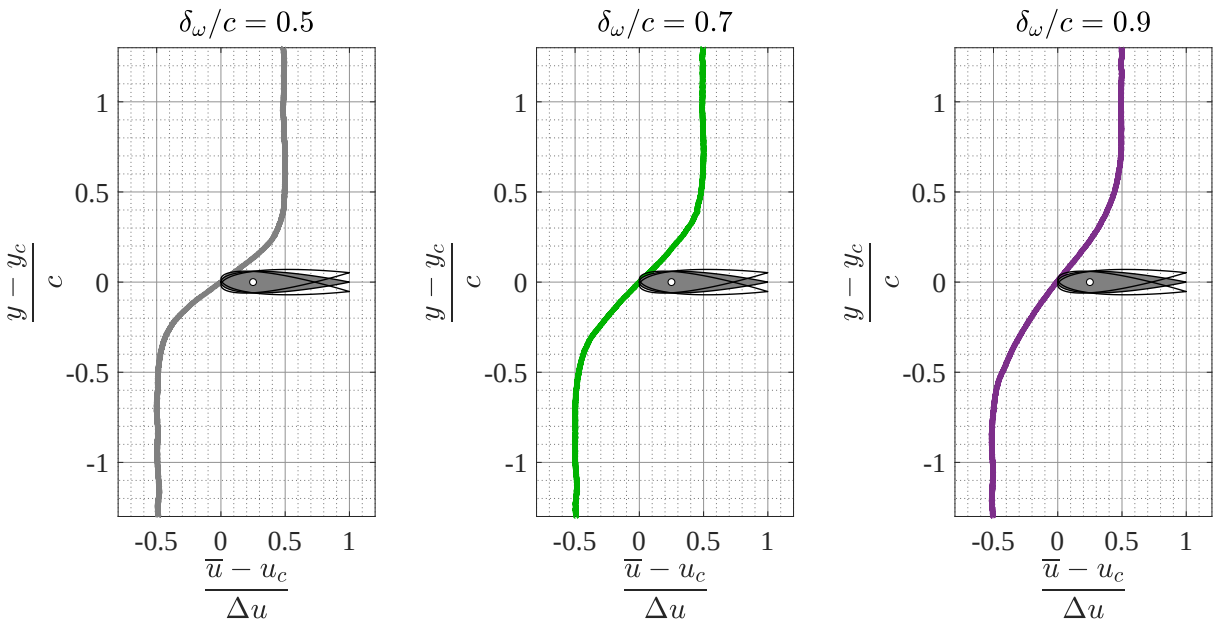

(a) (b) (c)

Figure C.2: Extent of airfoil angular displacement (±4°) compared to the shear layer thickness at each measurement location.

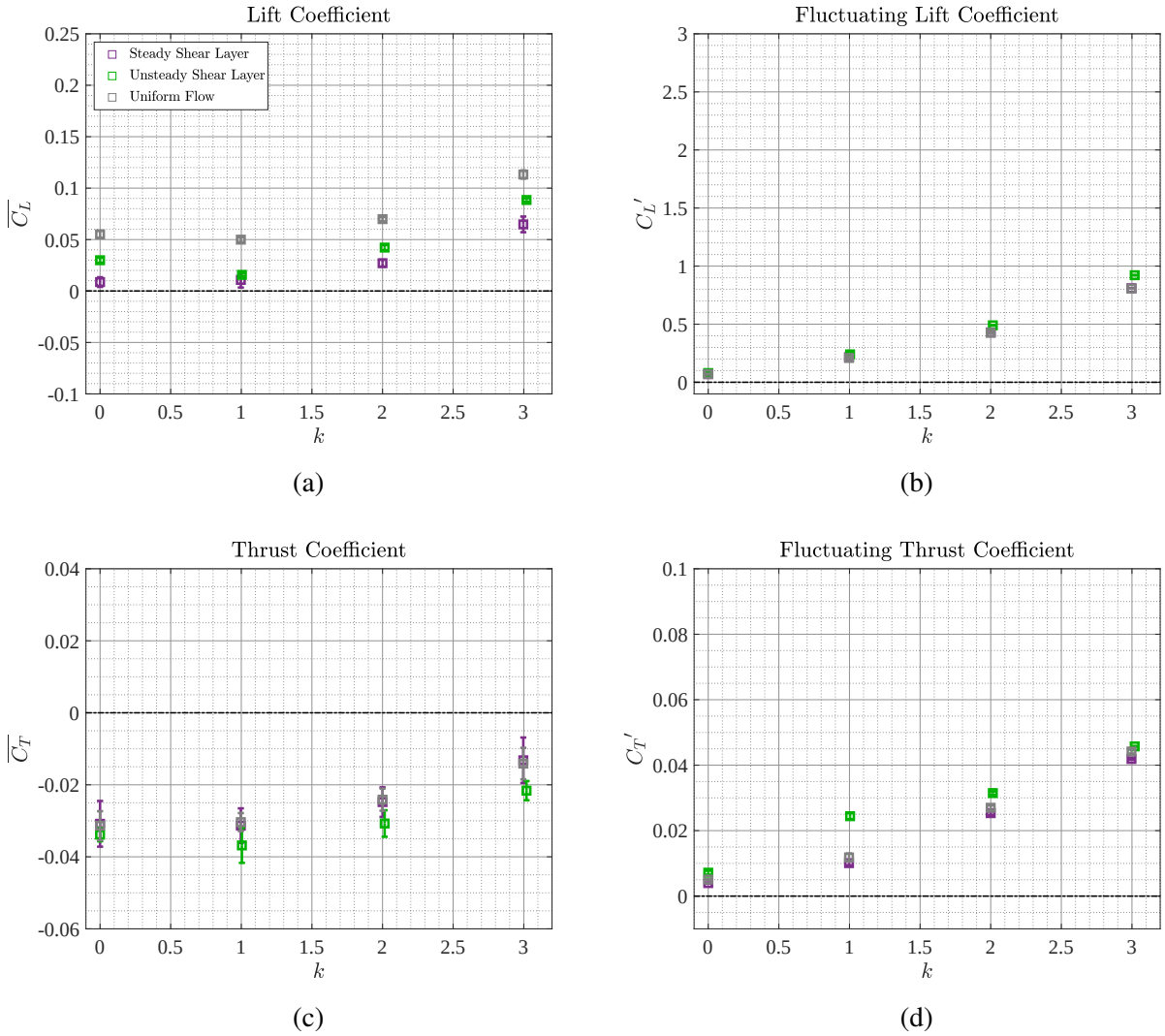

Figure C.3: Comparison of aerodynamic force coefficients measured on a pitching airfoil placed in unsteady shear layer at different downstream locations: **(a)** mean lift coefficient, $\overline{C_L}$, **(b)** lift coefficient fluctuations, $C_L{}'$, **(c)** mean thrust coefficient, $\overline{C_T}$, **(d)** thrust coefficient fluctuations, $C_T{}'$. The airfoil is pitching with zero mean angle of attack and an oscillation amplitude of 4° around its quarter chord point.

APPENDIX D

SAMPLES OF PHASE ORDERED AERODYNAMIC FORCES ON OSCILLATING AIRFOIL

The following figures provide one sample of the phase ordered and phase averaged lift and thrust coefficients for each of the oscillation cases performed in uniform flow, steady shear layer and unsteady shear layer. In these experiments the airfoil is pitching with a reduced frequency of varying from $k = 1$ to 6 and oscillation amplitudes of $\alpha_0 = 2^\circ$. Each of these plots are from a single instance of force measurement sorted into 128 phase bins based on the airfoil angular position. In these plots, the blue lines represent the phase ordered data, while the black lines portray the phase averaged behavior ($\overline{\langle C_L \rangle}$ and $\overline{\langle C_T \rangle}$) with the red lines highlighting the standard deviation of the data in each phase bin ($\langle C_L \rangle'$ and $\langle C_T \rangle'$).

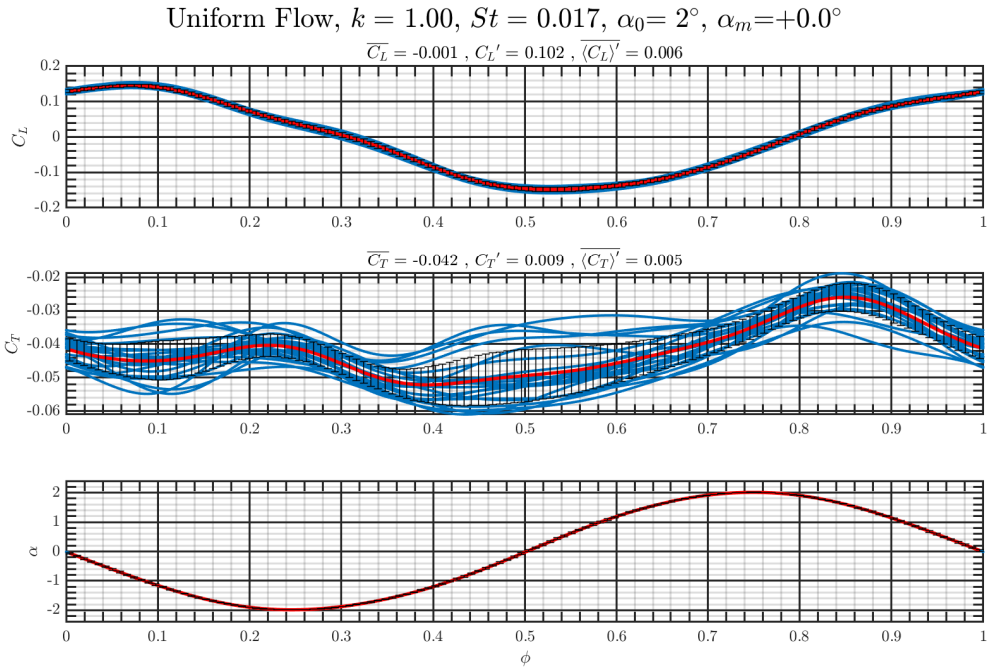

Figure D.1: Sample of phase ordered force measurements performed in uniform flow for a pitching airfoil with oscillation amplitude of $\alpha_0 = 2°$ and reduced frequency of $k = 1$. Blue lines represent the phase ordered data, red lines portray the phase averaged values with the black lines highlighting the standard deviation of the data in each phase bin.

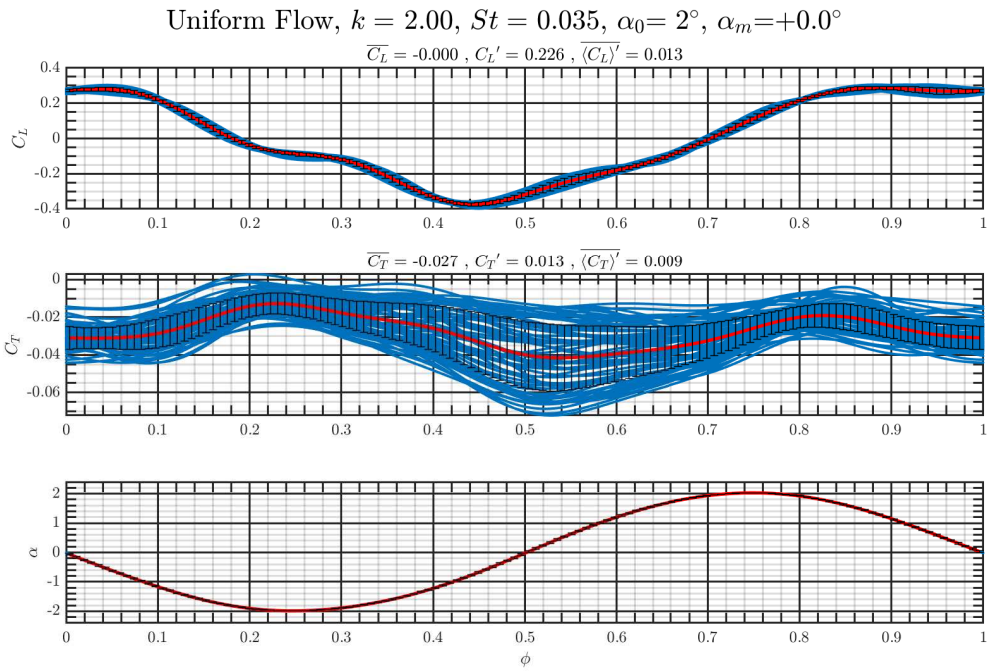

Figure D.2: Sample of phase ordered force measurements performed in uniform flow for a pitching airfoil with oscillation amplitude of $\alpha_0 = 2°$ and reduced frequency of $k = 2$. Blue lines represent the phase ordered data, red lines portray the phase averaged values with the black lines highlighting the standard deviation of the data in each phase bin.

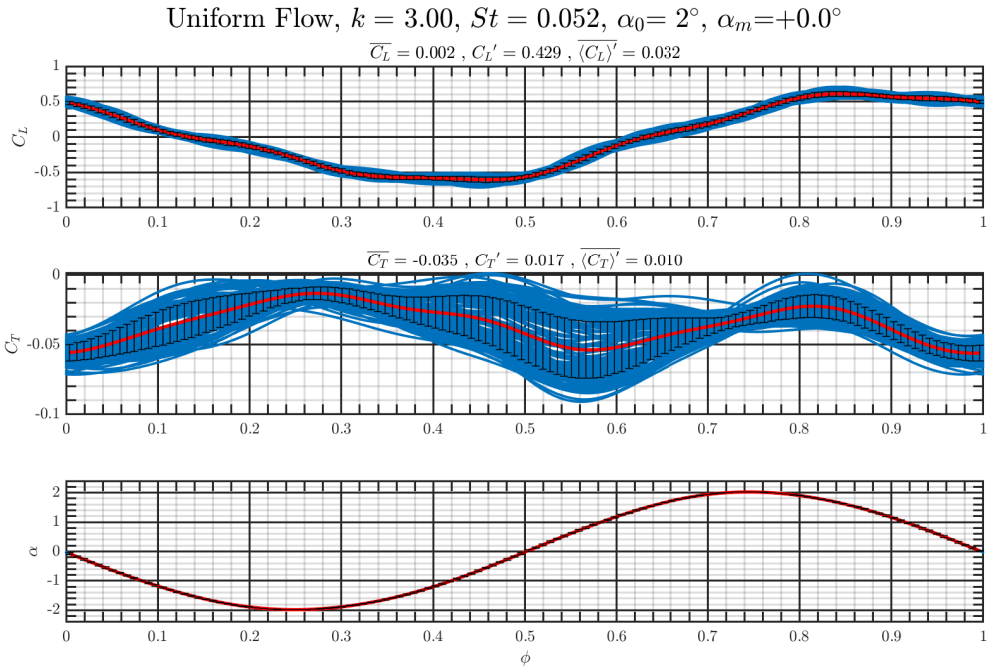

Figure D.3: Sample of phase ordered force measurements performed in uniform flow for a pitching airfoil with oscillation amplitude of $\alpha_0 = 2°$ and reduced frequency of $k = 3$. Blue lines represent the phase ordered data, red lines portray the phase averaged values with the black lines highlighting the standard deviation of the data in each phase bin.

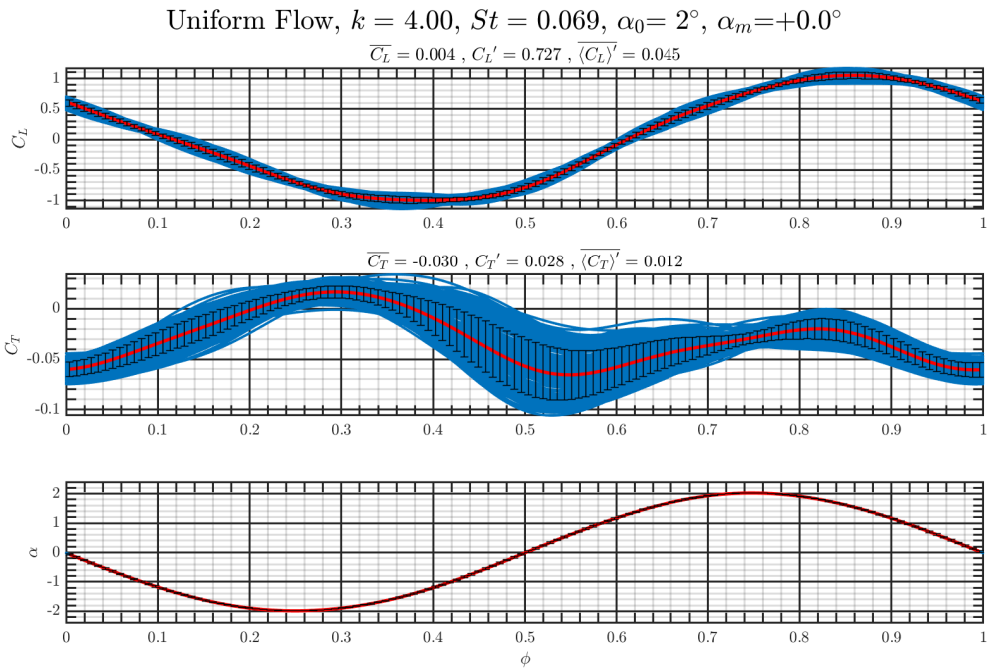

Figure D.4: Sample of phase ordered force measurements performed in uniform flow for a pitching airfoil with oscillation amplitude of $\alpha_0 = 2°$ and reduced frequency of $k = 4$. Blue lines represent the phase ordered data, red lines portray the phase averaged values with the black lines highlighting the standard deviation of the data in each phase bin.

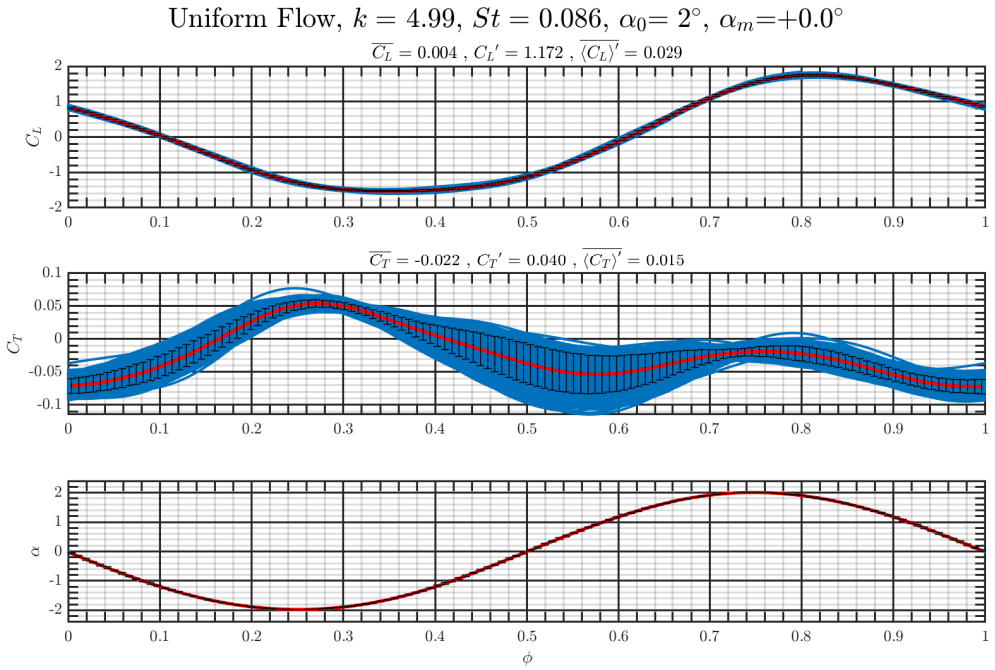

Figure D.5: Sample of phase ordered force measurements performed in uniform flow for a pitching airfoil with oscillation amplitude of $\alpha_0 = 2°$ and reduced frequency of $k = 5$. Blue lines represent the phase ordered data, red lines portray the phase averaged values with the black lines highlighting the standard deviation of the data in each phase bin.

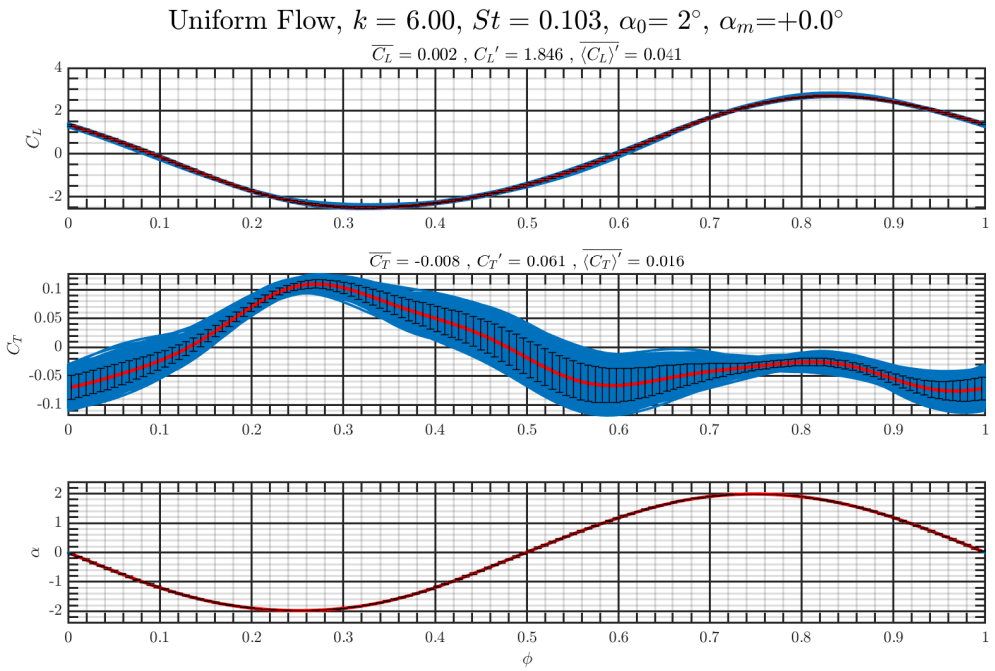

Figure D.6: Sample of phase ordered force measurements performed in uniform flow for a pitching airfoil with oscillation amplitude of $\alpha_0 = 2°$ and reduced frequency of $k = 6$. Blue lines represent the phase ordered data, red lines portray the phase averaged values with the black lines highlighting the standard deviation of the data in each phase bin.

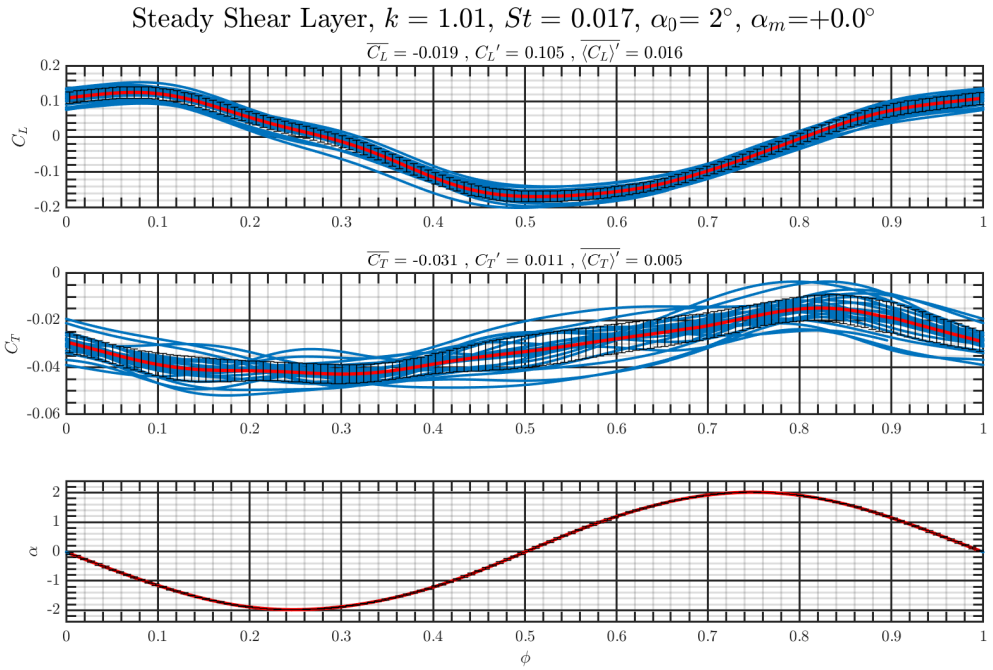

Figure D.7: Sample of phase ordered force measurements performed in steady shear flow for a pitching airfoil with oscillation amplitude of $\alpha_0 = 2°$ and reduced frequency of $k = 1$. Blue lines represent the phase ordered data, red lines portray the phase averaged values with the black lines highlighting the standard deviation of the data in each phase bin.

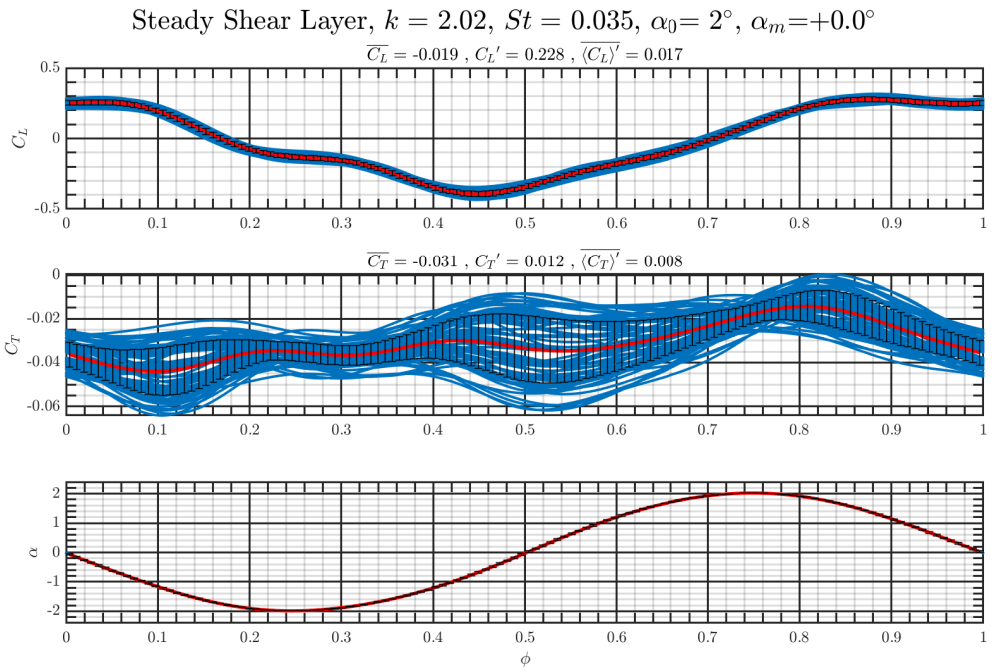

Figure D.8: Sample of phase ordered force measurements performed in steady shear flow for a pitching airfoil with oscillation amplitude of $\alpha_0 = 2°$ and reduced frequency of $k = 2$. Blue lines represent the phase ordered data, red lines portray the phase averaged values with the black lines highlighting the standard deviation of the data in each phase bin.

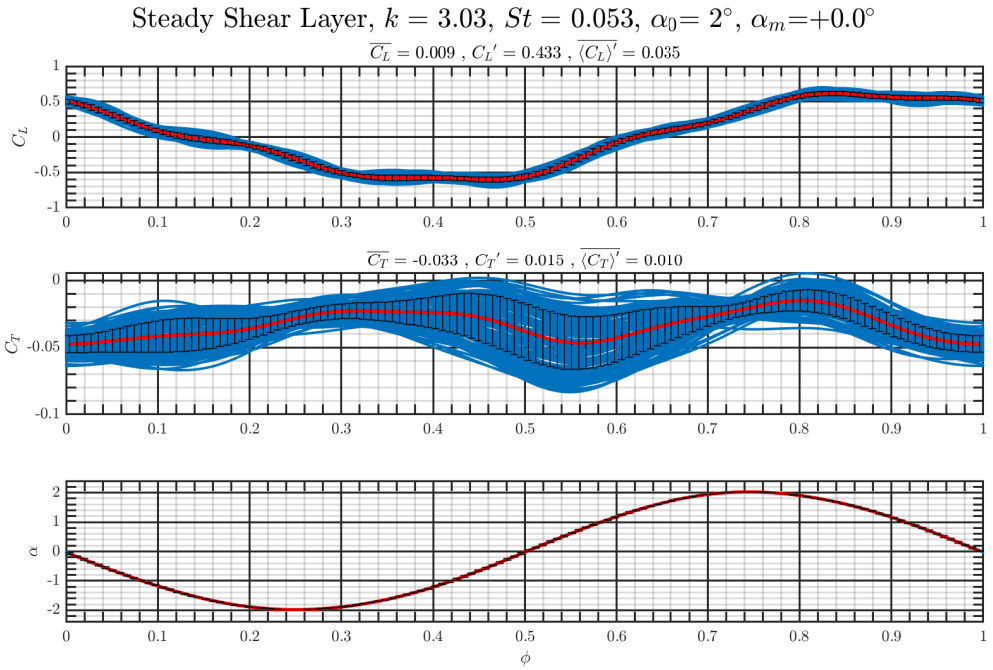

Figure D.9: Sample of phase ordered force measurements performed in steady shear flow for a pitching airfoil with oscillation amplitude of $\alpha_0 = 2°$ and reduced frequency of $k = 3$. Blue lines represent the phase ordered data, red lines portray the phase averaged values with the black lines highlighting the standard deviation of the data in each phase bin.

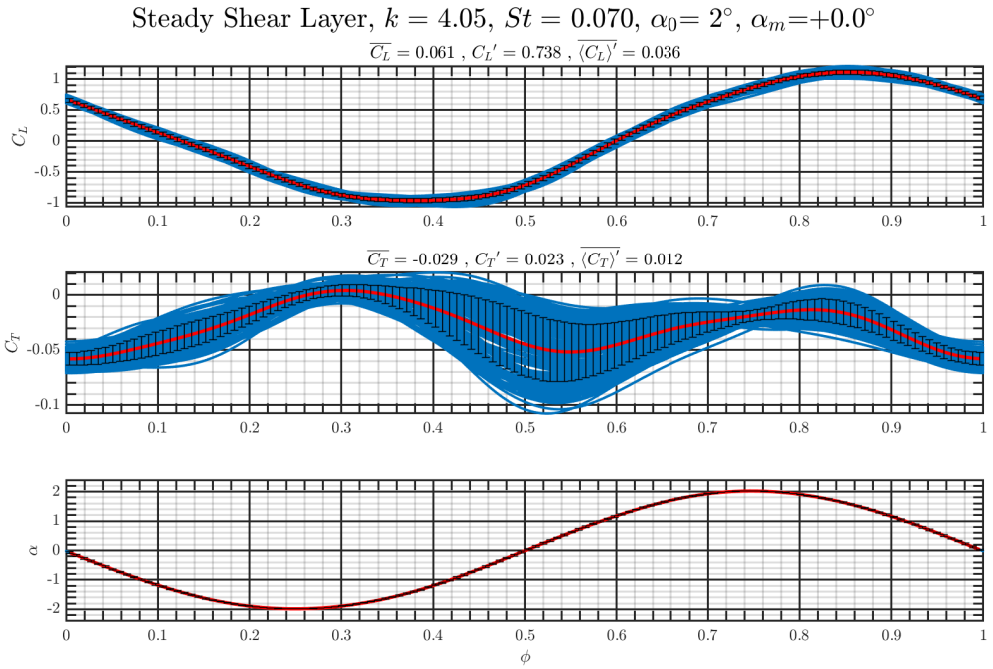

Figure D.10: Sample of phase ordered force measurements performed in steady shear flow for a pitching airfoil with oscillation amplitude of $\alpha_0 = 2°$ and reduced frequency of $k = 4$. Blue lines represent the phase ordered data, red lines portray the phase averaged values with the black lines highlighting the standard deviation of the data in each phase bin.

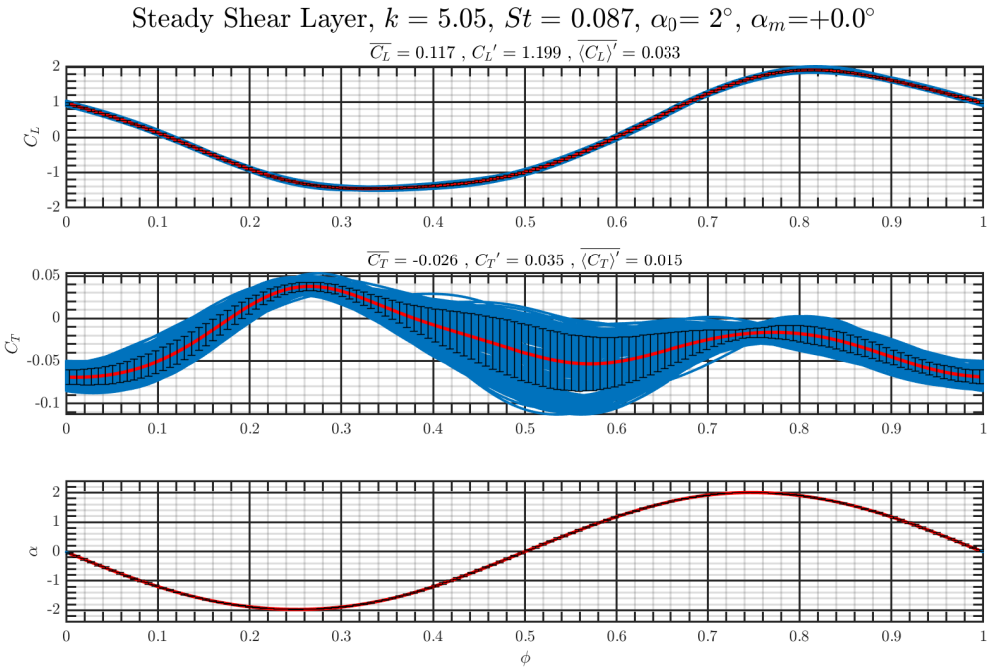

Figure D.11: Sample of phase ordered force measurements performed in steady shear flow for a pitching airfoil with oscillation amplitude of $\alpha_0 = 2°$ and reduced frequency of $k = 5$. Blue lines represent the phase ordered data, red lines portray the phase averaged values with the black lines highlighting the standard deviation of the data in each phase bin.

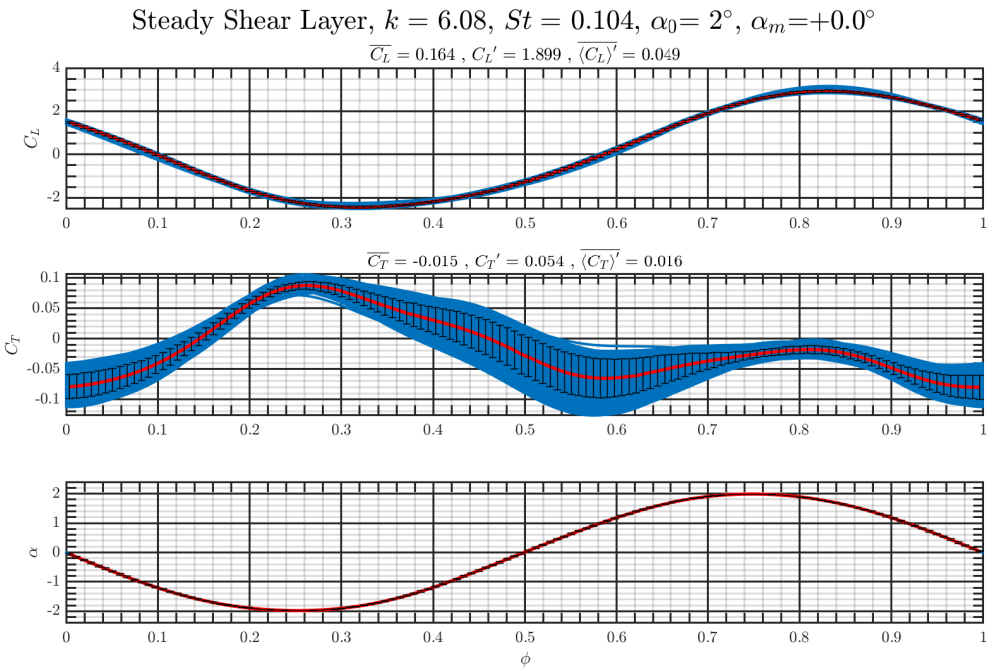

Figure D.12: Sample of phase ordered force measurements performed in steady shear flow for a pitching airfoil with oscillation amplitude of $\alpha_0 = 2°$ and reduced frequency of $k = 6$. Blue lines represent the phase ordered data, red lines portray the phase averaged values with the black lines highlighting the standard deviation of the data in each phase bin.

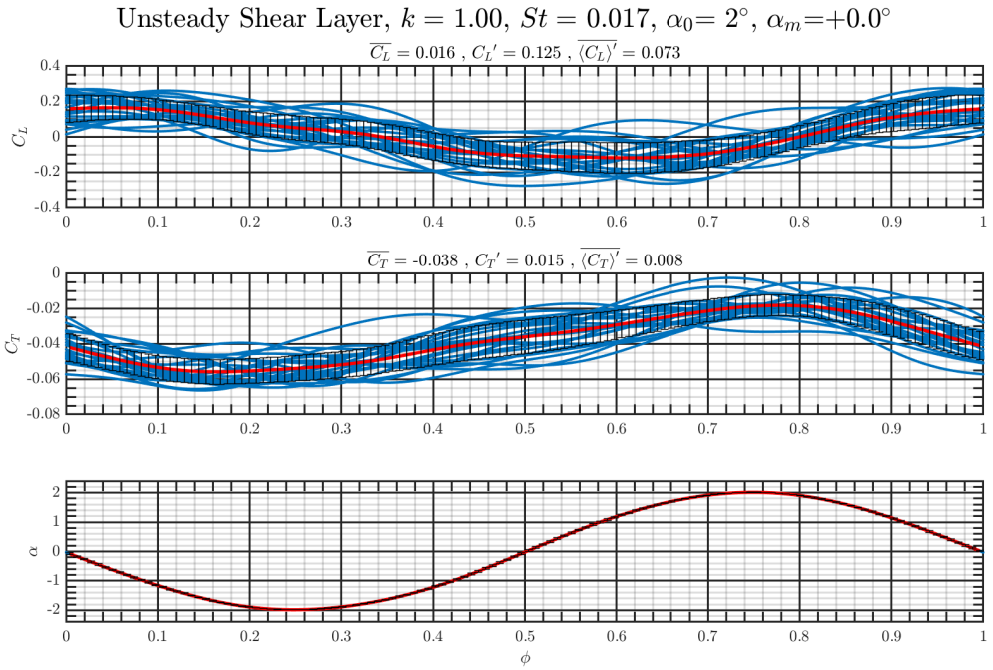

Figure D.13: Sample of phase ordered force measurements performed in unsteady shear flow for a pitching airfoil with oscillation amplitude of $\alpha_0 = 2°$ and reduced frequency of $k = 1$. Blue lines represent the phase ordered data, red lines portray the phase averaged values with the black lines highlighting the standard deviation of the data in each phase bin.

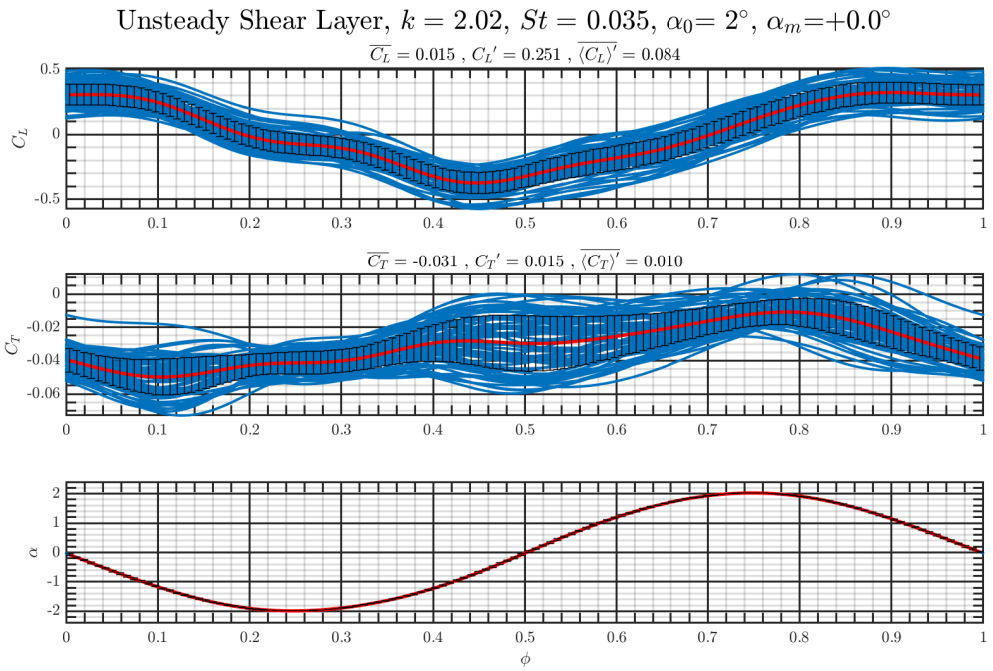

Figure D.14: Sample of phase ordered force measurements performed in unsteady shear flow for a pitching airfoil with oscillation amplitude of $\alpha_0 = 2°$ and reduced frequency of $k = 2$. Blue lines represent the phase ordered data, red lines portray the phase averaged values with the black lines highlighting the standard deviation of the data in each phase bin.

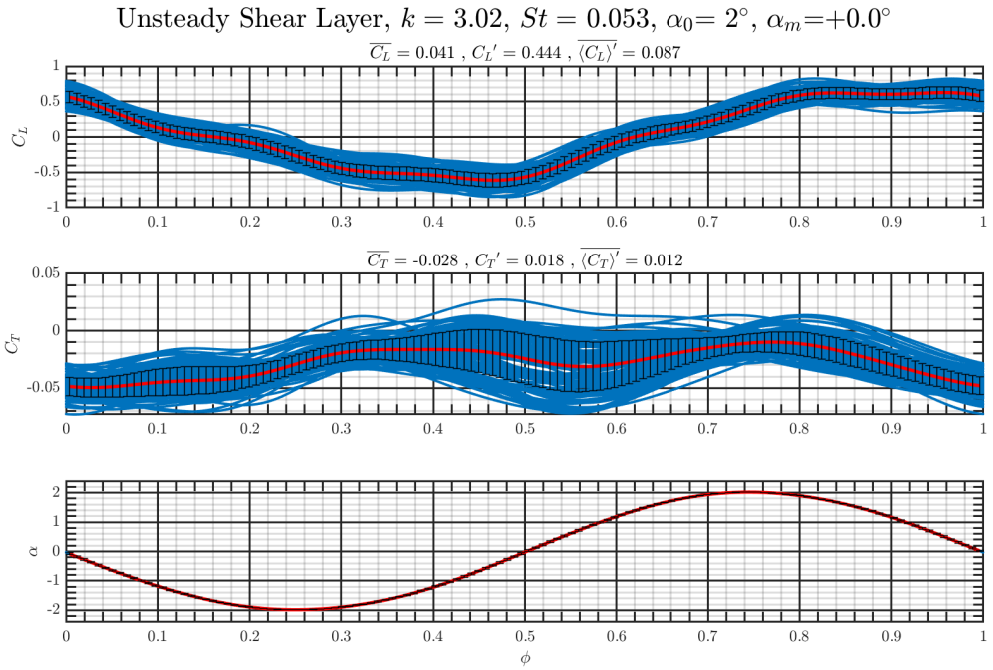

Figure D.15: Sample of phase ordered force measurements performed in unsteady shear flow for a pitching airfoil with oscillation amplitude of $\alpha_0 = 2°$ and reduced frequency of $k = 3$. Blue lines represent the phase ordered data, red lines portray the phase averaged values with the black lines highlighting the standard deviation of the data in each phase bin.

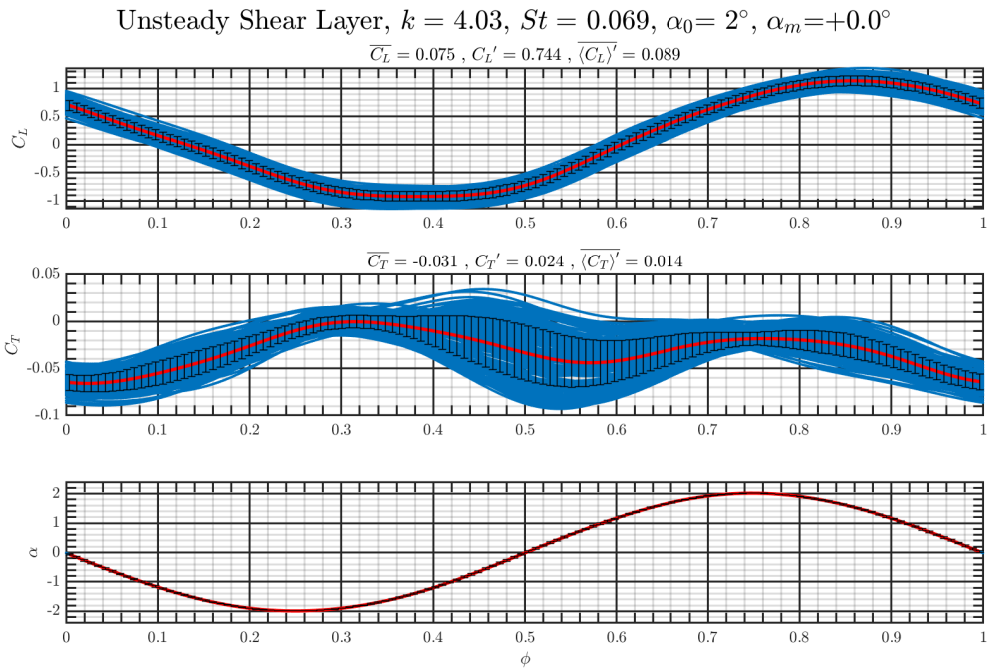

Figure D.16: Sample of phase ordered force measurements performed in unsteady shear flow for a pitching airfoil with oscillation amplitude of $\alpha_0 = 2°$ and reduced frequency of $k = 4$. Blue lines represent the phase ordered data, red lines portray the phase averaged values with the black lines highlighting the standard deviation of the data in each phase bin.

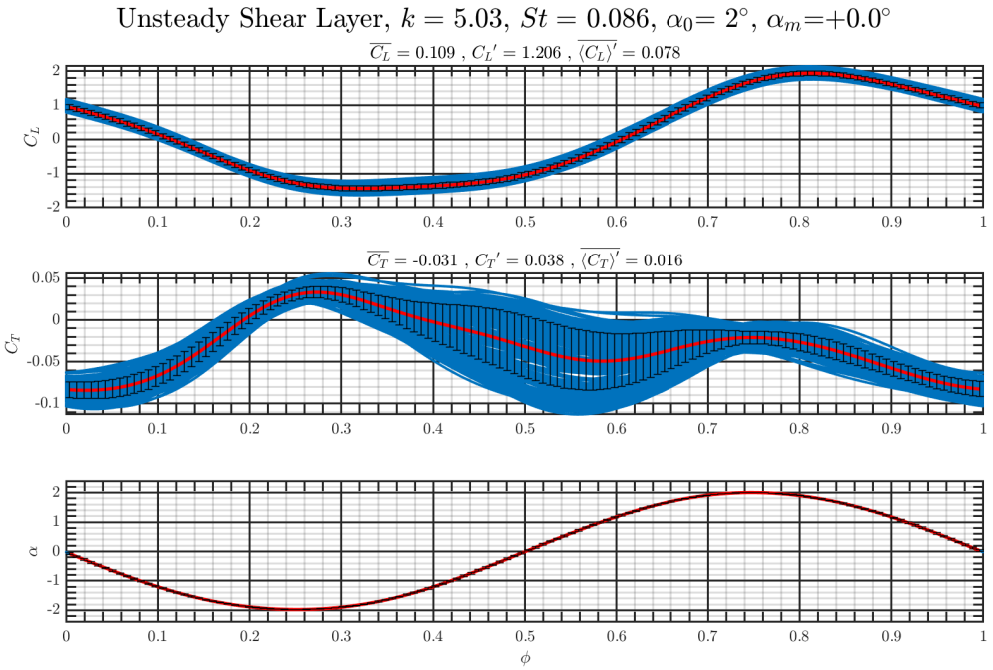

Figure D.17: Sample of phase ordered force measurements performed in unsteady shear flow for a pitching airfoil with oscillation amplitude of $\alpha_0 = 2°$ and reduced frequency of $k = 5$. Blue lines represent the phase ordered data, red lines portray the phase averaged values with the black lines highlighting the standard deviation of the data in each phase bin.

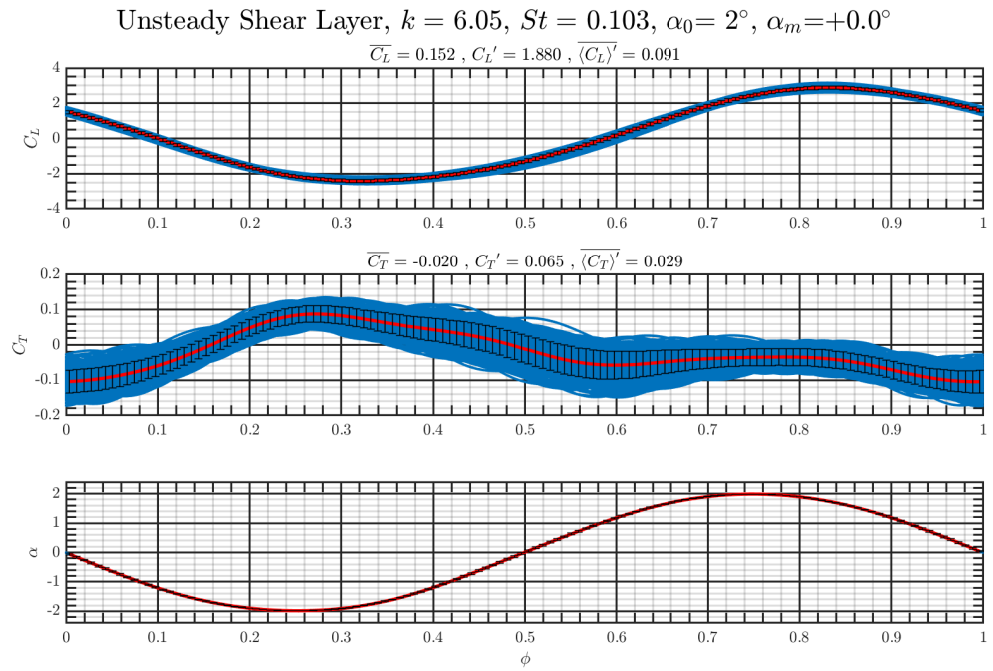

Figure D.18: Sample of phase ordered force measurements performed in unsteady shear flow for a pitching airfoil with oscillation amplitude of $\alpha_0 = 2°$ and reduced frequency of $k = 6$. Blue lines represent the phase ordered data, red lines portray the phase averaged values with the black lines highlighting the standard deviation of the data in each phase bin.

APPENDIX E

BOUNDARY LAYER MEASUREMENT ALTERNATE CONTOURS

The following figures provide alternative versions of the boundary layer resolved velocimetry results in a fashion that the airfoil shown at its actual angle of attack and the flow direction is from left to right, as shown with the arrow in plots. The color map used for generating the contour plots are designed to show a sharp change from dark blue to purple at a velocity of zero to further highlight the regions with reverse flow. The mean streamwise velocity values are normalized by the centerline velocity of the shear flow (U_c) while the shear layer velocity difference, Δu, is used to normalize the velocity fluctuations. The white patches in the contours are regions that are either partially blocked by the airfoil or have been affected by the glow from the airfoil surface.

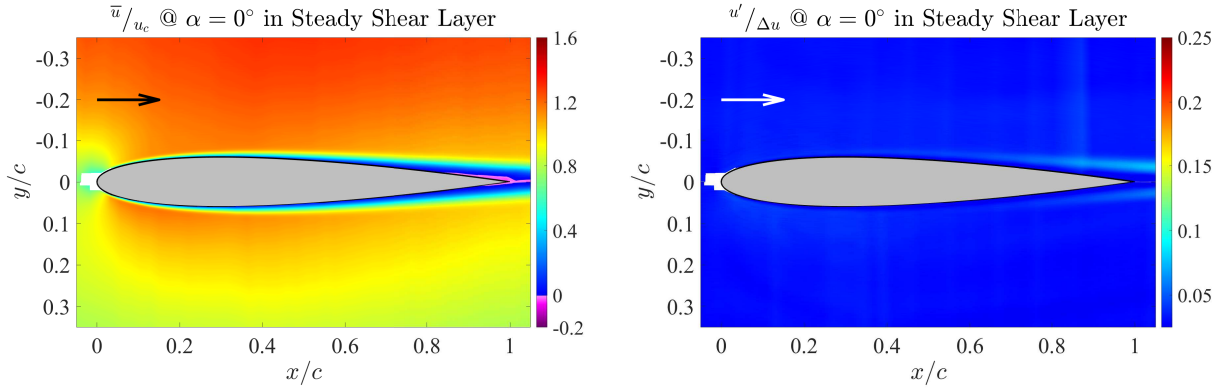

(a) (b)

Figure E.1: Contour of **(a)** mean and **(b)** fluctuating streamwise velocities measured near the surface of the airfoil positioned at $\alpha = 0°$ at the center of the steady shear layer.

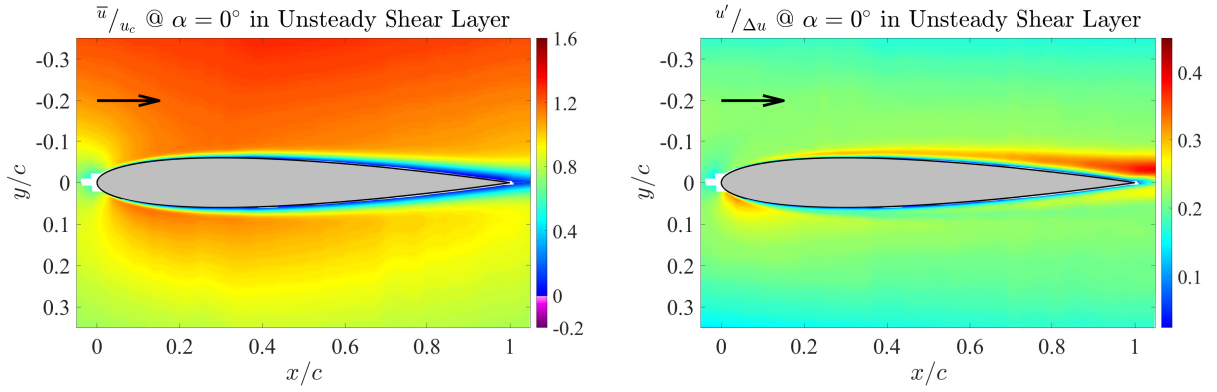

(a) (b)

Figure E.2: Contour of **(a)** mean and **(b)** fluctuating streamwise velocities measured near the surface of the airfoil positioned at $\alpha = 0°$ at the center of the unsteady shear layer.

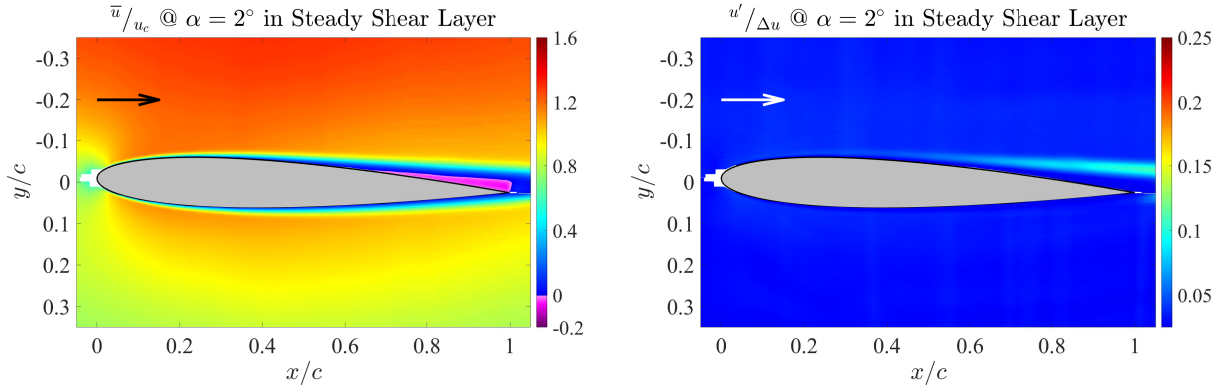

(a) (b)

Figure E.3: Contour of **(a)** mean and **(b)** fluctuating streamwise velocities measured near the surface of the airfoil positioned at $\alpha = 2°$ in the steady shear layer.

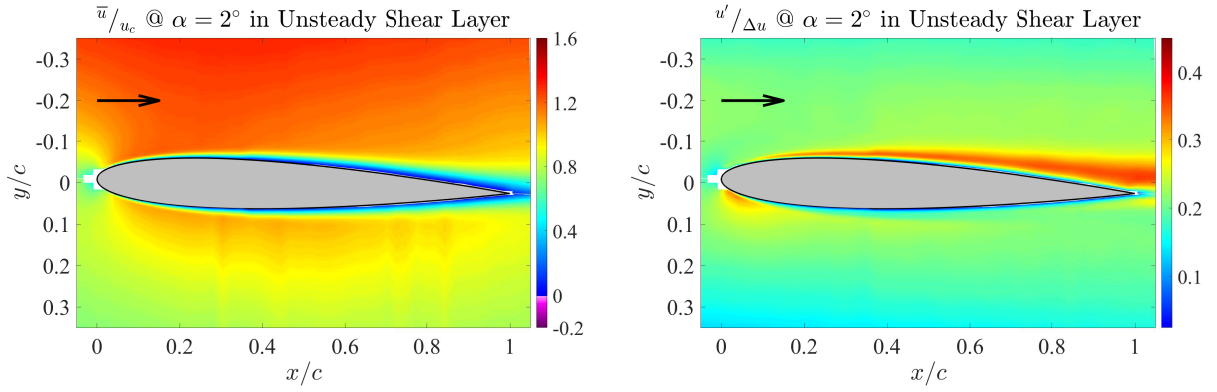

(a) (b)

Figure E.4: Contour of **(a)** mean and **(b)** fluctuating streamwise velocities measured near the surface of the airfoil positioned at $\alpha = 2°$ in the unsteady shear layer.

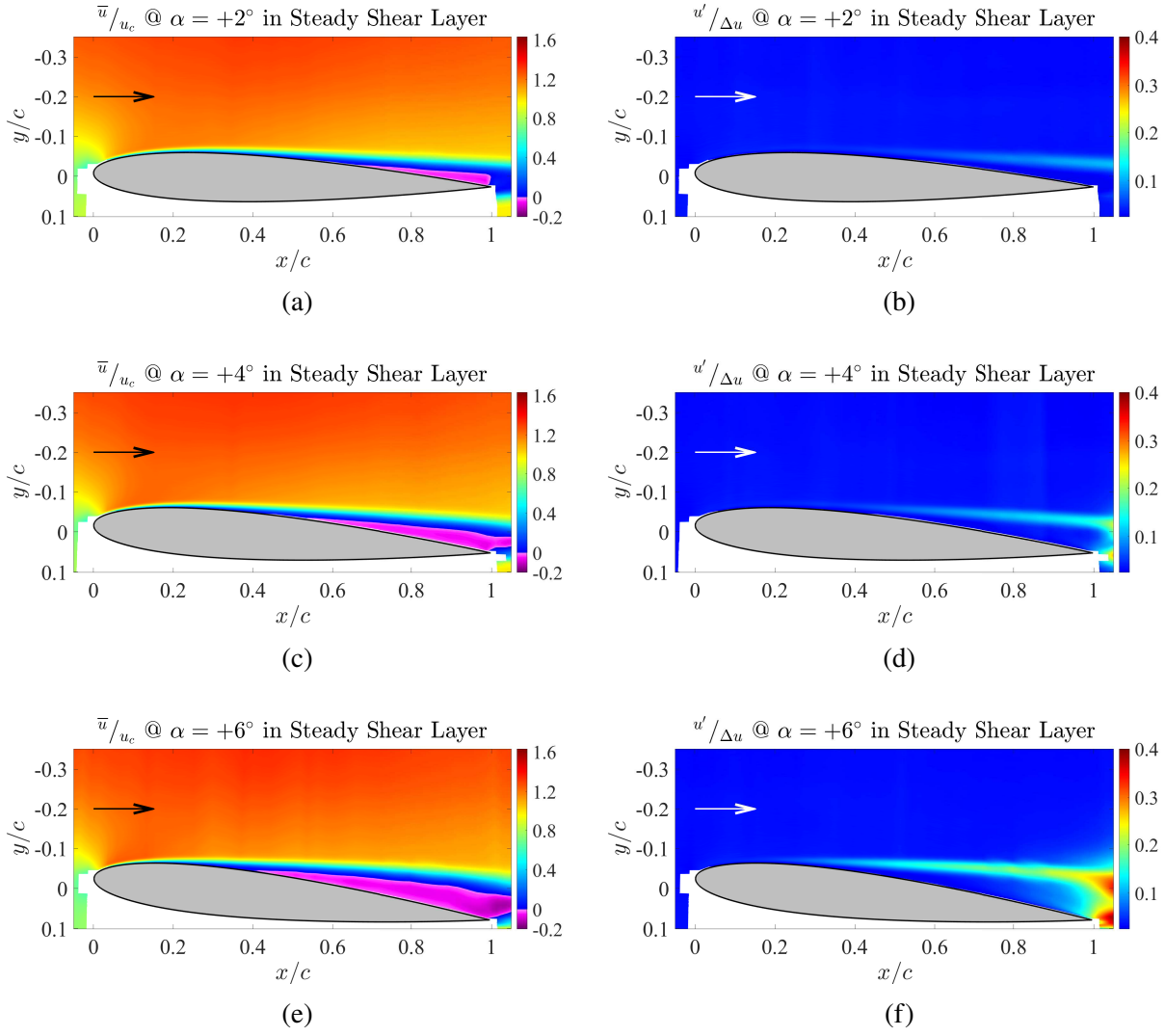

Figure E.5: Comparison of mean (left), and fluctuating (right) streamwise velocity contours measured near the suction surface of the airfoil positioned at positive angles of attack in the center of the steady shear layer.

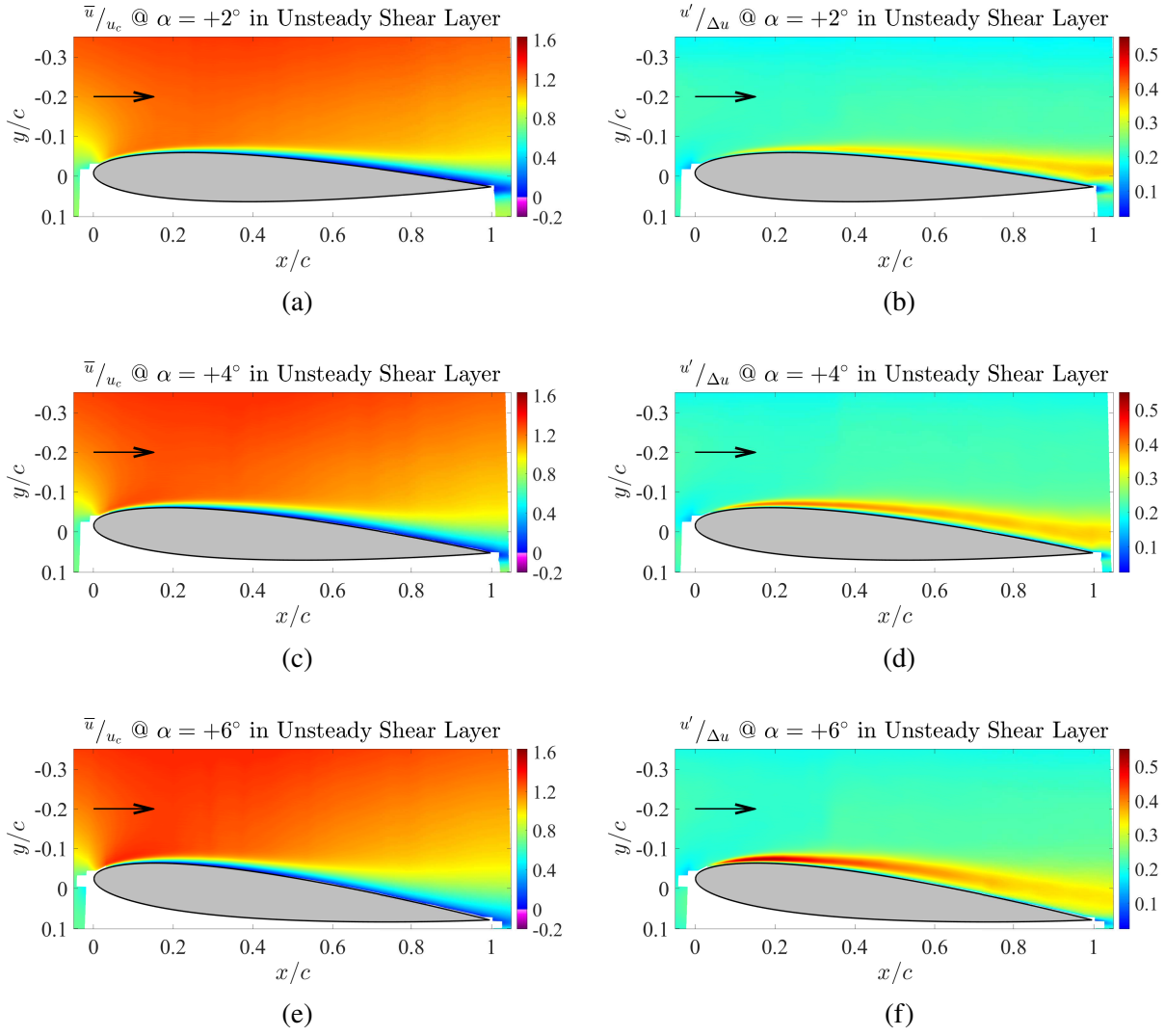

Figure E.6: Comparison of mean (left), and fluctuating (right) streamwise velocity contours measured near the suction surface of the airfoil positioned at positive angles of attack in the center of the unsteady shear layer.

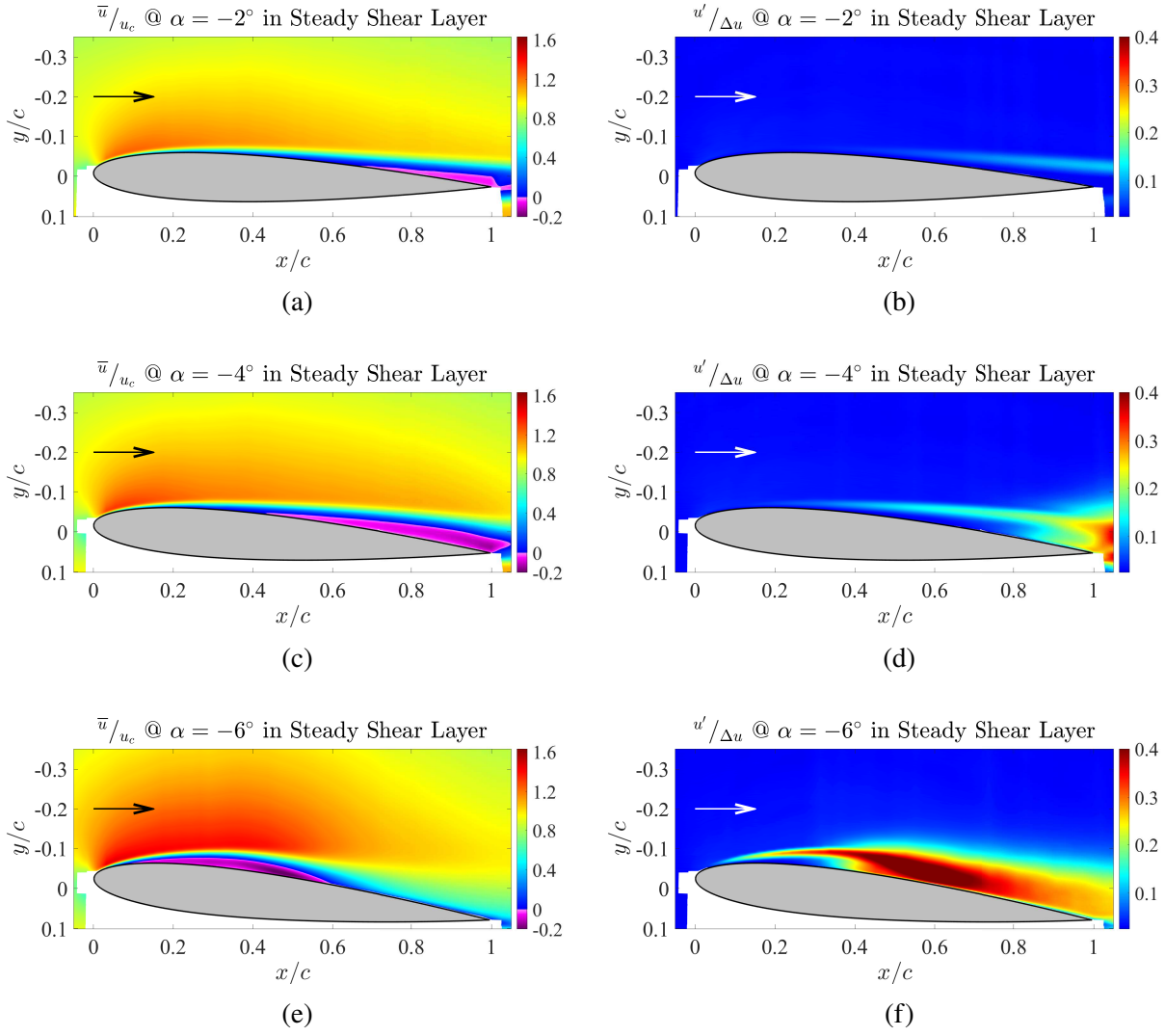

Figure E.7: Comparison of mean (left), and fluctuating (right) streamwise velocity contours measured near the suction surface of the airfoil positioned at negative angles of attack in the center of the steady shear layer.

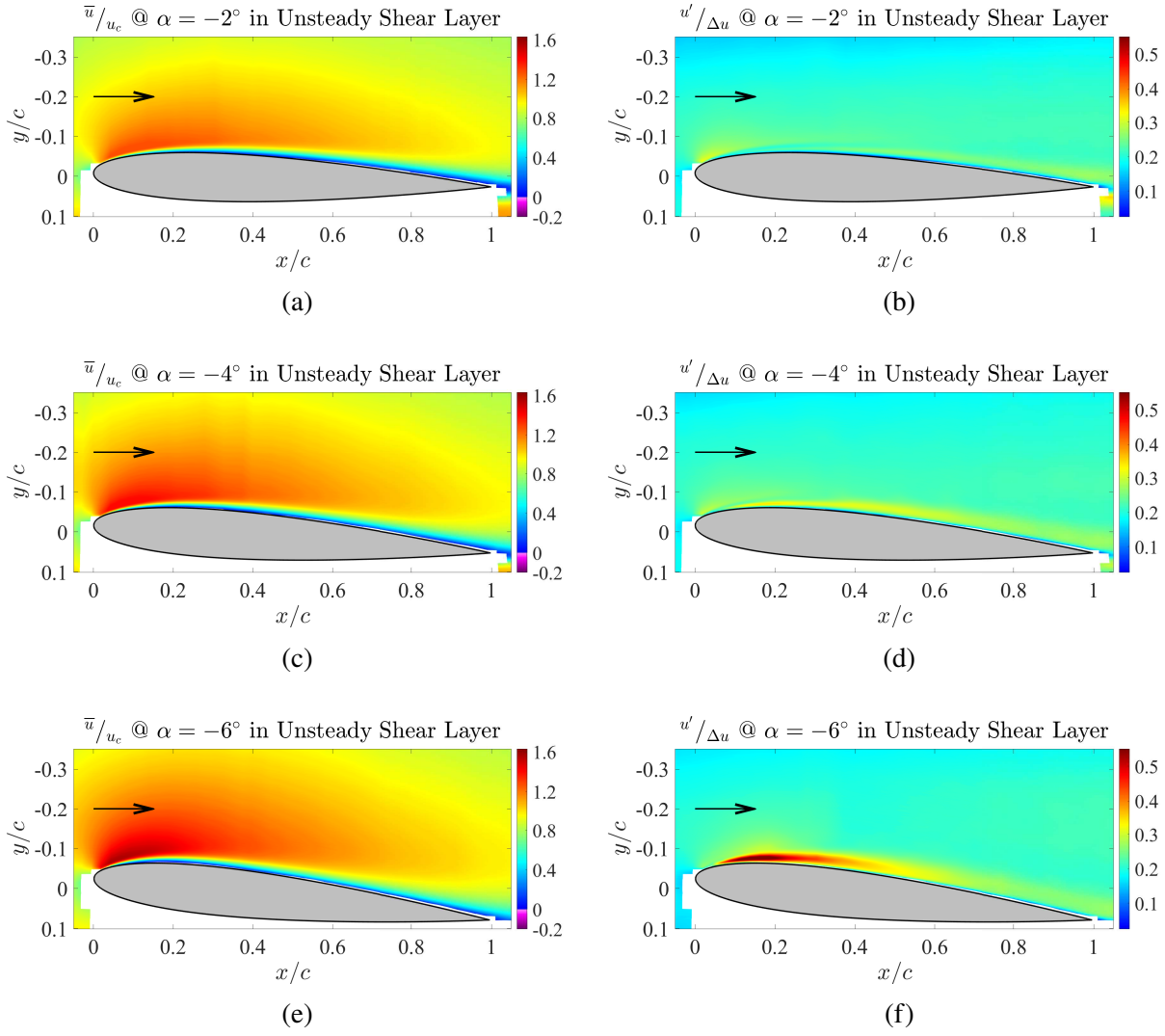

Figure E.8: Comparison of mean (left), and fluctuating (right) streamwise velocity contours measured near the suction surface of the airfoil positioned at negative angles of attack in the center of the unsteady shear layer.

BIBLIOGRAPHY

BIBLIOGRAPHY

Abramovich, G. N. 1963. *The theory of turbulent jets*. M.I.T. Press.

Bohl, D. G. 2002. *Experimental Study of the 2-D and 3-D Structure of a Concentrated Line Vortex Array*: Michigan State University dissertation.

Bohl, D. G. & M. M. Koochesfahani. 2009. MTV measurements of the vortical field in the wake of an airfoil oscillating at high reduced frequency. *Journal of Fluid Mechanics* 620. 63.

Brown, G. L. & A. Roshko. 1974. On density effects and large structure in turbulent mixing layers. *Journal of Fluid Mechanics* 64. 775–816.

Champagne, F. H., V. G. Harris & S. Corrsin. 1970. Experiments on nearly homogeneous turbulent shear flow. *Journal of Fluid Mechanics* 41. 81–139.

Cleaver, D., Z. Wang & I. Gursul. 2010. Vortex mode bifurcation and lift force of a plunging airfoil at low reynolds numbers. In *48th aiaa aerospace sciences meeting including the new horizons forum and aerospace exposition*, .

Cockrell, D. J. & B. E. Lee. 1966. Production of shear profiles in a wind tunnel by cylindrical rods placed normal to the stream. *Journal of the Royal Aeronautical Society* 70(667). 724–725.

Du Plessis, J. P & M. R Collins. 1992. A new definition for laminar flow entrance lengths of straight ducts. *N&O Joernaal* 25. 11–16.

Elder, J. W. 1959. Steady flow through non-uniform gauzes of arbitrary shape. *Journal of Fluid Mechanics* 5. 355–368.

Gendrich, C. P. & M. M. Koochesfahani. 1996. A spatial correlation technique for estimating velocity fields using molecular tagging velocimetry (MTV). *Experiments in Fluids* 22(1). 67–77.

Gendrich, C. P., M. M. Koochesfahani & D. G. Nocera. 1997. Molecular tagging velocimetry and other novel applications of a new phosphorescent supramolecule. *Experiments in Fluids* 23(5). 361–372.

Hammer, P. R. 2016. *Computational study of the effect of Reynolds number and motion trajectory asymmetry on the aerodynamics of a pitching airfoil at low Reynolds number*: Michigan State University dissertation.

Hammer, P. R., D. A. Olson, M. R. Visbal, A. M. Naguib & M. M. Koochesfahani. 2019. Joint Computational-Experimental Investigation of Harmonically Pitching Airfoil Aerodynamics in Uniform-Shear Approach Flow. *AIAA Journal* 57(8). 3290–3298.

Hammer, P. R, M. R Visbal, A. M Naguib & M. M Koochesfahani. 2016. Lift on a Steady Airfoil in Low Reynolds Number Shear Flow. In *Aps division of fluid dynamics meeting abstracts* APS Meeting Abstracts, E6.005.

Hammer, P. R., M. R. Visbal, A. M. Naguib & M. M. Koochesfahani. 2018. Lift on a steady 2-D symmetric airfoil in viscous uniform shear flow. *Journal of Fluid Mechanics* 837. R2.

Hill, R. B. & J. C. Klewicki. 1996. Data reduction methods for flow tagging velocity measurements. *Experiments in Fluids* 20(3). 142–152.

Ho, C. M. & P. Huerre. 1984. Perturbed free shear layers. *Annual Review of Fluid Mechanics* 16. 365–424.

Honda, M. & M. J Lighthill. 1960. Theory of a thin wing in a shear flow. *Proceedings of the Royal Society of London. Series A. Mathematical and Physical Sciences* 254(1278). 372–394.

James, D. G. 1951. Two-Dimensional Airfoils in Shear Flow. I. *The Quarterly Journal of Mechanics and Applied Mathematics* 4(4). 407–418.

von Karman, T. H. & J. M. Burgers. 1935. *Basic ideas of wing theory: Flow around an airfoil* 1–24. Berlin, Heidelberg: Springer Berlin Heidelberg.

von Karman, T. H. & W. R. Sears. 1938. Airfoil theory for non-uniform motion. *Journal of the Aeronautical Sciences* 5(10). 379–390.

Katz, A. W. 2010. *Molecular tagging velocimetry measurements of the low-reynolds-number flow around an sd7003 airfoil*. Michigan State University MA thesis.

Kiya, M., H. Tamura & M. Arie. 1980. Vortex-shedding from a circular cylinder in moderate-Reynolds-number shear flow. *Journal of Fluid Mechanics* 101. 721–735.

Koochesfahani, M. M. 1989. Vortical patterns in the wake of an oscillating airfoil. *AIAA Journal* 27(8). 1200–1205.

Koochesfahani, M. M & D. G Bohl. 2002. Molecular tagging visualization and velocimetry of the flow at the trailing edge of an oscillating airfoil. In *Proceedings of the 10th international symposium on flow visualization*, .

Koochesfahani, M. M & P. E. Dimotakis. 1989. Effects of a downstream disturbance on the structure of a turbulent plane mixing layer. *AIAA Journal* 27(2). 161–166.

Koochesfahani, M. M & D. G. Nocera. 2007. *Molecular tagging velocimetry (mtv)* 362–382. Berlin, Heidelberg: Springer Berlin Heidelberg.

Kotansky, D. R. 1966. The use of honeycomb for shear flow generation. *AIAA Journal* 4. 1490–1491.

Lau, Y. L. & W. D. Baines. 1968. Flow of stratified fluid through curved screens. *Journal of Fluid Mechanics* 33. 721–738.

Lee, K. S, C. H Chung & J. H Baek. 2014. Lift correction model for local shear flow effect on wind turbine airfoils. *Renewable Energy* 65. 275 – 280.

Liepmann, H. W & J Laufer. 1947. Investigations of free turbulent mixing. Tech. rep. National Advisory Committee for Aeronautics.

Lighthill, M. J. 1969. Hydromechanics of Aquatic Animal Propulsion. *Annual Review of Fluid Mechanics* 1. 413–446.

Lissaman, P. B. S. 1983. Low-reynolds-number airfoils. *Annual Review of Fluid Mechanics* 15(1). 223–239.

Livesey, J. L. & E. M. Laws. 1973. Flow through non-uniform gauze screens. *Journal of Fluid Mechanics* 59(4). 737–743. doi:10.1017/S0022112073001825.

Muzychka, Y. S. & M. M. Yovanovich. 2009. Pressure Drop in Laminar Developing Flow in Noncircular Ducts: A Scaling and Modeling Approach. *Journal of Fluids Engineering* 131(11).

Naguib, A. M. & M. M. Koochesfahani. 2012. Canonical airfoil gust interactions for micro-air vehicles. Final technical report Universal Technology Corporation.

Nishiyama, T. & K. Hirano. 1970. Aerofoil section characteristics in shear flows. *Ingenieur-Archiv* 39(3). 137–148.

Olson, D. A. 2011. *Facility and flow dependence issues influencing the experimental characterization of a laminar separation bubble at low reynolds number*. Michigan State University MA thesis.

Olson, D. A. 2017. *The Influence of Chordwise Flexibility on the Flow Structure and Streamwise Force of a Sinusoidally Pitching Airfoil*: Michigan State University dissertation.

Olson, D. A., A. W. Katz, A. M. Naguib, M. M. Koochesfahani, D. P. Rizzetta & M. R. Visbal. 2013. On the challenges in experimental characterization of flow separation over airfoils at low reynolds number. *Experiments in Fluids* 54(2). 1470.

Olson, D. A., A. M. Naguib & M. M. Koochesfahani. 2015. Measurement of the wall pressure and shear stress distribution using molecular tagging diagnostics. *Experiments in Fluids* 56(8). 171.

Olson, D. A, A. M Naguib & M. M Koochesfahani. 2016. Experiments on a Steady Low Reynolds Number Airfoil in a Shear Flow. In *Aps division of fluid dynamics meeting abstracts*, E6.006.

Owen, P. R. & H. K. Zienkiewicz. 1957. The production of uniform shear flow in a wind tunnel. *Journal of Fluid Mechanics* 2. 521–531.

Payne, F. M. & R. C. Nelson. 1985. Aerodynamic characteristics of an airfoil in a nonuniform wind profile. *Journal of Aircraft* 22(1). 5–10.

Rose, W. G. 1970. Interaction of grid turbulence with a uniform mean shear. *Journal of Fluid Mechanics* 44(4). 767–779.

Sabin, C. M. 1965. An Analytical and Experimental Study of the Plane, Incompressible, Turbulent Free-Shear Layer With Arbitrary Velocity Ratio and Pressure Gradient. *Journal of Basic Engineering* 87(2). 421–428.

Shah, R. K. 1978. A Correlation for Laminar Hydrodynamic Entry Length Solutions for Circular and Noncircular Ducts. *Journal of Fluids Engineering* 100(2). 177–179.

Theodorsen, T. 1949. General theory of aerodynamic instability and the mechanism of flutter. Tech. rep. National Advisory Committee for Aeronautics.

Tsien, H. S. 1943. Symmetrical joukowsky airfoils in shear flow. *Quarterly of Applied Mathematics* 1(2). 130–148.

Turner, J. T. 1969. A computational method for the flow through non-uniform gauzes: the general two-dimensional case. *Journal of Fluid Mechanics* 36. 367–383.

Wang, S., Y. Zhou, M. d. Mahbub Alam & H. Yang. 2014. Turbulent intensity and reynolds number effects on an airfoil at low reynolds numbers. *Physics of Fluids* 26(11). 115107.

Wygnanski, I. & H. E. Fiedler. 1970. The two-dimensional mixing region. *Journal of Fluid Mechanics* 41(2). 327–361.